

國立交通大學

材料科學與工程學系

博 士 論 文

奈米介孔材料之合成、結構及其氣體感測性質

之研究



Fabrication, Structure and Gas Sensing Applications of
Mesostructured Materials

研 究 生：劉厥揚

指導教授：陳家富 教授

呂志鵬 教授

中 華 民 國 九 十 八 年 三 月

奈米介孔材料之合成、結構、及其氣體感測性質之研究

研究生：劉厥揚

指導教授：陳家富 博士

呂志鵬 博士

國立交通大學

材料科學與工程研究所

摘 要

近年來，隨著工業的進展及環保意識的重視，各種廢氣量日益增加，對於有毒氣體如CO, CO₂, SO₂, NO₂等外在環境的控制亦趨重要。它們對人體有害，同時也對環境造成嚴重的傷害。因此，偵測污染源並提出預警變的更顯重要。為了改善傳統氣體感測器之昂貴、笨重與偵測耗時等缺點，近年來已有許多研發專注於新型氣體感測器之上。

本研究利用模版複印法製備三種新型態的奈米孔洞氣體感測器。在多孔的二氧化矽模板上分別製備p型半導體的多孔碳及多孔氧化鈷感測材料；另外，利用多孔碳為模板製備n型半導體的多孔氧化鋅感測材料。初製備的此三種奈米孔洞材料均具有均勻尺寸與多孔性，利用X光繞射(XRD)光譜對不同的樣品做相鑑定；利用掃描式(SEM)及穿透式電子顯微鏡 (TEM)量測材料的結晶結構和顯微結構；利用氮氣吸脫附分析儀(BET)分析材料的表面積及孔洞的尺寸。並研究奈米孔洞材料的結構、表面形態對於一氧化碳感測特性的影響。由實驗結果得之，此三種孔洞感測材料在相當低濃度(10-100 ppm)的一氧化碳環境下均具有良好的感應能力，其中具有單晶結構的多孔氧化鋅感測材料具有51.7%的敏感度，並提出此新穎氣體感測器之可能的感測機制。

另外，為了減少能量的消耗，本研究也結合微機電技術設計並製作新型微型薄膜氣體感測器。感測器以矽為基材，並包括了加熱器、絕緣層、電極、感測層等結構，而感測材料則是在室溫下利用電泳方式排列沉積。在電泳過程中感測材料因為受到電場極化作用下聚集並沿著電場方向排列，最後成功的吸附在電極上。由實驗結果得之，多孔材料的規則排列的結構提供更多的活性反應面積使得多孔氧化鋅感測材料在70 ppm CO下

有60.0%的敏感度且反應時間約為90秒。此種新穎的氣體感測器具有高靈敏度、快速的反應時間及良好的可逆性等特性，為一新穎且簡易之氣體感測器。

。



Fabrication, Structural and Gas Sensing Applications of Mesostructured Materials

Student : Chueh-Yang Liu

Advisor : Dr. Chia-Fu Chen

Dr. Jih-Perng Leu

Institute of Materials Science and Engineering
National Chiao-Tung University

Abstract

Recently, environmental protection has gained attention as a result of industrial development and an increase in the emission of various kinds of exhaust gases. Noxious gases such as CO, CO₂, SO₂, and NO₂ are presented in the atmosphere. They are highly toxic for the human body and also cause indirect harm to the environment. Traditional gas sensors that have been used thus far are expensive, heavy, and prone to delay; in order to overcome these problems, many studies have focused on developing gas sensors.

In this study, three novel nanoporous gas sensors were synthesized by using the template replication method. P-type semiconducting sensors for example mesostructured carbon and mesostructured cobalt oxide were synthesized using a porous SiO₂ template. Further, an n-type semiconducting porous ZnO sensor was synthesized using porous carbon as a template. The prepared mesostructured materials were highly ordered porous structure with uniform particle sizes. Powder x-ray diffraction (XRD) spectra of the different mesostructured materials confirm the phase of these materials. The crystal structure and microstructure of the mesostructured materials were observed by scanning electron microscopy (SEM) and transmission electron microscopy (TEM). The surface areas and pore-size distributions of the

mesostructured materials were analyzed by N₂ adsorption-desorption isotherms. Structural and morphological studies were carried out in order to investigate the influence of these materials on the sensing properties of sensors synthesized using mesostructured materials. All of the sensing materials have good sensitivity for low CO concentrations (10–100 ppm). Among the porous sensing materials, porous ZnO had a sensitivity of 51.7%. The sensing-mechanism of these novel gas sensors was reviewed.

In order to reduce the power consumption in sensors, in this study, we have designed and developed a system for measuring energy consumption on the microscopic scale. Sensors were fabricated on silicon substrates using micro electromechanical systems (MEMS) technologies and compatible with integrated circuit (IC) process. The layers in the device include a micro-heater, an isolator, electrodes, and a sensing film. The sensing materials were aligned and immobilized between electrodes by using the dielectrophoresis process, which is known to be a convenient method for the manipulation of dielectric substances in a liquid. Experimental results showed that the regular aligned structure of these mesostructured materials provide number of active areas on the sensor; porous ZnO had a sensitivity of 60.0% and had a fast response time of 90 s. These mesostructured gas sensors have been developed in this study with high sensitivity, good response properties and good repeatability. Moreover, the preparation process of the mesostructured sensor was a simple method.

誌謝

四年半，一個說長不長說短也不短的時間，我完成了我的博士生涯。寫此篇誌謝的當下中，心中百感交集，有喜悅也有不捨。當順利完成此本論文的同時，心中滿懷喜悅與感激，喜悅的是順利完成博士論文；不捨的則是要離開美麗的交大校園跟一起打拼的夥伴們。首先要感謝我的指導教授-陳家富老師-在專業知識及相關領域上的細心指導與解惑及其他方面的訓練與指導，使學生獲益不少。此外，也很感謝我的另一位指導教授-呂志鵬老師-在實驗方面給予許多的建議。另外，感謝暨南大學 孫台平院長、交通大學材料系 陳三元教授、明新科大化工系 陳密教授於口試期間的建議與指導，使學生的論文更加充實，在此致上最誠摯的謝意。

研究期間，感謝實驗室的成員-士塵學長、鴻鈞學長、光中學長、建仲學長、建銘學長、振航學長、騰凱同學及琮琦、瑞豪、方慈、宜輝、家駿等學弟及明道大學政宜、昱顯、朝俊等學弟的鼎力幫忙，使我在博士班的生涯中更多采多姿。另外，感謝目前在高應大任教的弘穎學長在實驗方面的經驗傳授與指教，使我實驗能更順利完成。還有德銘學長、詠煌、建民、世緯、伸鉉、又維、小麥、賀昌、牧龍、昱涵、均元、少農、宏偉、文碩、崇榮、冠名、志遠等學弟及志欣、維齡、小蔡等學妹在實驗上的幫忙與鼓勵。特別感謝交大材料的克遙、蕙馨跟麗娟姐在行政上的大力幫忙。由於要感謝的人太多，不及一一備載，望請海涵。

最後，僅以此篇論文至給我最愛的家人及所有關心我的人，感謝你們在背後無怨無悔的支持與鼓勵，謝謝。

Contents

中文摘要	i
Abstract	iv
Acknowledge	vi
Contents	vii
Table Caption.....	ix
Figure Caption	x
Chapter 1 Introduction.....	1
1.1 Background.....	1
1.2 Motivation	3
Chapter 2 Mesoporous Materials: Literature Review.....	5
Chapter 3 Functionals of Semiconductor Metal Oxide Gas Sensor	13
3.1 Physisorption and Chemisorption.....	14
3.2 Charge Tranfer Model (CTM)	15
3.3 Depletion Layers Effect.....	17
3.4 Necked-controlled and Grain Boundary Effect	18
3.5 Scottky Contact	21
3.6 Oxygen Vacancy	23
Chapter 4 Experimental Methods	25
4.1 Synthesis of Mesoporou Materials	25
4.1.1 Synthesis of mesoporous silica template.....	25
4.1.2 Synthesis of mesoporous carbon	25
4.1.3 Synthesis of mesoporous metal oxide materials.....	26
4.2 Fabrication of mesostructured sensing device.....	27
4.2.1 Fabrication of thick-film sensor device	27

4.2.2 Fabrication of thin-film sensors.....	27
4.3 Characterization.....	31
4.3.1 XRD.....	31
4.3.2 FE-SEM.....	31
4.3.3 TEM.....	31
4.3.4 DTA/TGA.....	31
4.3.5 XPS.....	31
4.4 Gas-sensing measurement	32
Chapter 5 Result and discussion.....	34
5.1 Mesoporous silica template	34
5.1.1 Synthesis of SBA-15 at different temperatures	34
5.1.2 Synthesis of SBA-15 at low acid concentrations	49
5.1.3 Two step desorption isotherm of SBA-15	54
5.2 Mesostructured cobalt oxide materials.....	55
5.3 Mesostructured carbon materials.....	79
5.4 Synthesis of mesostructured ZnO materials	97
5.5 Mesosttrured-based micro sensors	104
5.5.1 Overview of the micro-sensor	105
5.5.2 Gas-sensing for DEP-trapped mesostructured materials	107
5.6 Tunable interconnectivity of mesostructured materials on sensing performance	121
5.7 The new mechanism of mesostructured-based sensors	124
Chapter 6 Conclusions.....	127
Reference.....	131

Table Captions

Table 1.1 Typical deposition techniques used for preparation of gas-sensitive materials based on semiconductors.....	2
Table 2.1 Pore-size definition of the porous materials	5
Table 5.1 Device specification for mesostructured materials.....	116



Figure Captions

Figure 1.1 The sensor material is deposited on the interdigitated electrode	4
Figure 2.1 Two possible pathways for the LCT mechanism.....	6
Figure 2.2 Assembly of silicate rods	7
Figure 2.3 Puckering of silicate layers in the direction	7
Figure 2.4 Curvature induced by charge density matcgng. The arrow indicates the reaction coordinate.....	8
Figure 2.5 Folding of silicate sheets around intercalated surfactant moloecules. (a) Ion exchange, (b) calciate.....	8
Figure 2.6 Formation of a silicatropic liquid crystal phase.....	9
Figure 2.7 The illustrations of M41S materials: (a) MCM-41, (b) MCM-48, and (c) MCM-50 ..	10
Figure 2.8 The schematic diagram of SBA-15 synthesizes with triblock copolymer.....	11
Figure 3.1 The thermal desorption spectra (TDS) of molecular oxygen on ZnO. Curve C is the first heat treatment	15
Figure 3.2 The space charge at the surface of an n-type semiconductor (left) and of a p-type semiconductor (right) due to the adsorption of an electron acceptor. (a) Distribution of the charge carrier. (b) Band deflection at the semiconductor surface. (c) Charge carrier concentration in the conductor resp. valence band. E_C : edge of the conduction band, E_V : edge of the valence band, E_F : Fermi level, E_D : donor level, E_A : acceptor level, E_I : intrinsic level, n_b : concentration of electrons in the bulk, p_b : concentration of holes in the bulk.....	16
Figure 3.3 Charge carrier concentration n and conduction band E_C for a contact position of grain boundaries for a grain with a Debye-length (LD) less than half grain size on the left side and a grain with a Debye-length more than half grain size on the right	

side.	18
Figure 3.4 Surface space charge layer and electron transport between grain and target gases. (a) Grain boundaries, (b) Necked. E: Potential energy of electrons.	19
Figure 3.5 Assumed electron density profiles at the cross section of a neck.	20
Figure 3.6 Schematic diagram of grain size effect of nanoparticles.	20
Figure 3.7 (a) Energy-band diagram of metal-oxide-n-type semiconductor junction: (1) Before contact, (2) After contact and thermodynamic equilibrium is attained, in the presence of a gap (or an insulating dielectric) of thickness d , (3) When d is comparable to interatomic distance, and (4) in the limit $d=0$ (metal-semiconductor junction)	22
Figure 4.1 Schematic of the alumina substrates with the interdigitated electrodes.....	27
Figure 4.2 The fabrication schematic diagram of the micro sensor device.....	28
Figure 4.3 Schematic diagram of the DEP system.....	29
Figure 4.4 The OM images (a) before the DEP immobilized; (b) after the DEP immobilized of the mesostructured metal oxide samples.....	30
Figure 4.5 The diagram of the mesostructured materials testing chamber.....	32
Figure 5.1 XRD patterns of as-synthesized SBA-15 template.....	35
Figure 5.2 The SEM image of as-synthesized SBA-15 template.....	35
Figure 5.3 (a) The nitrogen isotherms of as-synthesized SBA-15 and (b) the corresponding pore size distribution.....	36
Figure 5.4 The XRD patterns of SBA-15 synthesized at 40, 60 and 100°C..	38
Figure 5.5 (a) Nitrogen adsorption-desorption isotherms and (b) pore size distribution of SBA-15 synthesized at 40, 60, and 100°C.....	39
Figure 5.6 The SEM images of SBA-15 synthesized at different temperature. (a) 40°C, (b) 60°C, and (c) 100°C.....	40
Figure 5.7 The TEM micrographs of SBA-15 synthesized at different aging temperatures (a)	

40°C, (b) 60°C, and (c) 100°C.....	44
Figure 5.8 Schematic representation of micelle dehydration upon temperature.....	45
Figure 5.9 Phase diagram of P123, EO ₂₀ PO ₇₀ EO ₂₀	45
Figure 5.10 Schematic representation of SBA-15 synthesized (a) between 40 and 60 °C showing micropores and no connection between mesopores, (b) around 100°C showing micropores and connection between mesopores.. ..	48
Figure 5.11 The XRD patterns for the mesostructured silica synthesized under 0.001 M acid concentrations.. ..	50
Figure 5.12 The SEM image of mesostructured SBA-15 synthesized under 0.001 M acid concentration.....	50
Figure 5.13 Nitrogen adsorption-desorption isotherm of “plugged” mesopores, comprising both open and blocked mesopores, intrawall micropores, and microporous silica nanocapsules	53
Figure 5.14 Thermal decompositions plot of the cobalt-silica composite.....	56
Figure 5.15 (a) XRD patterns of samples with cobalt oxide in SBA-15 at different aging temperatures, and (b) XRD patterns of cobalt oxide heated at 250°C with varying times.....	57
Figure 5.16 XRD patterns of the specimens after decomposing Co(NO ₃) ₂ • 6H ₂ O without the presence of silica template.....	59
Figure 5.17 SEM images of mesostructured Co ₃ O ₄ materials heated at 250°C with varying times: (a) 10 min, (b) 30 min, (c) 60 min, (d) 180 min, and (e) 360 min, respectively. Typical bright-field TEM image of the mesostructured Co ₃ O ₄ materials in (f), inset is the corresponding selected areas electron diffraction; (g) shows a corresponding HRTEM image of (f).. ..	63
Figure 5.18 XPS measurement for (a) Co _{2p} , and (b) O _{1s} core levels for mesostructured cobalt oxide materials.. ..	64

Figure 5.19 (a) Nitrogen adsorption-desorption isotherms measured at 77 K and (b) corresponding pore size distributions of the mesostructured cobalt oxide materials...	66
Figure 5.20 The XRD patterns at (a) low-angle, (b) wide-angle regions of the mesostructured cobalt oxide materials with the templates prepared from different temperatures: (I) 40°C, (II) 60°C, and (c) 100°C..	69
Figure 5.21 Effect of size variation in 2D hexagonal parent silica on the preparation cobalt oxide. TEM images of preparation cobalt oxide at different crystallization temperatures: (a) 40°C, (b) 60°C, and (c) 100°C.....	71
Figure 5.22 Nitrogen adsorption-desorption isotherms of cobalt oxide prepared from SBA-15 templates with different crystallization temperatures: (I) 40°C, (II) 60°C, and (III) 100°C	71
Figure 5.23 Schematic diagram of preparing metal oxide arrays.....	73
Figure 5.24 Sensor response and recovery times of mesostructured materials with the applied voltages modulated from 1 V to 10 V.....	74
Figure 5.25 Sensor response of mesostructured cobalt oxide materials to 20 ppm CO at different working temperatures.....	76
Figure 5.26 The SEM images of mesostructured cobalt oxide sensing materials printed on the alumina substrate.....	76
Figure 5.27 Dynamic response of mesostructured cobalt oxide materials to different concentrations of CO in synthetic air at 200°C.....	77
Figure 5.28 Sensor response of mesostructured cobalt oxide materials to different concentrations of CO in synthetic air.....	77
Figure 5.29 The low-angle XRD patterns of mesostructured carbon synthesized from SBA-15 silicas at different carbonization temperatures: (i) 600°C, (ii) 700°C, (iii) 900°C, and (iv) 1000°C.....	80

Figure 5.30 Representative SEM image for mesostructured carbon at different carbonization temperatures: (a) 600°C, (b) 700°C, (c) 900°C, and (d) 1000°C.....	82
Figure 5.31 TEM images of the mesostructured carbon after carbonization treatment at 900°C..	84
Figure 5.32 The nitrogen adsorption-desorption isotherms of mesostructured carbon at different carbonization temperatures: (i) 600°C, (ii) 700°C, (iii) 900°C, and (iv) 1000°C..	84
Figure 5.33 XPS spectra of mesostructured carbon carbonized at different temperatures: (a) 600°C, (b) 700°C, (c) 900°C, and (d) 1000°C.....	85
Figure 5.34 (a) Nitrogen adsorption-desorption isotherm and (b) pore size distribution curves of mesostructured carbon from various SBA-15 templates: (i) 40°C, (ii) 60°C, and (c) 100°C.....	89
Figure 5.35 The low-angle XRD patterns of the mesostructured carbon synthesized from various silica templates: (i) 40°C, (ii) 60°C, and (iii) 100°C.....	90
Figure 5.36 Representative SEM images of the mesostructured carbon materials synthesized at various SBA-15 templates: (i) 40°C, (ii) 60°C, and (iii) 100°C..	90
Figure 5.37 Representative TEM images of the mesostructured carbon materials synthesized at various SBA-15 templates: (i) 40°C, (ii) 60°C, and (iii) 100°C..	92
Figure 5.38 The SEM images of mesostructured carbon sensing materials printed on the alumina substrate.....	95
Figure 5.39 Sensor responses of mesostructured cobalt oxide materials to different concentrations of CO in synthetic air.....	95
Figure 5.40 An energy band diagram of the Schottky barrier formed at interface between metal and p-type mesostructured carbon. E_F : Fermi level; E_C : conduction band; E_V ..	96
Figure 5.41 Concentrations dependence of the mesostructured carbon gas sensor response....	96

Figure 5.42 (a) low angle XRD patterns and (b) wide angle XRD patterns of the mesostructured ZnO.....	98
Figure 5.43 SEM image of the mesostructured ZnO.....	99
Figure 5.44 (a) TEM image of mesostructured ZnO materials, as a replica of mesostructured carbon template. (b) HRTEM micrograph of the crystalline framework of mesostructured ZnO.....	99
Figure 5.45 XPS spectra of (a) Zn 2p spectra, and (b) O 1s spectra of the mesostructured ZnO..	101
Figure 5.46 Variation of sensing response of mesostructured ZnO sensor with temperature at 20 ppm CO.....	104
Figure 5.47 Sensing response of mesostructured ZnO sensor determined with several CO concentrations.	104
Figure 5.48 Schematic design of a micro sensor device with the micro-hotplate membrane..	106
Figure 5.49 The top-view diagram of the micro sensor electrode.....	106
Figure 5.50 (a) low-magnification SEM images and (b) high-magnification SEM images of DEP-trapped mesostructured cobalt oxide.....	108
Figure 5.51 Dynamic sensor response of DEP-trapped mesostructured cobalt oxide sensor measured with various CO concentrations.....	110
Figure 5.52 Switching response of the DEP-trapped mesostructured cobalt oxide exposed to 50 ppm CO.	110
Figure 5.53 Linear sensor response of the DEP-trapped mesostructured cobalt oxide at various CO concentrations.....	111
Figure 5.54 (a) low-magnification SEM images and (b) high-magnification SEM images of DEP-trapped mesostructured ZnO..	113
Figure 5.55 (a) Switching response of the mesostructured ZnO sensor exposed to 30	

ppm CO gas, and (b) sensing response of mesostructured ZnO sensor determined with several CO concentrations..	115
Figure 5.56 The SEM images of (a) low magnification and (b) high magnification of the DEP-trapped mesostructured carbon..	119
Figure 5.57 (a) Response of the mesostructured carbon sensor measured with various CO concentrations and (b) Switch response of the mesostructured carbon sensor exposed to 30 ppm CO gas..	120
Figure 5.58 The sensor resistance of mesostructured cobalt oxide materials at different crystallization temperatures: (I) 40°C, and (II) 100°C.....	122
Figure 5.59 Relationship between the sensitivity of mesostructured cobalt oxide sensor at different crystallization temperatures: (I) 40°C, and (II) 100°C.....	122
Figure 5.60 The diagram showing the gas accessibility for mesostructured materials.....	126



Chapter 1 Introduction

1.1 Background

The increase in air pollution-as evidenced by acid rain, increase in particulate matter, the disappearance of the ozone shield, and the appearance of greenhouse effect-has thus far been the result of development in industry and technology. Such developments are an inconvenience and detriment to all human life. The gases involved include CO, CO₂, NO_x, SO_x, hydrocarbons, and hydrogen; these pollution gases have been cited as the main causes of “global warming” and “greenhouse effects” [1]. In light of these developments, various techniques have been widely used in the accurate analysis and detection of these gases. The installation of these conventional instruments is costly, and they require not only a sampling system and regular maintenance but also the continuous monitoring of most gases. To fulfill these demands, a device has been developed with an eye to safety, economy, pollution control, and the logistics of industrial processes. The majority of these devices involve the application of surface or bulk chemicals to determine the physical properties of materials; for this reason, many of them are called chemical sensors [2-5]. In general, there are three kinds of gas sensor categories: (1) solid electrolyte gas sensors, (2) catalytic combustion gas sensors, and (3) semiconductor gas sensors. They possess certain characteristics-such as low cost, quick sensor response, prompt recovery times, good mechanical strength, and long lifetime-that make them as attractive as semiconductor gas sensors to commercial sensor users [6].

In the last decade, several researchers and industries have developed optimal gas sensors, with the goal of determining a parameter to which optimized sensors can be manufactured and set to monitor, *vis-à-vis* different substances in different environmental conditions [7]. The synthesis and deposition of the sensing layer is obviously the most crucial part of preparing of gas sensors, and there are three main groups thereof: powder/slurry deposition, chemical

vapor deposition (CVD) and physical vapor deposition (PVD). The preparation methods for sensing films are listed in Table 1 [7, 8].

Table 1.1 Typical deposition techniques used for preparation of gas-sensitive materials based on semiconductors.

Powder/slurry	CVD	PVD	
		Sputtering	Evaporation
Sol-gel	Thermal CVD	Reactive	MBE
Precipitation	Plasma CVD	Cathode	Thermal
Print-Screen	Laser Induced		Reactive
Dip coating	Electroless		Laser
Spin coating			Arc

The traditional sensing material is usually deposited as a polycrystalline film or layer on a substrate with integrated electrodes and a heater (Figure 1.1) [9]. Extensive scientific research has focused on the optimization of semiconducting sensors with respect to their sensitivity, response rate, gas selectivity, and economic efficiency [10–15]. It is apparent that the physics and chemistry of semiconducting sensing equipment is complex and not yet understood. Although several principles *vis-à-vis* semiconducting sensing equipment have been identified, it has often been difficult to improve sensing performance. The most important properties of semiconducting sensing materials equipment are their sensitivity, operating temperature, selectivity, and long-term stability. On the other hand, the optimal sensing equipment should provide strong and noise-free changes in conductance upon changes in target gas concentration, as well as shorter response times and a reliable lifecycle. Finally, their energy consumption should be minimal.

1.2 Motivation

Apart from being applicable in a more universal fashion, the structure replication method bears another important advantage over the use of amphiphiles as structure directors, as well as over regular sol-gel synthesis lacking structure directors. In general, rigid matrices can withstand high temperatures during the formation of the desired metal oxides inside their pore systems. Serving as a rigid skeleton, a solid-state template allows for temperatures of several hundred degrees, without a loss of periodic structure. Thus, higher degrees of crystallinity and larger single-crystalline domains are possible. The concept of using structure directors or rigid structure matrices for the synthesis of mesoporous metal oxide gas sensors offers a number of substantial advantages over conventional synthesis methods. Mesoporosity plays a vital role in the application of semiconducting metal oxides as gas sensors. Apart from exhibiting high sensitivities due to their large specific surface areas, sensors with well-defined porosity offer powerful opportunities with respect to selectivity, self-diagnosis, low operation temperatures, and long-term stability. With respect to many key structural parameters—such as grain size, grain interconnectivity, pore size, and pore architecture—conventional synthesis methods do not allow efficient and individual control. New synthesis concepts of structure direction and structure replication provide new opportunities to create materials with defined mesoporosity and improved gas-sensing properties. The first objective of this study was to synthesize and characterize mesostructured materials—such as mesostructured carbon, zinc oxide, and cobalt oxide—by using a hard-template route and the application of gas-sensing measurement. For this purpose, mesostructured sensing materials were pasted on traditional alumina substrates, using the print-screen method.

The other objective of this study was to discover a micro-sensing device that used SOI technology and was fully CMOS-compatible. The mesostructured sensing materials were immobilized by the dielectrophoresis (DEP) process, while characterization of the structural and textural properties was carried out with X-ray diffraction (XRD), scanning electron

microscopy (SEM), transmission electron microscopy (TEM), X-ray photoelectron spectroscopy (XPS), and a surface-area analyzer. The sensing mechanisms of the mesostructured materials will also be discussed.

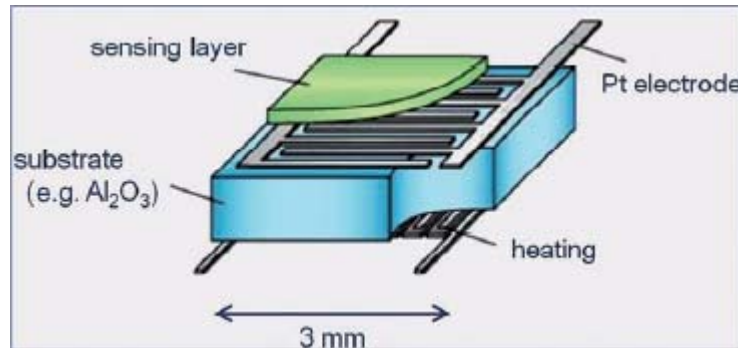


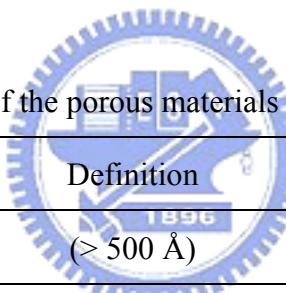
Figure 1.1 Sensor material is deposited on the interdigitated electrode [9].



Chapter 2 Mesoporous Materials: Literature Review

In 1992, a novel family of molecular sieves called M41S was launched by Mobil Corporation [16]. The pore size of these mesoporous materials were 15–100Å. These materials attracted interest due to their large pore size ($>1200 \text{ m}^2 \text{ g}^{-1}$) and tunable pore sizes. The M41S materials also provide a new approach in materials synthesis, supplanting the use of single molecules (zeolite) as templating structure-directing agents. In general, inorganic solids containing pores whose diameter range from 20 to 500 Å are considered mesoporous materials, according to IUPAC definition. Examples of mesoporous materials such as M41S, aerogels, and pillared layered structures as listed in Table 2.1.

Table 2.1. Pore size definition of the porous materials



Pore size	Definition	Examples
Macroporous	($> 500 \text{ Å}$)	Glasses
Mesoporous	($20\text{-}500 \text{ Å}$)	Aerogels, M41S
Microporous	($< 20 \text{ Å}$)	Zeolites, Activated Carbon

On the most fundamental level, the formation of mesoporous materials from inorganic precursors and organic surfactants occurs in the presence of surfactants, in a solution from solubilized inorganic precursors. Surfactants contain a hydrophilic head group and a long hydrophobic tail group within the same molecule, and they will self-organize so as to minimize contact between the incompatible ends. The type of interaction between the surfactant and the inorganic precursor is seen as a significant difference among the various synthesis routes, the formation models, and the resulting classes of mesoporous materials [17]. A liquid crystal templating (LCT) mechanism has been proposed, based on the similarity (i.e.,

lyotropic phase) between liquid crystalline surfactant assemblies and M41S [18]. Common traits include the mesostructure dependence on the hydrocarbon chain-length of the surfactant tail groups, the effects of changing of the surfactant concentrations, and the influence of organic swelling agents [19].

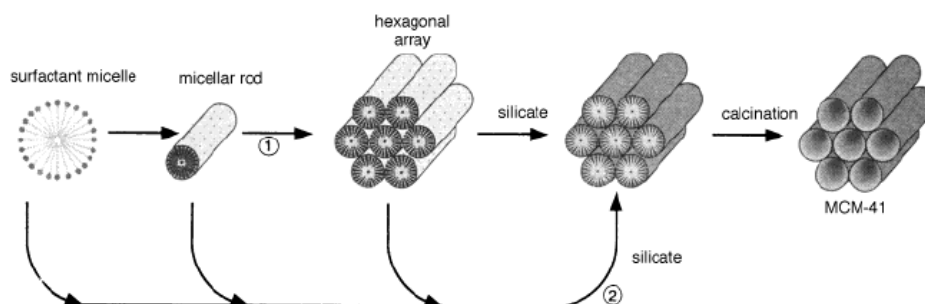


Figure 2.1 Two possible pathways for the LCT mechanism

Self-assembled molecular aggregates or supermolecular assemblies are employed as structure-directing agents, co-assembling with the inorganic materials into sophisticated nanoscale structures through favorable molecular interaction. The resultant nanoscale materials have a delicate structural ordering; thus, not only scale ordering (1.5–30 nm), but both crystalline symmetry (i.e., those that are hexagonal, lamella, and cubic) and morphologies can be tailored.

Davis et al. found that the hexagonal LC phase did not develop during MCM-41 synthesis. They propose that the formation of MCM-41 begins with the deposition of two to three monolayers of silicate precursor onto isolated surfactant micellar rods [20]. In that study, the rods were randomly ordered, eventually packing into a hexagonal mesostructures.



Figure 2.2 Assembly of silicate rods.

Steels et al. found that surfactant molecules assembled directly into the hexagonal LC phase, upon the addition of a silicate species [21]. The silicates were organized into layers, with rows of cylindrical rods intercalating between layers.

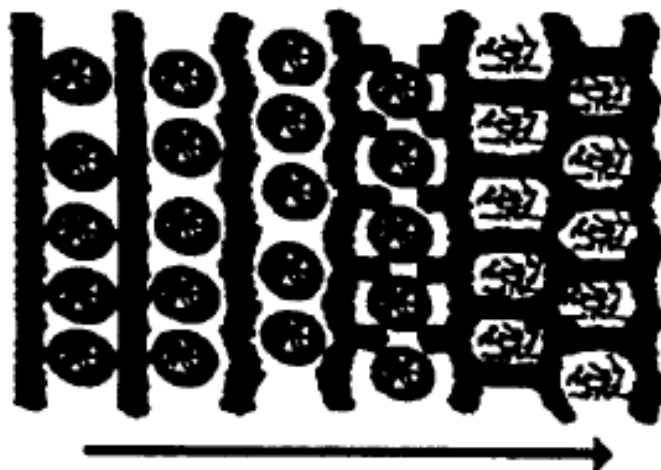


Figure 2.3 Puckering of silicate layers in the direction.

Monnier et al. and Stucky et al. indicate a novel mechanism for a lamellar phase. In that study, the phase of the synthesis mixture formed as a result of the electrostatic attraction between the anionic silicates and the cationic surfactants [22, 23].

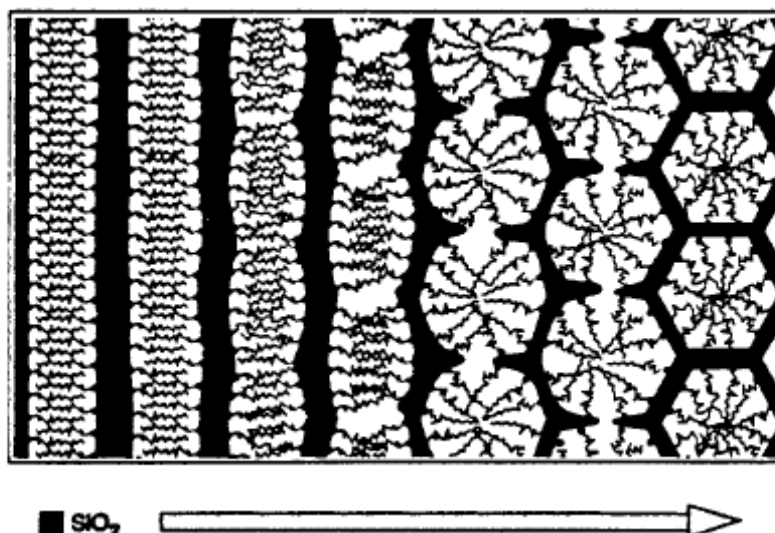


Figure 2.4 Curvature induced by charge density matching; the arrow indicates the reaction coordinate.

A lamellar-to-hexagonal phase motif accompanied by hydrated sodium silicate comprising single-layered silica sheets was found by Vartuli et al. [24]. They demonstrated that the layered structures were still retained in the kanemite-derived mesoporous materials.

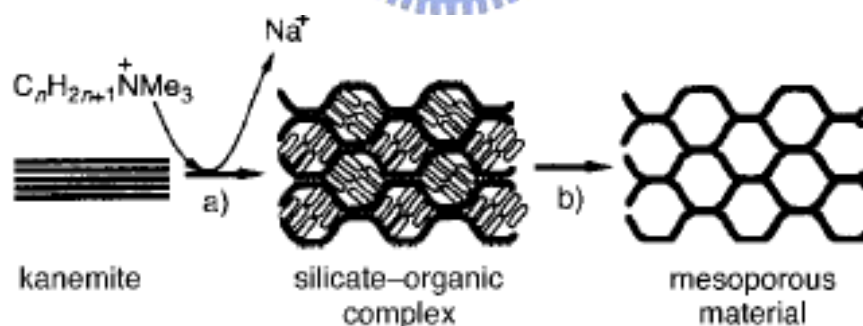


Figure 2.5 Folding of silicate sheets around intercalated surfactant molecules. (a) Ion exchange, (b) calcination.

Under synthesis conditions that prevented the condensation of silicate species—such as low temperatures and high pH—a truly cooperative self-assembly of silicates and surfactants was found. Firouzi et al. showed that a micelle solution of

cetyltrimethylammonium bromide (CTAB) transformed to a hexagonal phase in the presence of silicate anions [25]. The silicate anions ion-exchanged with the surfactant halide counteranions to form a silicotropic liquid crystal (SLC) phase that involved silicate-encrusted cylindrical micelles. The SLC phase exhibited behavior very similar to those of typical lyotropic systems,

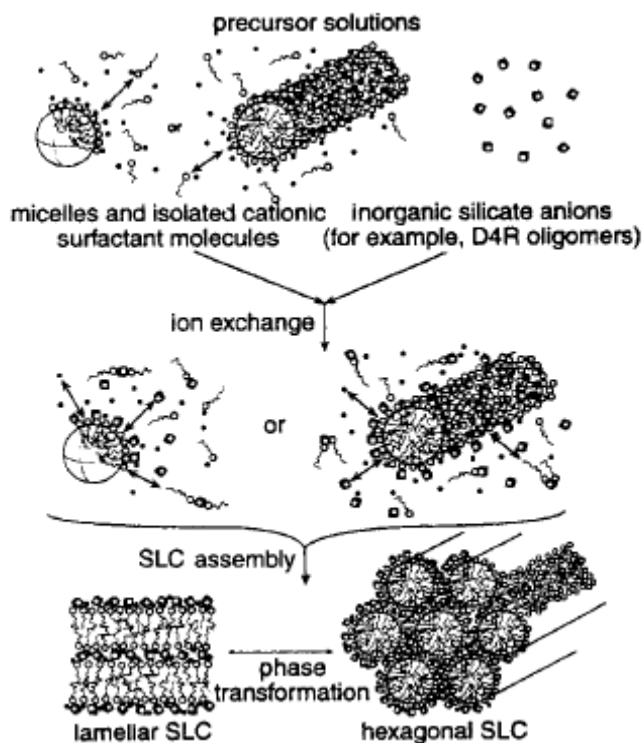


Figure 2.6 Formation of a silicotropic liquid crystal phase.

except that the surfactant concentrations were much lower and the silicate counteranions were reactive [26]. Additionally, Firouzi et al. also demonstrated the charge-balance requirement (electrostatic interaction) [25, 26]. There was a preferential bonding of the ammonium head group to multi-charged D4R $[(\text{Si}_8\text{O}_{20})^{8-}]$ silicate anions, under high pH conditions; the interaction was so strong that an alkyltrimethylammonium surfactant solution could force a silicate solution that did not contain D4R oligomers to re-equilibrate and form a D4R species. Furthermore, Fyfe and Fu were able to prepare mesostructured silicates with D4R silicates

[27]; they tried to combine D4R precursors with cetyltrimethylammonium chloride (CTAC) surfactant-produced mesostructured materials. Control of the condensation of the silicates within the mesostructure by acidic vapor treatment led to the observation of cubic, lamellar, and hexagonal phases as intermediate transformation phases. The M41S family comprises made up of three well-defined mesostructures: MCM-41, MCM-48, and MCM-50 [28]. Illustrations of the M41S family are provided in Figure 2.7. MCM-41 has a hexagonally packed array of noninterconnecting cylindrical pores,

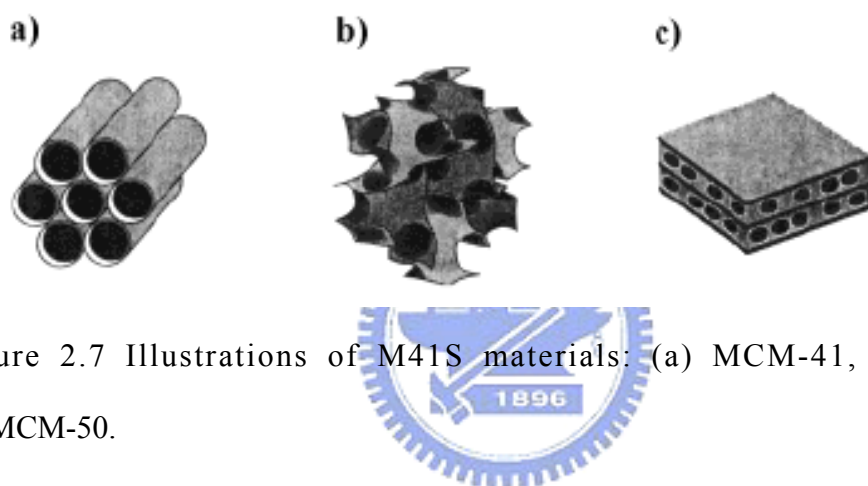


Figure 2.7 Illustrations of M41S materials: (a) MCM-41, (b) MCM-48, and (c) MCM-50.

while the structure of MCM-48 can be thought of as two intertwined networks of spherical cages that are separated by a continuous silicate framework. MCM-50, meanwhile, contains a lamellar structure in the uncalcined form.

Through the acidic route, other species considered to be in the SBA series have been synthesized [29]. These materials have thicker pore walls and a framework charge that is different from those in M41S materials, due to their different precipitation conditions and charge-balance requirements. Zhao et al. have reported the synthesis of highly ordered hexagonal mesoporous silica structures named SBA-15, by using an amphiphilic block copolymer as an organic-templating agent [30]. Poly(alkylene oxide) triblock copolymers triblock copolymers ((EO_x-PO_y-EO_x))—where EO is ethylene oxide and PO is propylene

oxide—were good candidates, owing to their mesostructural ordering properties, commercial availability, biodegradability, and cost-effectiveness. The hydrothermal stability and mechanism properties of SBA-15 were superior to those of MCM-41, because the walls of SBA-15 are thicker than those of MCM-41 with cationic surfactants. The EO species had greater hydrophilicity, causing it to interact more strongly than the hydrophobic PO species (Figure 2.8). Several morphologies of mesoporous materials—such as films, spheres, hollow spheres, and fibers—have been synthesized [31–34].

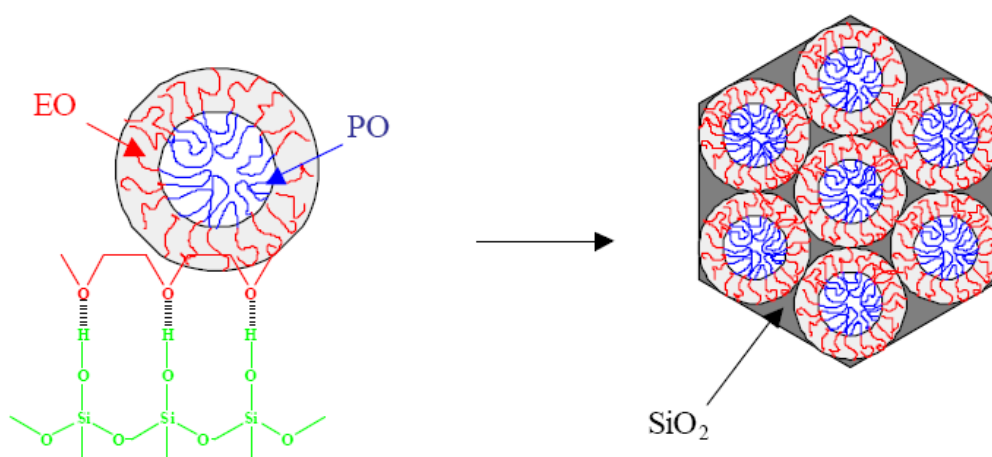


Figure 2.8 A schematic diagram of SBA-15 synthesized with triblock copolymer.

Zhao et al. and Lin et al. have each synthesized hollow mesoporous silicate spheres with hierarchically ordered structures by using bitanol as a co-surfactant [35–39]. Moreover, Zhao et al. have also demonstrated a variety of SBA-15 morphologies by using a co-surfactant, co-solvent, or electrolytes [40]. Herein, the morphology of SBA-15 strongly depended on the surface curvature energy at the interface of inorganic silica and organic copolymer species.

The large pores of mesoporous materials are formed directly by copolymers called mesostructured cellular foams (MCFs). Prior to their development, large-pore molecular sieves were much in great demand, for the separations of large molecules; the development of

SBA-15 and MCF has extended the range of mesoporous materials with pore sizes larger than 10 nm [41]. On the other hand, SBA-15 and MCF materials were synthesized with triblock copolymer (EO-PO-EO) templates and are related by phase transition from a hexagonally ordered cylindrical mesoporous structure to the mesocellular foam structure.

To date, there has been increased interest in the fabrication of nanometer-sized fine structures, because of their potential utilization in electronics and optical and micromechanical devices. There have been numerous reports of the preparation of inorganic mesoporous films, due to their potential use in separation membranes, chemical sensors, optical devices, and electronic devices such as low-k dielectric films [42–44]. Most of all, the mesoporous silica of MCM-41 and SBA-15 have conventionally been fabricated by surfactant-silicate composites from a liquid phase, under acidic or basic conditions [45–47]. A simple way to synthesize mesoporous silica films has been developed using the spin-coating and dip-coating methods [48, 49]. Recently, Kim and Ryoo have synthesized MCM-48 crystals (*Ia3d*) with a cubic structure [50], and Che et al. have reported the synthesis of SBA-1 (*Pm3n*) with a large number of facets by adjusting temperature, synthesis time, acidity, and surfactant concentrations [51]. It should be noted that ionic surfactants have been used in all reports; this is because the specific interaction between copolymer and silica is much weaker than that of ionic surfactants and inorganic species in solution.

In recent years, much work has been done in which there was use of ordered mesoporous carbon, CMK-3, and mesoporous metal oxide that were synthesized through a template method from SBA-15 mesoporous silica; in much of this work, these films were used to derive electric double-layer capacitors (EDLCs) and sensing materials [52–56].

Chapter 3 Fundamentals of Semiconductor Metal Oxide

Gas Sensors

According to Göpel and Schierbaum [57], gas sensors are devices that convert a chemical state into an electrical signal. Although many authors have provided more general or specific definitions for this kind of sensor [58], this is probably the simplest one that best fits the purpose of this work. The term “chemical state” must be understood as alluding to different concentrations or partial pressures of molecules or ions in a gas, liquid, or solid phase; if these conditions are not specified, it is often assumed that these chemical sensors are just a primary link in the proverbial measuring chain—in other words, an interface of the chemical world and electronics.

Stetter and Penrose [59] indicate that good gas sensors should provide (1) a sensitive layer, (2) information regarding changes in the chemistry of the sensitive layer, and (3) a sensitive layer on a platform, allowing transduction of the change to electric signals; furthermore, they should (4) be small in size, (5) operate in real time, and (6) be cost-effective. As stated above, every chemical sensor that has ever been made belongs to one of two domains: the physical transducer or the chemical interface layer. At the chemical interface, the analyte interacts chemically with a surface, producing a change in physical and/or chemical properties. These changes are measured by the transducer domain, which monitors this change and generates a related electrical signal.

The characteristics of semiconductor metal oxide (SMO) gas sensors are based on changes in their electrical properties in the presence of a gas. Depending on the material, this change can be due to bulk effects, surface conductance effects, or a combination of the two [60]. Consequently, oxygen has free valences that result in a basic electrical conductivity when in vacuum. The gas-dependent conduction behavior of metal oxide semiconductors

relies upon the presence of oxygen in an ambient gas (e.g., the use of air). If the oxygen concentration in the ambient gas is different from the oxygen equilibrium concentration in the bulk metal oxide, oxygen diffusion takes place and the conductivity of the metal oxide changes. This is termed the “bulk effect.” At room temperature in air, oxygen is adsorbed at any surface (including the metal oxide surface); therefore, oxygen molecules react with electrons from the metal oxide surface, and so decrease the concentration of free electrons. This leads, in the case of n-type materials, to a reduction in their conductivity. The amount of adsorbed O_2^- depends strongly on the oxygen partial pressure. If there is a reducing or oxidizing gas present in the ambient gas that is able to react with the adsorbed oxygen, the surface concentration of the adsorbed oxygen will be altered. Normally, energy must be applied externally, to overcome internal activation energies; the common operation temperatures of SMO gas sensors are therefore in the range of 50–900°C. The reaction will take place only at the surface of the heated sensor part. To understand this surface reaction, it is necessary to consider some surface chemistry concepts.

The foundation of SMO materials is controlled through the processes discussed below.

3.1 Physisorption and Chemisorption

Gas molecules on the surface cannot fully satisfy their valence or coordination requirements. The adsorption of external species that happen to be in the vicinity of the surface reduces the surface energy of the solids. Physisorption and chemisorption would, then, occur at the same time. The gas molecules are seized by van der Waals forces (physisorption), and gas molecules adsorbed on the surfaces would result in through an exchange of electrons, resulting in chemical bonds (chemisorption).

Figure 3.2 shows a diagram of oxygen desorption from a semiconducting metal oxide sensor. As one can see, the physisorbed and chemisorbed oxygen are adsorbed point defects are formed at the surface, and bulk defects are involved.

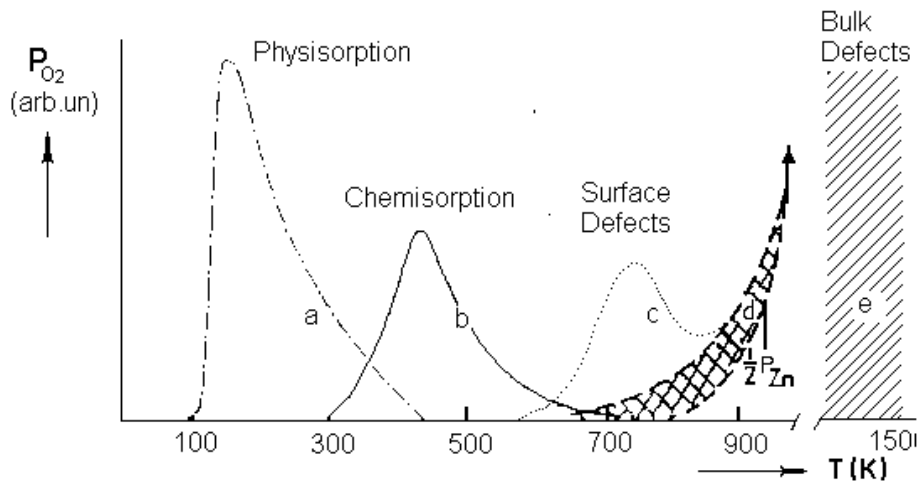


Figure 3.1 A thermal desorption spectra (TDS) of molecular oxygen on ZnO. Curve C is the first heat treatment. [61].

3.2 Charge Transfer Model (CTM)

The Charge Transfer Model (CTM) describes the interaction at the gas/metal oxide interface. It describes the chemisorption of gas molecules in terms of “ionsorption,” where molecules are free to accept or donate electrons from the bulk material. This is equivalent to the generation of a surface state with an underlying space-charge region. Whether these surface states can act as surface acceptors or donors depends on the nature of both the adsorbed gas (i.e., whether reducing or oxidizing), as well as the type of semiconductor (i.e., whether n-type or p-type). Thus, the gas adsorption leads to a band deflection near the surface [62]. To understand the CTM, it is necessary to know the band model, the Fermi distribution, and the influence of doping. A common classification of layers considers whether the injected type of the charge carrier is of the same type as the major charge carrier (termed the “accumulation layer”) or vice versa (termed the “depletion layer”) [63]. For example:

- Donors on the surface of an n-type material—which inject electrons into the conduction band—or acceptors on the surface of a p-type material—which inject holes into the valence

band—form an accumulation layer.

- Acceptors on the surface of an n-type material—which extract electrons from the valence band or donors on the surface of a p-type material—which inject electrons into the conduction band—can form a depletion layer.

Figure 3.2 shows the influence of an adsorbed electron acceptor (e.g., O_2) on an n-type and a p-type semiconductor. Owing to such a charge transfer, a positive space-charge region in the surface region is generated [62].

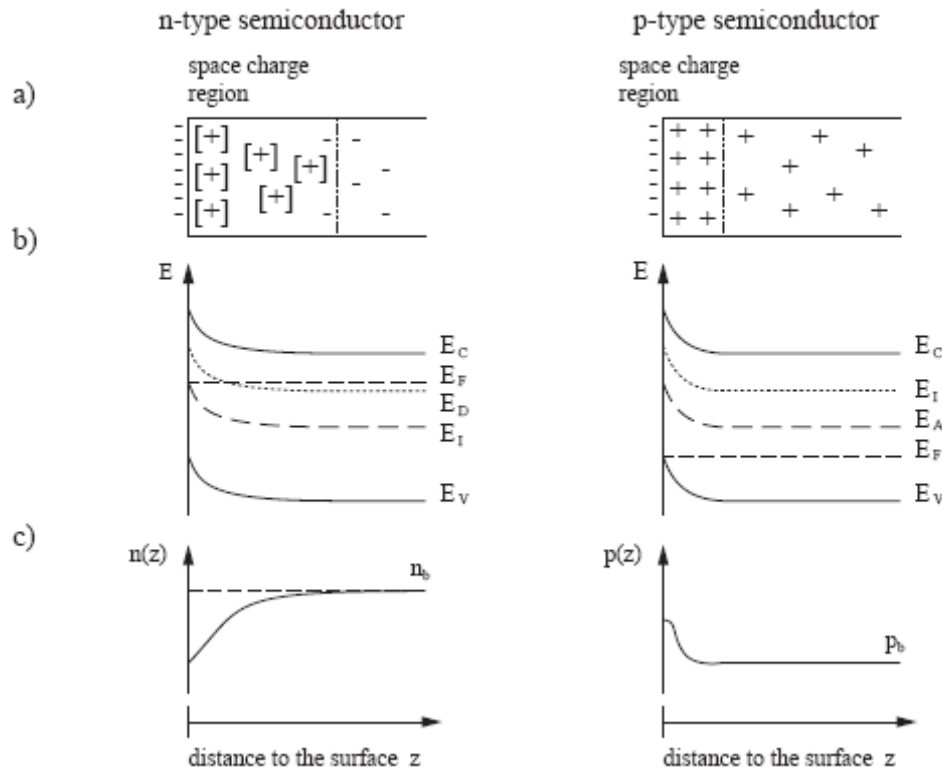


Figure 3.2 Space charge at the surface of an n-type semiconductor (left) and of a p-type semiconductor (right), due to the adsorption of an electron acceptor. (a) Distribution of the charge carrier, (b) band deflection at the semiconductor surface (c) charge carrier concentration in the conductor valence band. E_C : edge of the conduction band, E_V : edge of the valence band, E_F : Fermi level, E_D : donor level, E_A : acceptor level, E_I : intrinsic level, n_b : concentration of electrons in the bulk, p_b : concentration of holes in the bulk. [62].

3.3 Depletion Layers Effect

Each SMO gas sensor presents a depletion layer of width L in air, where L depends on the Debye length and the strength of the oxygen chemisorption. The Debye length can be expressed as:

$$L_D = (kT \varepsilon / q^2 n)^{1/2},$$

where k , T , q , e , and n are the Boltzmann constant, Kelvin temperature, electron charge, dielectric constant, and charge-carrier concentration, respectively. The thickness of the space charge layer is related to Debye length (L_D) is usually determined by:

$$L = L_D * (2eV_s / kT)^{1/2},$$

where eV_s is the surface potential and kT is thermal energy. It follows that the introduction of impurity cations inside the lattice would result in changes in L_D and L , and therefore promote or attenuate gas sensitivity, even when grain size remains the same.

Therefore, by reducing the particle size, high gas sensitivity and short response times can be achieved. Dieguez et al. showed that in the two smallest particles was found the highest density of defects, all of which could negatively influence the transport properties or act as a region for accumulating metal doping in the crystalline. Therefore, a compromise between particle size and depletion layer is ideal. To date, SMO crystals deposited by thin-film techniques have been polycrystalline; this enables the diffusion of gases along the grain boundaries, allowing the gases to influence each single grain. In this case, the ratio of grain size to effective Debye length has a significant effect on the gas-sensing behavior. To explain this behavior, an n-type semiconductor with adsorbed electron acceptors is considered (Figure 3.3); if the Debye length is smaller than half the grain size (Figure 3.3, left), then the conduction is dominated through the charge carrier depletion at the grain edges. This results in a band bending at the interface between each single grain. In the case of a larger Debye length (Figure 3.3, right), the charge depletion occurs in the whole grain and results in a movement of the complete conduction band relative to the Fermi level.

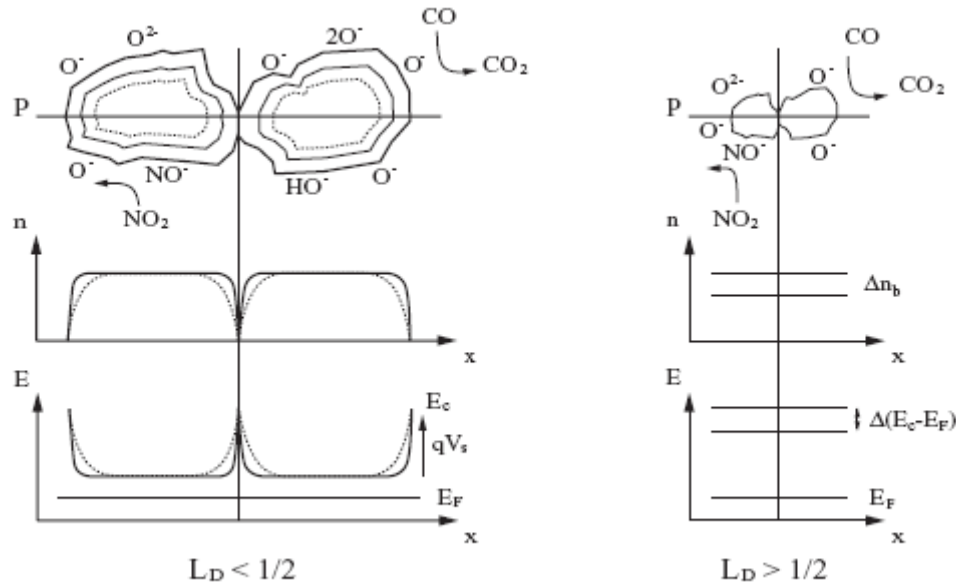


Figure 3.3 Charge carrier concentration n and conduction band E_C for the contact position of grain boundaries, for a grain with a Debye-length (L_D) less than a half-grain size on the left side and a grain with a Debye-length more than a half-grain size on the right side.

3.4 Neck-controlled and Grain Boundary Effect

SMO gas sensors with small grain size have high gas sensitivity. However, grains are connected by neck and grain boundaries. The model combines the neck mechanism and grain boundary mechanism, because there is a charge transfer between the neck and grain boundaries. Conducting electrons should move across a potential barrier when the grain boundaries make contact. Ihokura et al. has indicated that the barrier is high, caused oxygen's rate of adsorption is lower than that of target gases [64].

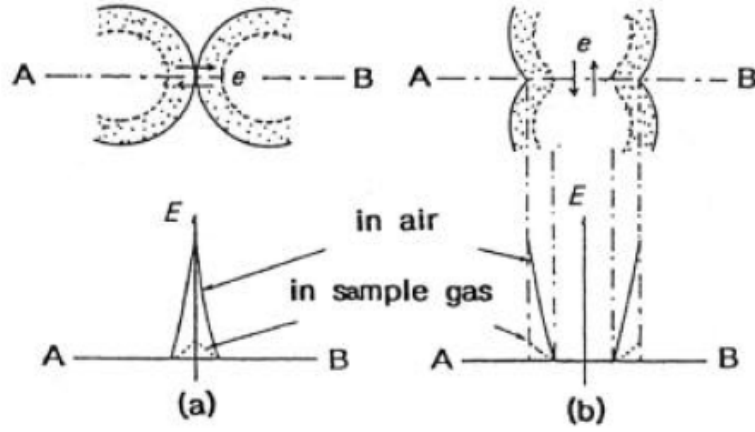


Figure 3.4 Surface space charge layer and electron transport between grain and target gases. (a) Grain boundaries, (b) necks. E: Potential energy of electrons.

When $D \gg 2L$, it is apparent that the gas sensitivity is essentially independent of grain size.

When electrons transferred to a channel of nearby necks (Figure 3.4), the aperture of the channel is modulated by with the surface spacer layer; this is consistent with the findings of Mitsudo [65]. It is narrow in air, because of oxygen adsorption that occurs while a target gas arrives to consume adsorbed oxygen, leading to gas-dependant electric resistance. On the other hand, it is assumed that the space charge layer is formed to the depth of L and the electron concentration is constant, when the electron concentration in the core region is as shown in Figure 3.5. When the mobility of electrons is constant, the gas sensitivity can be expressed by:

$$S = R_a / R_g = (x-1)^2 + n_L(g) / n_0 [x^2 - (x-1)^2] / (x-1)^2 + n_L(a) / n_0 [x^2 - (x-1)^2]$$

where $x = X / 2L$, and $n_L(g)$, and $n_L(a)$ are electron concentration in air and in target gas, respectively.

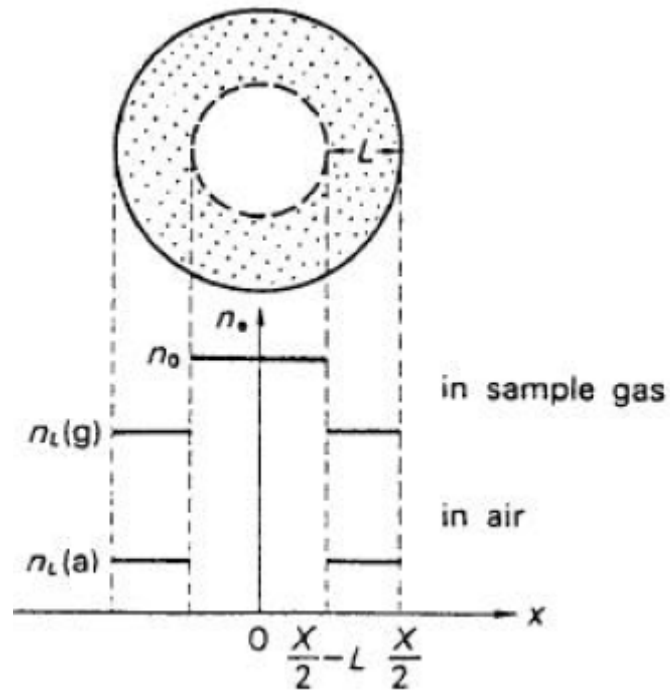


Figure 3.5 Assumed electron concentration profiles at the cross-section of a neck.

A simplified model consisting of a large number of necks and a small number of grain boundary contacts is demonstrated as a 1D chain of particles. The following three cases are differentiated, according to the value of D and $2L$ (Figure 3.6):

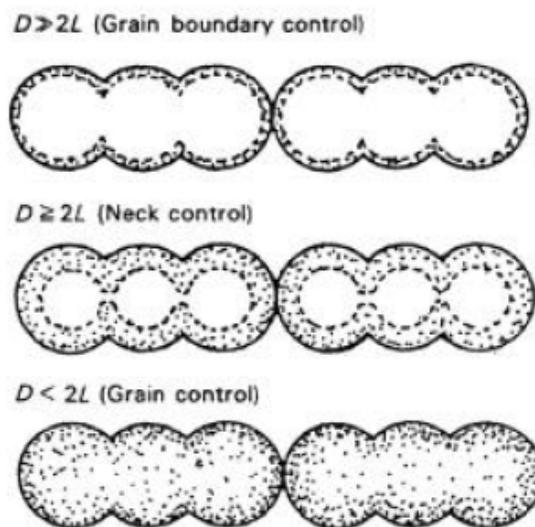


Figure 3.6 Schematic diagram of grain-size effect of nanoparticles.

- (a) $D \gg 2L$ (Grain boundary control). The electron channel is too wide, and the resistance at the grain boundary contacts determines the whole resistance, giving rise to a gas sensitivity that is independent of D .
- (b) $D = 2L$ (Neck control). Each channel is narrow, and since the number of necks is greater than the number of grain boundary contacts, the resistance of the entire element would rise to the neck size-dependent gas-sensitivity level.
- (c) $D < 2L$ (Grain control). Each particle is included as a whole in the space-charge region. The electron transport at any place inside the particle becomes susceptible to the surface effect, and the whole of the electrical resistance and gas sensitivity will be controlled by grains at a sufficiently small D value. The outer part of each grain is more susceptible to gases than the inner part; this likely explains the increase in gas sensitivity as D decreases, though quantitative measurements have yet to be taken.

If D is small, the depletion region will drop down the neck conduction channel. Electrons are significantly scattered by the grain boundaries, and the mobility is therefore reduced [66].

3.5 Schottky Contact

It has been proven that a change can occur in the Schottky barrier height, on account of the electron concentration adsorbed on the surface [67]. When gas molecules are adsorbed on the semiconductor surface, the Fermi level of the semiconductor adjusts to the dominating presence of the metal; the free carrier density is much higher than that of the semiconductors, and the Fermi level is lowered by an amount equal to the difference between the two work functions. An adjustment of the Fermi level occurs when there exists a thin dielectric layer, such as WO_3 , between the metal and the semiconductor. This scenario is illustrated in Figure 3.7, which describes the energy band diagram of the Schottky barrier structure in the absence of the surface states in the semiconductor [68].

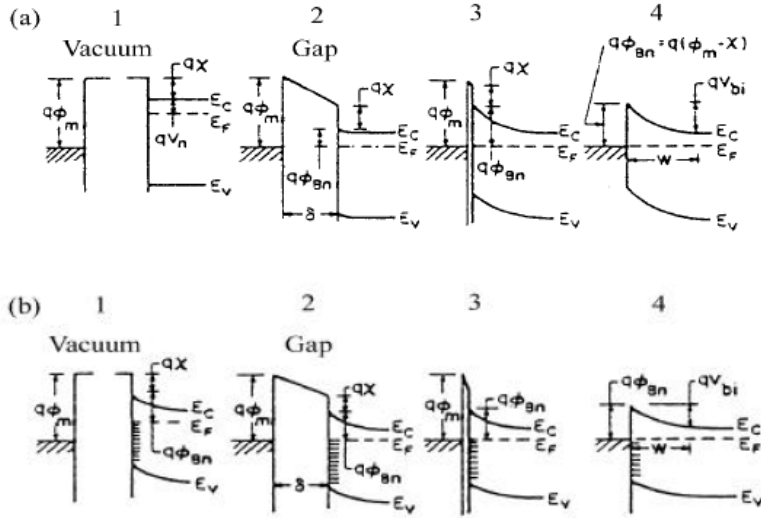


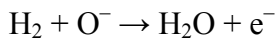
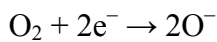
Figure 3.7 (a) Energy-band diagram of metal-oxide-n-type semiconductor junction: (I) Before contact, (II) after contact and thermodynamic equilibrium is attained, in the presence of a gap (or an insulating dielectric) of thickness d , (III) when d is comparable to interatomic distance, and (IV) in the limit $d=0$ (metal-semiconductor junction).

If the barrier is high enough, the Schottky diode is rectifying (i.e., the current-voltage (I-V) characteristics are not highly linear), behaving like an ordinary p-n junction in series with a thin tunneling layer. Upon exposure to certain gases, the Schottky barrier is affected. The dependence of metal work function ($q\phi_m$) indicates that a device can become gas-sensitive when Schottky diodes are exposed to gases that alter the metal work function. The bending of the semiconductor bands at the interface occurs down to a depth W , which is called the depletion width or the surface charge layer. Sricastava et al. demonstrated that the electrical behavior of n-type SMO-sensing material with active grain boundaries are controlled by the formation of double Schottky potential barriers at the interface between adjacent grains. The formation is the result of charge-trapping at the interface. Trap states present at the interfaces can capture majority carriers; therefore, the bending of the band

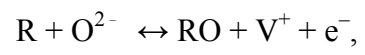
occurs and forms a barrier at the interface. While this material is exposed to under the air conditions, oxygen molecules are adsorbed at the surface. The adsorbed oxygen accepts electrons from the trap states present at the interface of adjacent grains, to form O_2^- , O^- , and O^{2-} ions—thus decreasing the concentration of the number of charge carriers nearby the surface and causing a depletion of the raised layer. When exposed to a reduced gas in air, the co-adsorption and mutual interaction between the reactants (i.e., reducing gas and oxygen gas) result in an oxidation of reducing gas at the surface [69]. The oxidation phenomenon helps in the removal of oxygen ions from the surface, resulting in a decrease of barrier and an increase in conductance.

3.6 Oxygen Vacancy

Several models explain the resistance change of SMO-sensing materials. In air conditions, the oxygen that would otherwise adsorb at the surface would dissociate to O^- . The electron extraction tends to increase resistance. In the presence of a combustible gas (i.e., hydrogen), that gas would react with the adsorbed O^- to form water and the electrons would be re-injected into the semiconductor, leading to a tendency to decrease the resistance.



A competition results between oxygen-removing electrons and the reactive gas that restores these electrons. The steady-state value of the resistance depends on the concentration of the combustible gas. Another model shows that, if chemically active, the reactive gas would exist or coexist and extract lattice oxygen from the metal oxide, leaving vacancies that act as donors. The oxygen from the air tends to re-oxidize the metal oxide, removing donor vacancies; in this way, there is a competition between oxygen-removing donor vacancies and gas-producing donor vacancies. The density of the donor vacancies depends only on the concentration of gas, because the oxygen pressure is constant.



where O is lattice oxygen, V^+ is oxygen ion vacancy, and R is the reactive gas.



Chapter 4 Experimental Methods

4.1 Synthesis of Mesoporous Materials

4.1.1 Synthesis of Mesoporous Silica Template

Samples of the hexagonal structure mesoporous silica SBA-15 were prepared using a simple hydrothermal process, according to methods found in the literature [70, 71]. In the batch synthesis, 4 g of poly(alkylene oxide) triblock copolymer P123 ($\text{EO}_{20}\text{PO}_{70}\text{EO}_{20}$, EO = ethylene, PO = propylene, BASF) as the structure-directing agent was dissolved into 30 g of deionized water and 120 g of 2 M HCl solution under stirring at 40°C. This was followed by the addition of 8.6 g of TEOS into the solution; it served as the silica source. The mixture was kept under static conditions in an oven for 20 h at 40°C. Subsequently, the mixture was placed in an oven at 100°C for 24 h for hydrothermal treatment. The molar ratio of composition was 0.017 P123/0.02 TEOS/0.12 HCl/3.92 H_2O . Following hydrothermal treatment, the solid product was filtered, washed with deionized water, dried at 120°C overnight, and calcined at 560°C. To investigate the interconnectivity of silica templates, the mixtures were treated at different hydrothermal temperatures; the resultant SBA-15 samples are denoted as SBA-40d, SBA-60d, and SBA-100d.

4.1.2 Synthesis of mesoporous carbon

The carbon replicas were derived by the presence of silica templates, sucrose, and H_2SO_4 [72]. Briefly, 1 g SBA-15 was added to a solution obtained by dissolving 1.25 g sucrose and 0.14 g H_2SO_4 in 5 g of H_2O . The mixture was heated in an oven for 6 h at 100°C. Subsequently, the oven temperature was raised to 433 K for another 6 h. The sample turned dark brown or black during heat treatment in the oven. The silica sample was treated again at 100°C and 160°C, using the same drying oven, following the addition of 0.8 g sucrose, 0.09 g H_2SO_4 , and 5 g H_2O . Carbonization was completed via pyrolysis with heating, to typically

900°C under an argon atmosphere. The carbon-silica composite obtained after pyrolysis was washed with 5 wt% hydrofluoric acid at room temperature, to remove the silica template. The template-free carbon product thus obtained was filtered, washed with ethanol, and dried at 393 K. All samples were denoted as Suc-40d, Suc-60d, and Suc-100d.

4.1.3 Synthesis of mesostructured metal oxide materials

The mesoporous metal oxide samples were synthesized using mesoporous silica and mesoporous carbon templates. To synthesize mesoporous cobalt oxide, mesoporous silica was used as the template. Mesostructured cobalt oxide materials were prepared using SBA-15, along with different interconnectivity networks as templates. Generally, a mixture of $\text{Co}(\text{NO}_3)_2 \cdot 6\text{H}_2\text{O}$ (0.8 M) and SBA-15 (0.2 g) was dissolved in ethanol and stirred for 1 h. The resultant materials were then calcined at a temperature of 450°C for 6 h. Finally, the silica template was removed using 5% hydrofluoric (HF) solution the black-colored Co_3O_4 materials were recovered by centrifugation and dried at a temperature of 50°C overnight. The samples obtained were denoted as Co-hex-40d, Co-hex-60d, and Co-hex-100d.

Previously, the mesostructured cobalt oxide was synthesized by using mesoporous silica as a template. However, mesostructured ZnO cannot synthesize with mesoporous silica, because the removal of the silica templates utilizes HF or concentrated sodium hydroxide (NaOH) solutions. Mesostructured ZnO is unsuitable for this purpose, as it is soluble when the pH is very low or very high. Therefore, mesoporous carbon is used instead of mesoporous silica as the solid template for synthesizing mesoporous ZnO. The mesoporous carbon is first prepared through a structure replication procedure, and then a mesoporous metal oxide is infused into the replica. Herein, mesostructured ZnO was prepared by immersing 0.5 g CMK-3 carbon in 20 mL of a solution comprising $\text{Zn}(\text{NO}_3)_2$ in THF (1.5 mol L^{-1}) and stirring at room temperature for 6 h. After filtration, the impregnated carbon was dried at ambient temperature, heated in an air atmosphere to 300°C and at a constant rate of 2.5 K min^{-1} , and

kept at that temperature for 2 h to convert zinc nitrate to zinc oxide. This procedure was repeated twice. The resultant product was a powder lacking any specific particle morphology.

4.2 Fabrication of mesostructure-sensing device

4.2.1 Fabrication of thick-film sensor device

Thick-film gas sensors were obtained via the print-screen of a paste based on alumina substrates. The alumina substrates ($5 \times 25 \times 0.5$ mm) were cleaned with acetone, alcohol, and deionized water in an ultrasonic machine. The platinum electrodes were deposited by an E-gun on the substrate. The electrodes were interdigitated, with 0.3-mm widths and 0.2-mm lengths. The mesostructured metal oxide samples were mixed with an appropriate amount of organic solvent until a homogeneous mixture was obtained. Finally, the mixture was printed on the alumina substrates, using a print-screen machine.

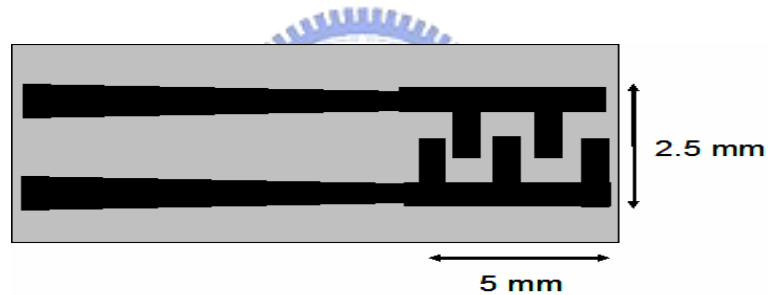


Figure 4.1 Schematic of the alumina substrates with the interdigitated electrodes.

4.2.2 Fabrication of thin-film sensors

To reduce power consumption, a micro-sensor device was fabricated on the silicon-based membrane, which was embedded with platinum interdigitating electrodes and a micro-heater (see Figure 4.2).

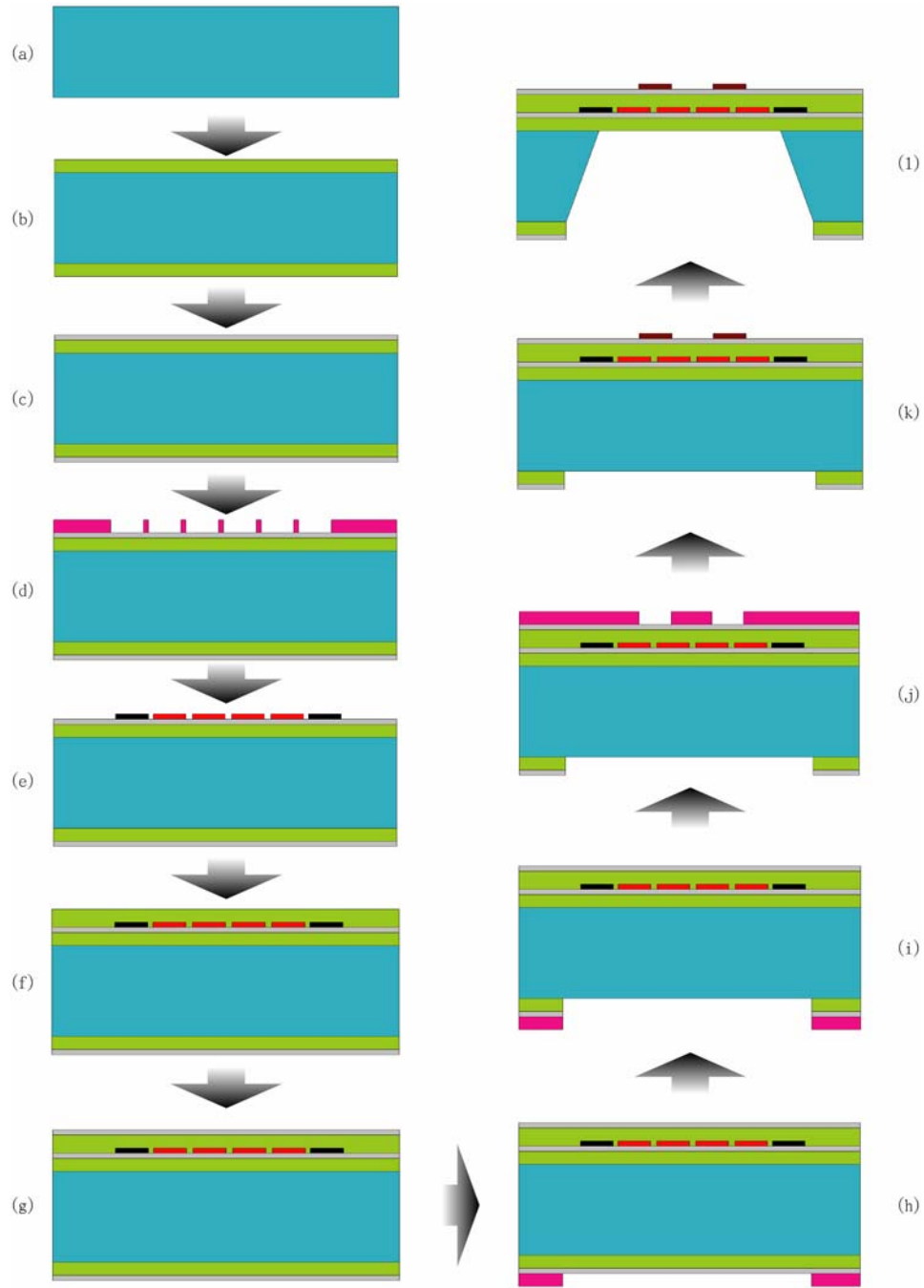


Figure 4.2 Fabrication schematic diagram of the micro-sensor device.

The details are as follows:

(a–b) A 2-μm-thick SiO₂ layer was thermally grown on a p-type silicon wafer bearing a thickness of 500 μm.

(c) A 200-nm Si₃N₄ deposition was applied over the SiO₂ layer, using low-pressure chemical

vapor deposition (LPCVD).

(d–e) A thin, 240-nm film of Cr was deposited onto the Si_3N_4 and photoresist layers by DC-sputtering on the front side of the wafer. The Cr-resistant heater and sensor were readily formed using the lift-off technique.

(f) A 2- μm -thick SiO_2 layer was deposited over the heater, using PECVD.

(g) A 200-nm Si_3N_4 deposition was applied over the SiO_2 layer, using PECVD.

(h–i) A square window pattern was opened through the SiO_2 and Si_3N_4 layers on the back side of the wafer, using photolithography; it was then etched using a reactive ion etch (RIE). Resistance was then etched by RIE, with O_2 .

(j–k) A 240-nm-thick Pt film was deposited on the front SiO_2 layer by DC-sputtering, which was then patterned to define the bonding pads. Again, the pair of electrodes was created by using the lift-off technique.

(l) To achieve excellent thermal isolation and reduce thermal mass, the membrane was fabricated via KOH anisotropic etching on the back side of the wafer; a 2- μm -thick layer of thermal oxide was applied as an etch stop.

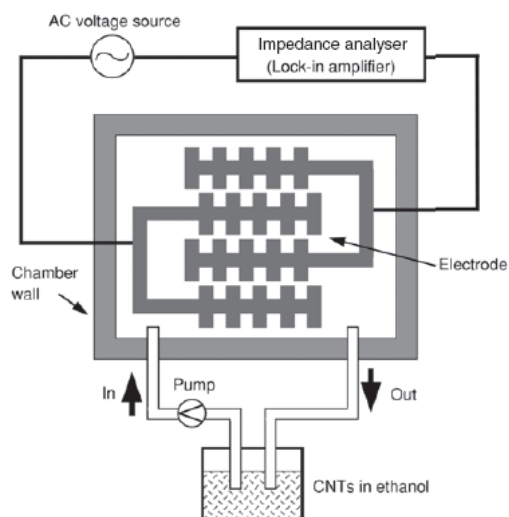


Figure 4.3 Schematic diagram of the DEP system [73].

All sensing materials were immobilized on the micro-sensor device, using the DEP process. All experiments were carried out at room temperature. The experiment set-up consisted of a function generator, an oscilloscope, and a microscope. The function generator, which included a sinusoidal wave output, was used to generate the drive signal. Different drive signals—in the range of 1–10 V, peak-to-peak, with frequencies in the range of 1–3 MHz—were used during testing. First we chose the original samples, and the gaps between them were an average of 20 μm each. A 10-V voltage with a 1-MHz frequency was applied to the interdigitated-castellated design. The devices were fixed on a chip holder, which was connected to the AC signal source (GW Instek GFG-3015 function generator) and the electrodes. The chip holder was then mounted on a microscope for the real-time observation of mesostructured metal oxides. A photograph of an unused array is provided in Figure 4.4(a). After 180 min of collecting mesostructured metal oxides, the array was viewed under an optical microscope; an image thereof is shown in Figure 4.4(b).

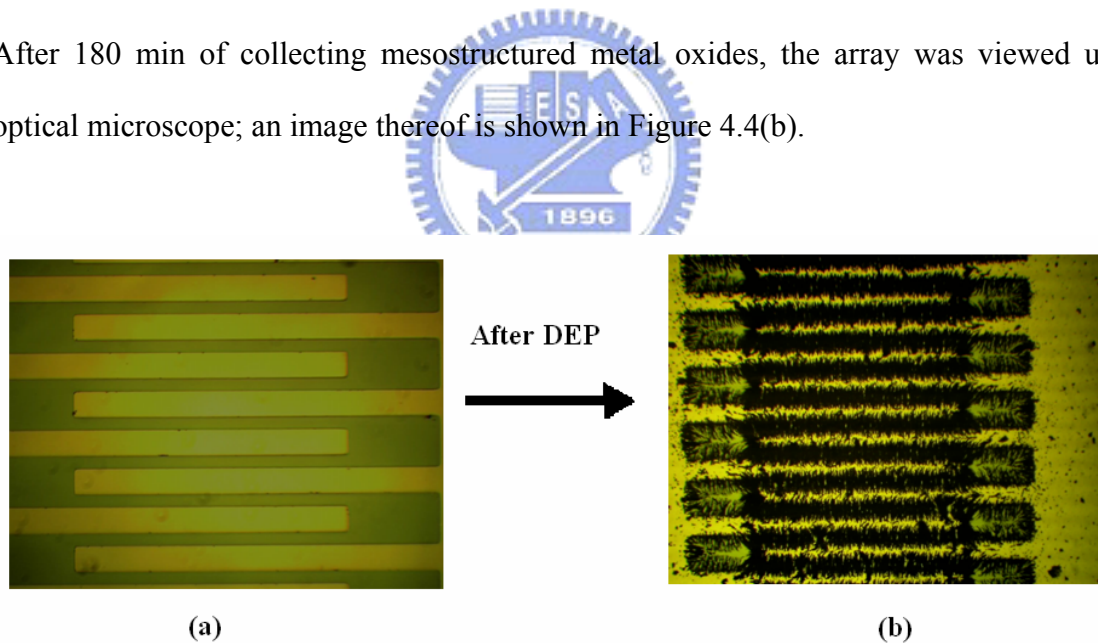


Figure 4.4 OM images: (a) Before the DEP immobilized and (b) after the DEP immobilized the mesostructured metal oxide samples.

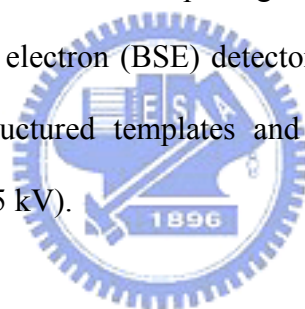
4.3 Characterization

4.3.1 X-ray diffraction (XRD) patterns

Bade D1 involves a powerful X-ray diffractometer that is employed to identify the phases and determine the structural properties of mesostructured sensing materials. The highly ordered symmetries of the mesostructured gas-sensing materials were identified using low-angle XRD patterns, where the diffraction patterns ranged from 0.5° to 3° ; otherwise, the crystallites of the mesostructured sensing materials were analyzed using wide-angle diffraction patterns, where the patterns ranged from 20° to 70° .

4.3.2 Field-emission scanning electron microscopy (FE-SEM)

FE-SEM was used to observe the morphologies of the specimens. SEM uses second electron (SE) or backscattered electron (BSE) detectors that pass the signal to form images. The topology of the mesostructured templates and metal oxides were characterized by FE-SEM (JOEL JSM 6700F, 15 kV).



4.3.3 Transmission electron microscopy (TEM)

The morphologies of the mesostructured sensing materials were examined by TEM (JOEL 2010, 200 kV), and the crystalline of the mesostructured-sensing materials were determined by using selected areas electron diffraction (SAED) patterns.

4.3.4 Differential thermal and thermogravimetry analysis (DTA/TGA) measurement

Decomposition of the mesostructured materials was determined using a TA Q500 DTA/TGA analyzer. The composites were examined from 25°C to 700°C (i.e., a heating rate of $10^\circ\text{C}/\text{min}$).

4.3.5 X-ray photoelectron spectroscopy (XPS) [74]

XPS measurements were carried out using a PHI 1600 (Perkin Elmer) with a Mg K α X-ray at 250 W. The analyzer angle of the X-ray source was 54.7°. Based on the high-resolution spherical capacitor analyzer (SCA), the energy resolution was 1.5 eV for the survey scan spectra.

4.4 Gas-sensing measurement

A diagram of the testing chamber is shown in Figure 4.5.

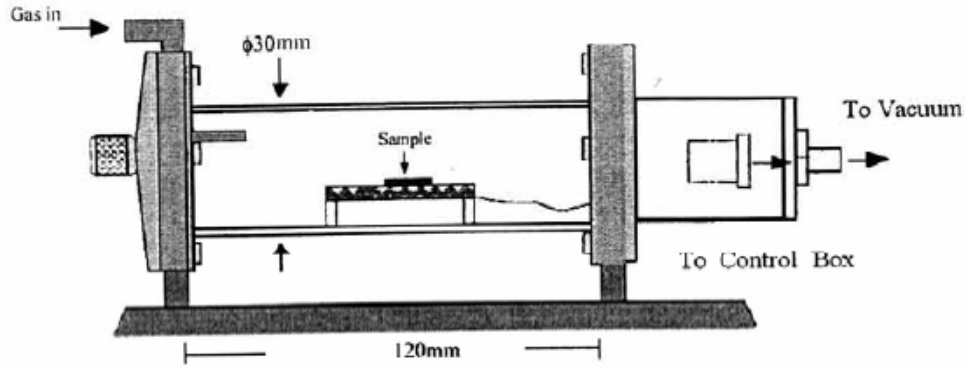


Figure 4.5 The diagram of the mesostructured materials testing chamber.

The purpose of this study was to determine the optimal conditions of mesostructured gas sensors for gas-detecting, including operating temperature, gas concentrations, response time, and recovery times. To that end, we defined the response and recovery times as follows, respectively: $\zeta_{\text{res}} = t_{90\%} - t_{10\%}$, where $t_{100\%}$ is the time at which the conductance has reached the stable state, and $\zeta_{\text{rec}} = t_{10\%} - t_{90\%}$ [75]. In general, the sensitivity of the gas-sensing materials was defined as the percentage change of the sensor resistance present in the target gas and dried air. The definition of the sensing materials is as follows (S%):

$$S\% = (R_{\text{gas}} - R_{\text{air}} / R_{\text{air}}) \times 100 \quad (\text{For p-type materials})$$

Otherwise, it was defined as:

$$S\% = (R_{\text{air}} - R_{\text{gas}} / R_{\text{air}}) \times 100$$

(For n-type materials),

where R_{air} is the resistance in dried air and R_{gas} is the resistance in the target gas.

Sensors were placed in a furnace test chamber. A continuous flow of gas (100 ml/min) passed through the chamber, making the pressure in the chamber nearly atmospheric. The desired gas concentration was obtained by mixing the appropriate flows of gases by means of mass flow controllers the electrical resistance response during testing was monitored by using a precision analyzer (Keithley 2400).



Chapter 5 Results and Discussion

5.1 Mesoporous silica template

5.1.1 Synthesis of SBA-15 at different temperatures

Recently, hexagonal-templated silica with a large surface area ($700\text{--}900\text{ m}^2\text{ g}^{-1}$), large pore size ($5\text{--}9\text{ nm}$), and thick walls ($3.5\text{--}5.3\text{ nm}$), called SBA-15, has been detailed by Zhao et al. [76, 77]. The SBA-15 synthesizes with non-ionic surfactants, displays excellent interfacial stabilization properties and is low-cost, nontoxic, and biodegradable. Figure 5.1 shows the XRD patterns of as-synthesized SBA-15, prepared with $\text{EO}_{20}\text{PO}_{70}\text{EO}_{20}$ as the structure-directing agent. This figure shows that there are three obvious well-solved peaks that can be indexed as (100), (110), and (200) diffraction peaks with $p6mm$ hexagonal symmetry. For the as-synthesized SBA-15, the intensity of the (100) peak reflects a d-spacing of 9.6 nm , accompanied by a larger cell parameter whose a_0 value was 11.1 nm . To show the morphology of the SBA-15 template, an SEM image of SBA-15 is provided in Figure 5.2. A rod-like structure with a $2\text{-}\mu\text{m}$ length and $400\text{-}\mu\text{m}$ diameter can be seen in the square regions. Some aggregate of SBA-15 can also be observed in the elliptical regions.

The nitrogen adsorption-desorption isotherm and corresponding pore-size distribution is shown in Figure 5.3. The isotherm reveals a well-resolved type-IV isotherm, with a sharp capillary condensation step indicative of mesopores that are narrowly distributed in size. The surface area, pore size, and total pore volume of the SBA-15 was $914.2\text{ m}^2\text{ g}^{-1}$, 9.02 nm , and $1.3\text{ cm}^3\text{ g}^{-1}$, respectively. The SBA-15 has a larger pore size and pore volume than MCM-41; on the other hand, the mean thickness of SBA-15 is about 5 nm , which is substantially thicker than the pore wall of MCM-41 silica ($1\text{--}2\text{ nm}$). Thus, SBA-15 exhibits the excellent hydrothermal properties, mechanism stability, and rapid catalysis reactions.

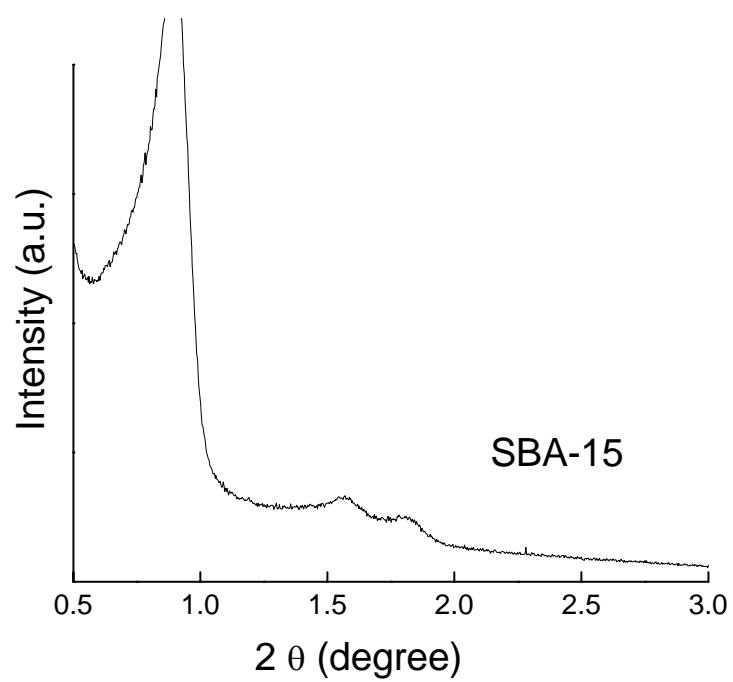


Figure 5.1 XRD patterns of as-synthesized SBA-15 template.

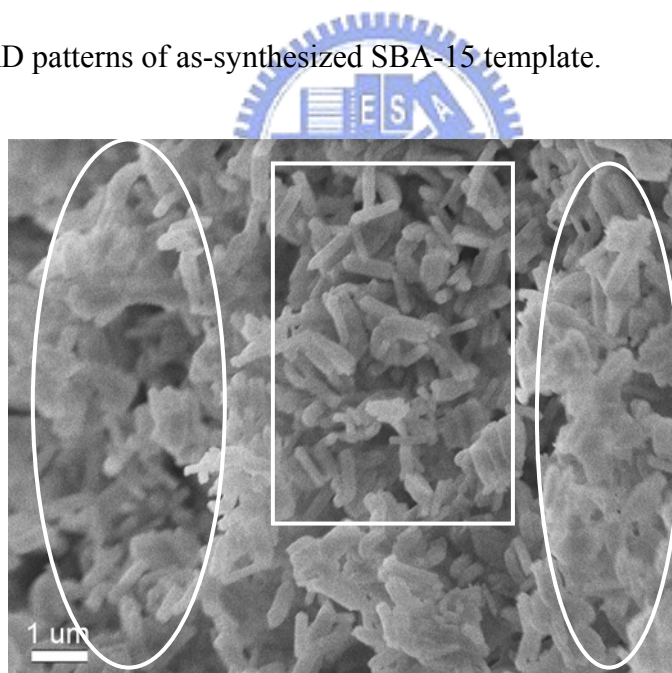


Figure 5.2 SEM image of as-synthesized SBA-15 template.

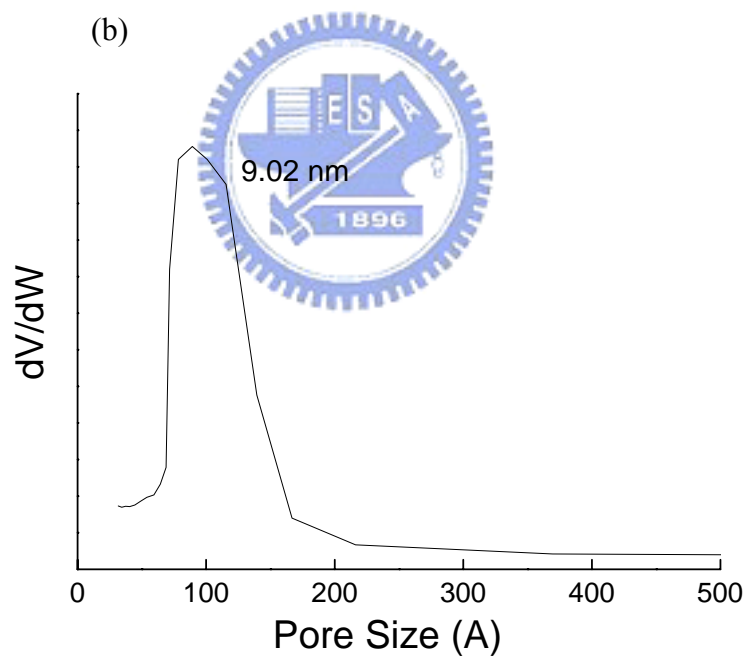
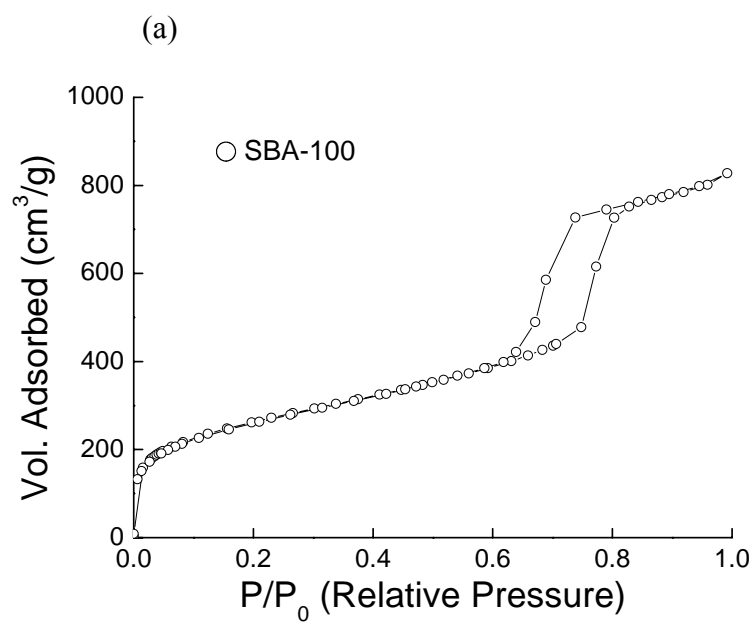


Figure 5.3 (a) Nitrogen isotherms of as-synthesized SBA-15 and (b) the corresponding pore-size distribution.

In general, variations in aging temperature are not only affected by the morphology, microporosity, and connection, but also by the tuned pore size and different silica pore-wall thicknesses [78]. Figure 5.4 shows the XRD patterns of SBA-15 synthesized at 40°C, 60°C, and 100°C. The diffraction pattern of SBA-100d shows three peaks that can be indexed according to a hexagonal array of mesopores, as for MCM-41; reflections due to the diffraction planes (100), (110), and (200) are observed. However, it can be seen that only one peak can be obtained with SBA-40d and SBA-60d. For the SBA-15 synthesized at a different temperature (i.e., from 40°C to 100°C), the cell parameter of the SBA-15 was different. The cell parameter of SBA-100d was around 11.1 nm; however, shrinking was observed for the SBA-15 synthesized between 40°C and 60°C (9 nm), likely due to the incomplete condensation of silica at low temperatures. For samples prepared at temperatures above 80°C, the cell parameter of SBA-15 sample was 11 nm. Figure 5.5 reports the nitrogen adsorption-desorption isotherms and pore-size distributions, respectively, for the series of SBA-15 materials synthesized with an increasing temperature during hydrothermal treatment. The sorption isotherms for the different calcined samples all remained well-resolved type-IV isotherms, with a sharp capillary condensation step indicative of mesopores that were narrowly distributed in size, irrespective of temperature. The shift of the capillary condensation step to a higher relative pressure and an increased temperature with mesopore size is also indicated by the evolving pore-size distribution curves. The surface area, pore size, and total pore volume increased sensibly, with an increase in temperature. The surface areas of all samples increased from 578.9 to 914.2 m² g⁻¹, the pore size from 4.5 to 9.0 nm, and the total pore volume from 0.61 to 1.3 cm³ g⁻¹, respectively.

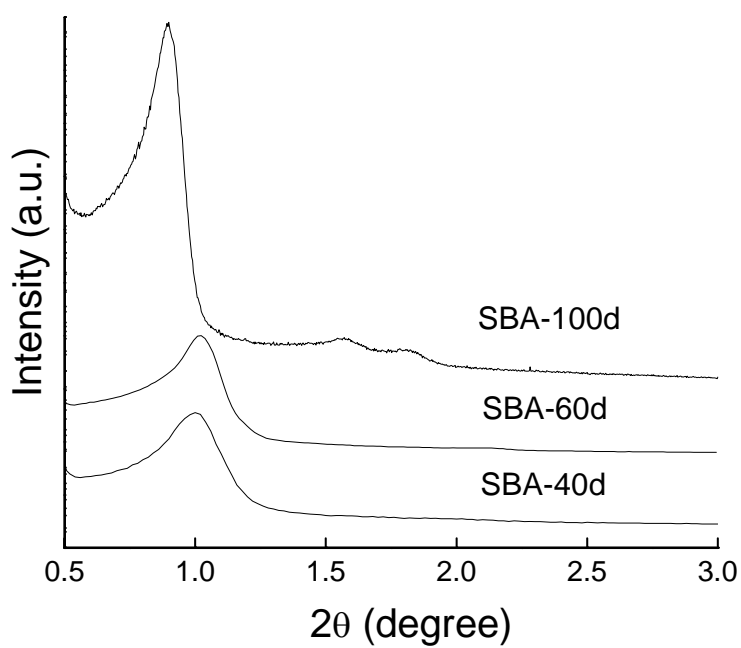
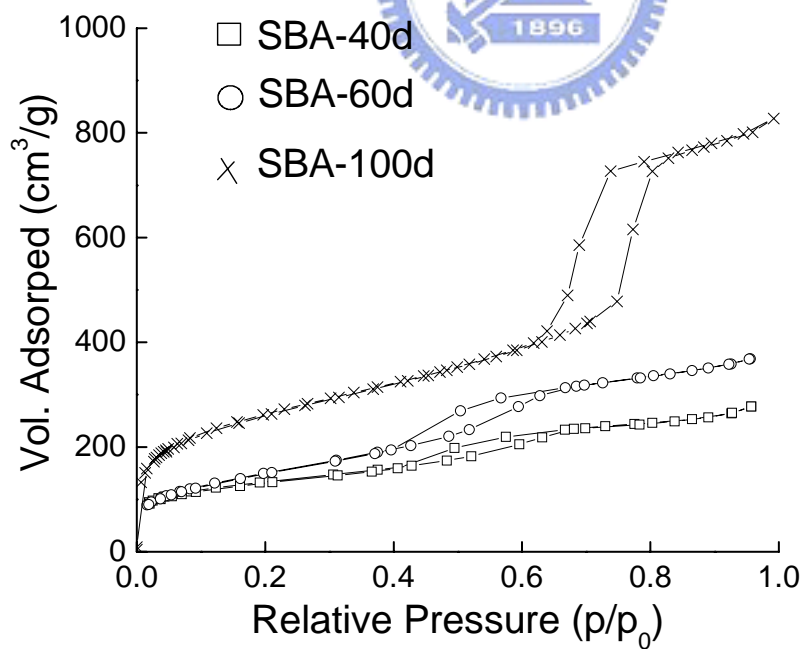


Figure 5.4 XRD patterns of SBA-15 synthesized at 40°C, 60°C, and 100°C.



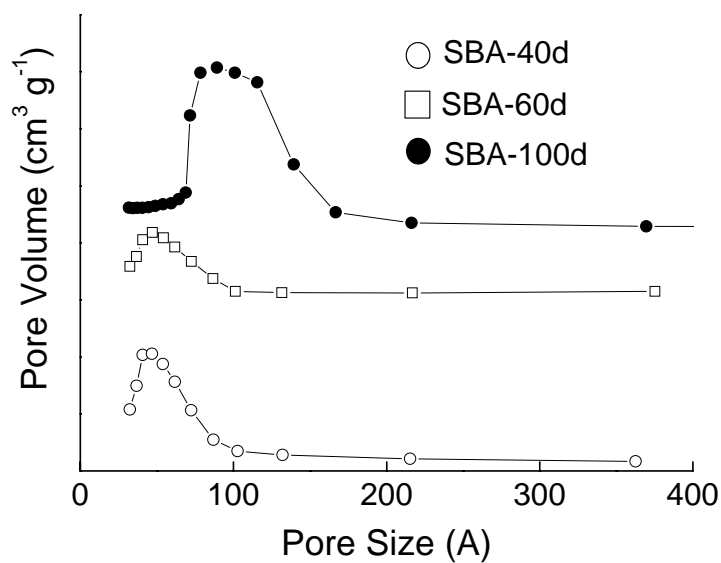
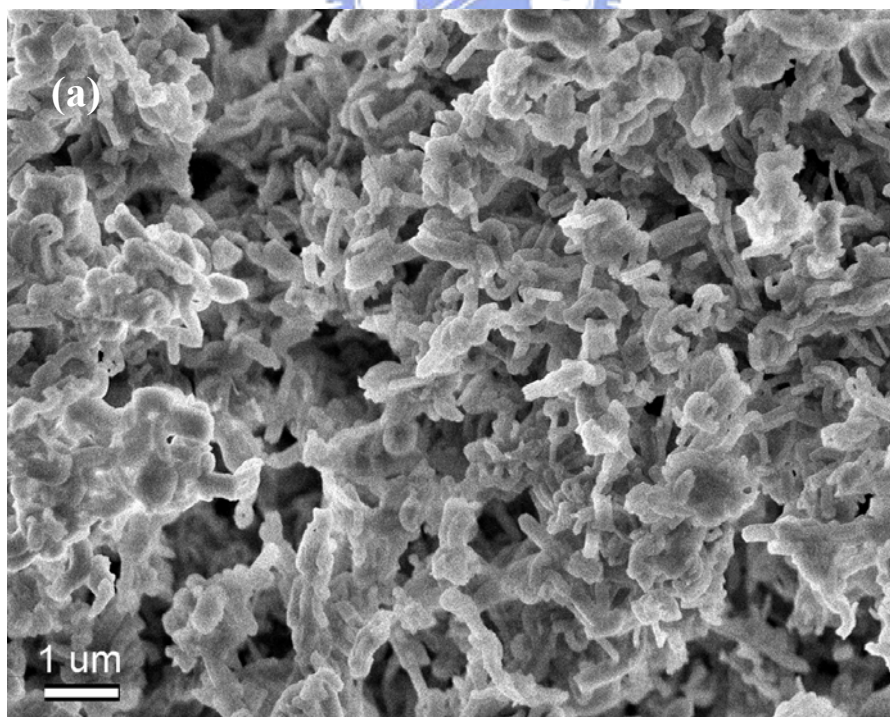


Figure 5.5 (a) Nitrogen adsorption-desorption isotherms and (b) pore-size distribution of SBA-15 synthesized at 40°C, 60°C, and 100°C.



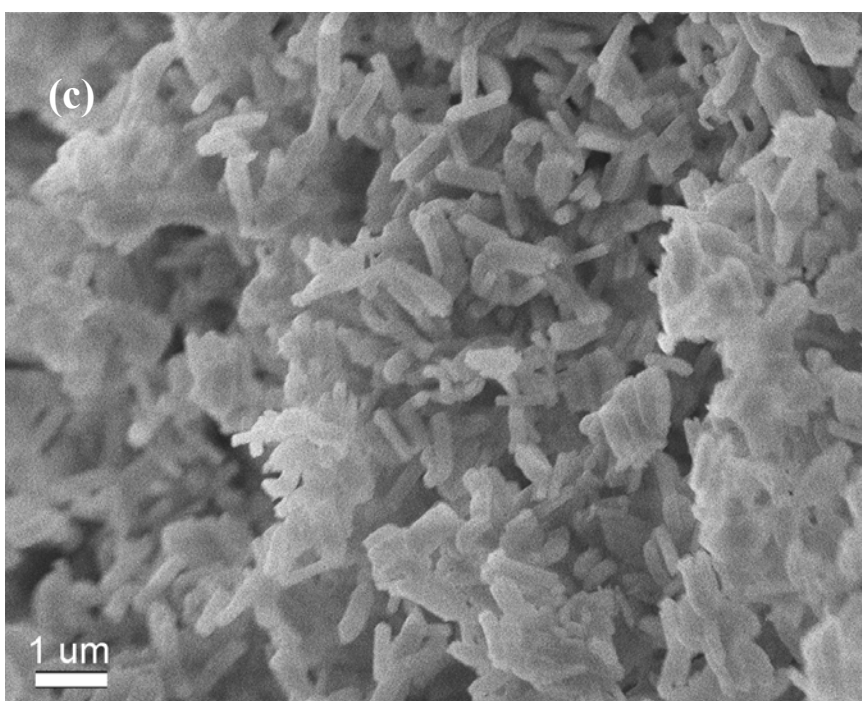
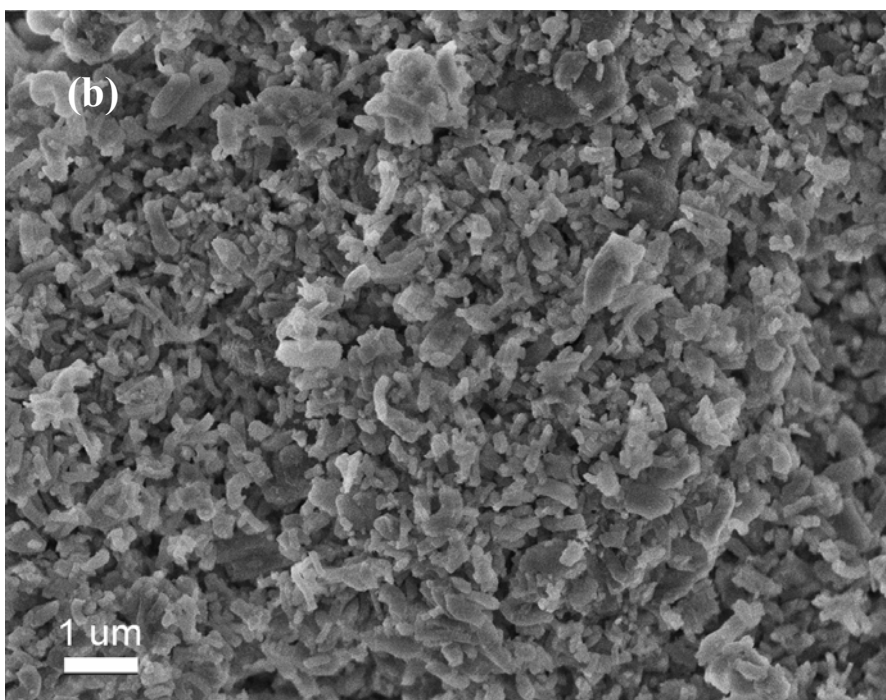
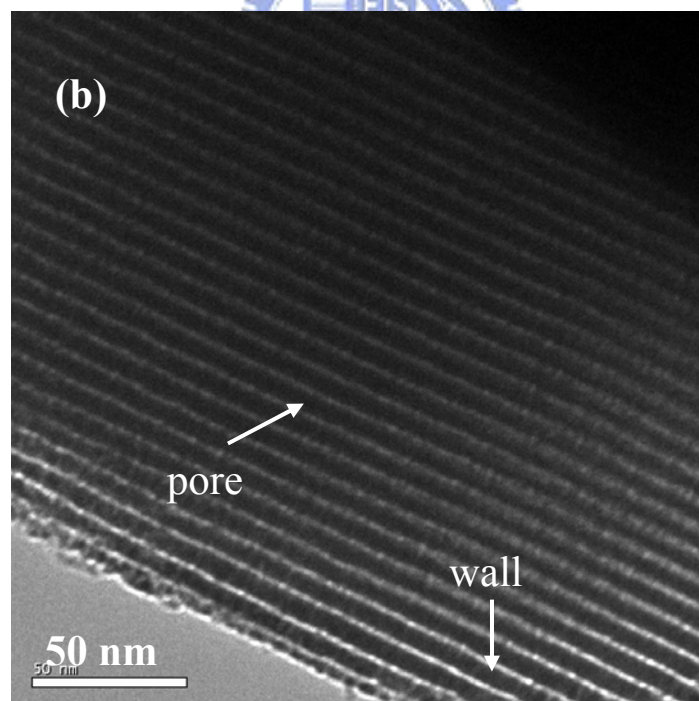
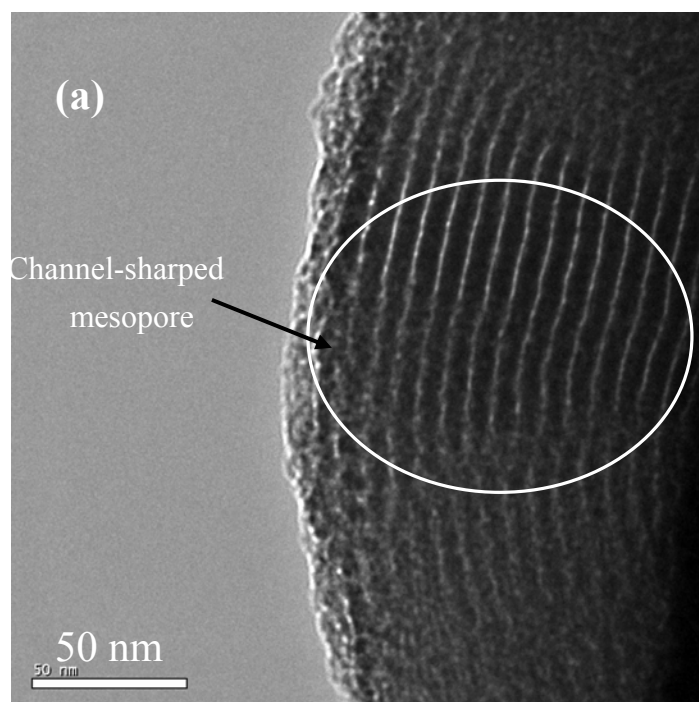


Figure 5.6 SEM images of SBA-15 synthesized at different temperatures: (a) 40°C, (b) 60°C, and (c) 100°C.

To investigate structural variations among the SBA-15 samples at different temperatures, SEM images focused on the morphological variations thereof (Figure 5.6). At a temperature of 40°C, the morphology of SBA-15 was randomly oriented. With a temperature increase to 60°C, the SBA-15 growth was prolonged becomes and became closely arranged. At a temperature of 100°C, the micelle of SBA-15 was reconstructed and a rod-like structure formed. Figure 5.7 shows TEM images of SBA-15 at different aging temperatures. As can be seen, the interconnections of pores became rigid when the aging temperature increased to 100°C. In Figure 5.7 (a), the TEM image shows that the SBA-40d possessed a partially ordered structure at the lower aging temperature, and some channel-shaped mesopores were found. In Figure 5.7(c), complete channel-like pores existed in the SBA-15 at a high aging temperature; in-between, a mixed mesophase coexisted in the SBA-15 at an aging temperature of 60°C (see Figure 5.7(b)). Therefore, the higher the aging temperature is, the more mesophase the SBA-40d is; the lower the aging temperature is, the more partially mesophase it is. These findings are consistent with the XRD patterns of SBA-15, under different aging temperatures. Moreover, it is apparent that a sample prepared at a lower aging temperature and with a poor channel mesophase presents with structure-ordering that is somewhat lower than that of material prepared at a higher aging temperature. The larger pore size and thicker silica pore wall of SBA-15 obtained at higher temperatures may have been caused by the properties of triblock copolymer templates: It is well-known that EO-PO-EO triblock copolymers, when in water, form micelles, in which the core and mantle comprise PO blocks and EO blocks, respectively. At the temperatures used in this study to synthesize SBA-15 samples (313K~373K), PO blocks are strongly hydrophobic, whereas the hydrophobicity of EO blocks strongly increases as temperatures increase. In acid solutions, hydrophilic EO moieties are expected to increase with the protonated silica through hydrogen bonding and thus be closely associated with the inorganic wall. Increasing the temperature results in an increased hydrophobicity in the EO block, and therefore decreases the lengths of the EO

segment that are associated with the silica wall. This tends to increase the hydrophobic volumes of the surfactant aggregates, resulting in increased pore sizes among the SBA-15 samples made at high temperatures. On the other hand, the SBA-15 synthesized at different temperatures allowed us to differentiate, in addition to the structural properties, the porosity, ultramicroporosity (pore size <1 nm), and second porosity with a very broad pore-size distribution, depending on synthesis temperature (i.e., between 1.5 nm and 3–5 nm) [79]. The presence of ultramicropores in SBA-15 walls can be explained by the micellar behavior of non-ionic surfactants, which has been extensively studied in the absence of silica [80]. Non-ionic micelles in water are surrounded by a corona of hydrated polyethylene oxide (PEO) chains protruding by nearly 1 nm from the average micelle surface [81]. When an isotropic micellar solution is formed, the repulsion between opposite combs of hydrated PEO chains takes the micelles to a distance of at least 3–4 nm. PEO chains pertaining to adjacent micelles do not share their hydrogen shells (Figure 5.8), but the situation changes when the temperature increases: Water becomes a less effective solvent, the PEO chains withdraw to the surface of the micelle, and a net intermicellar attraction arises from the PEO-PPO interactions between adjacent micelles. At the cloud point, the micelles interact strongly enough to form aggregates that can be separated from the diluted solution.



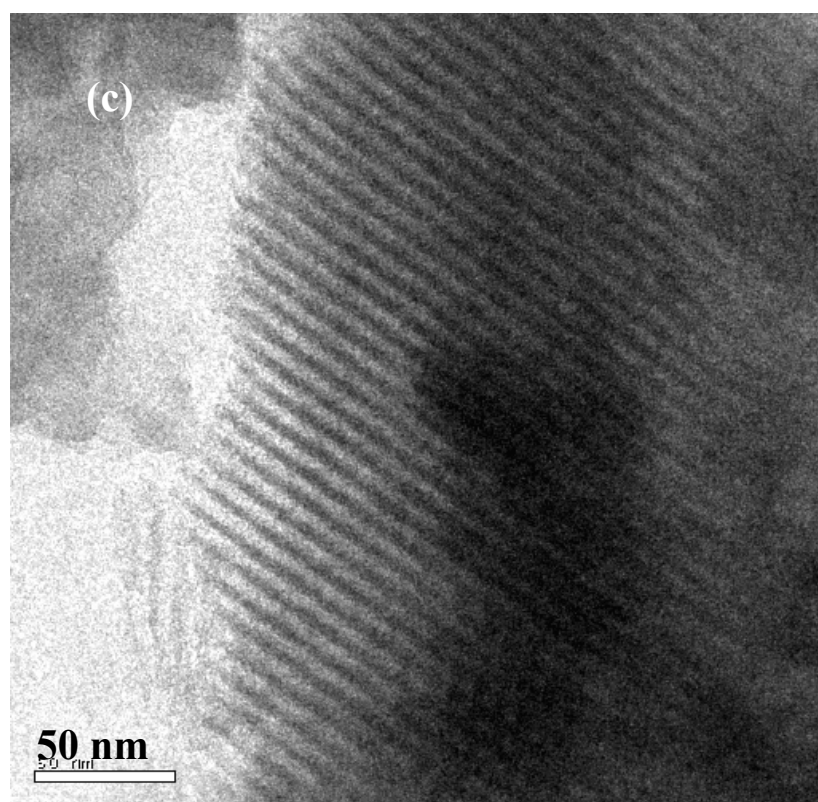


Figure 5.7 TEM micrographs of SBA-15 synthesized at different aging temperatures: (a) 40°C, (b) 60°C, and (c) 100°C.

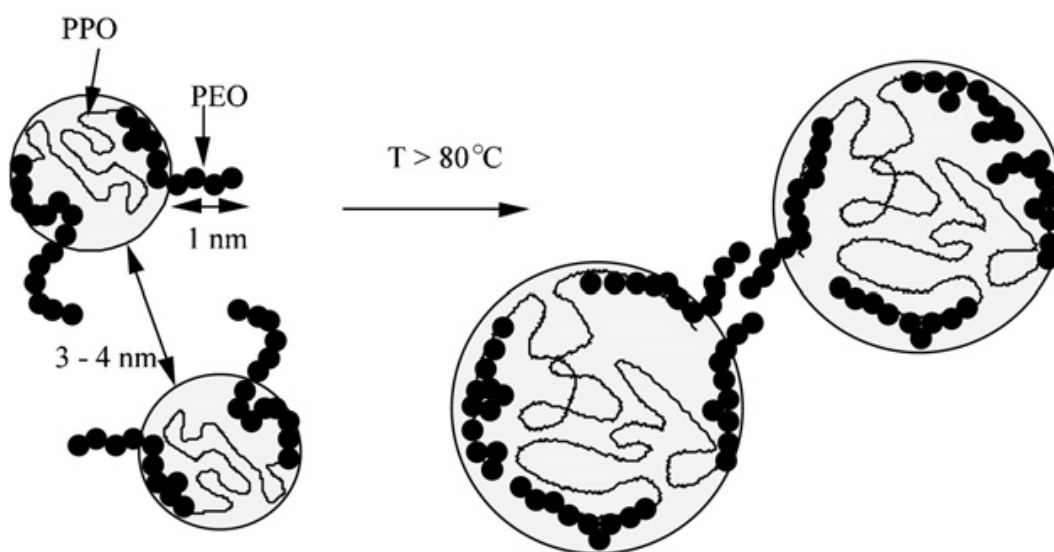


Figure 5.8 Schematic representation of micelle dehydration upon temperature increase.

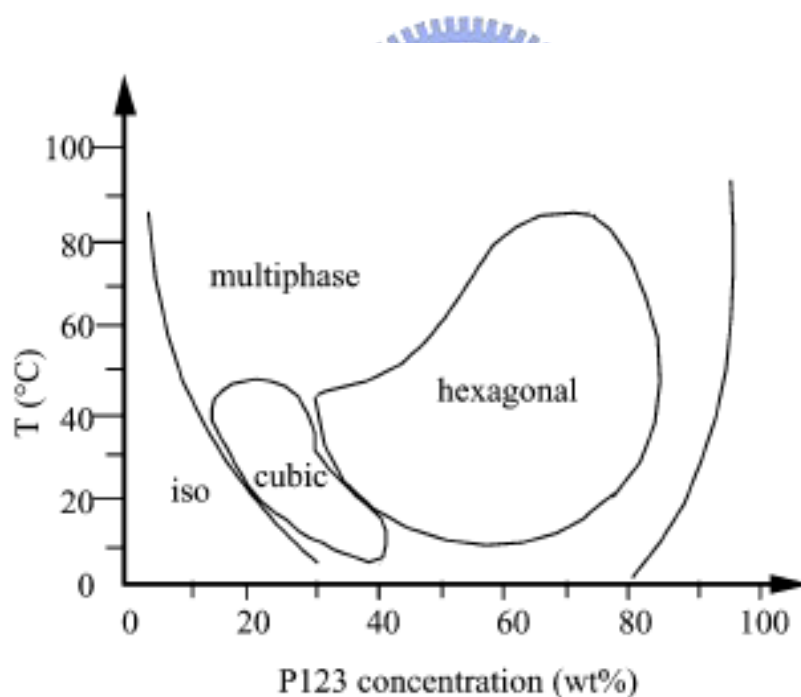


Figure 5.9 Phase diagram of P123, $\text{EO}_{20}\text{PO}_{70}\text{EO}_{20}$ [82].

The evolution of SBA-15 with synthesis temperature closely corresponds to this pattern. In all syntheses, the first step was a day-long aging at 35°C, during which the presence of silica prompted the formation of a composite mesophase at surfactant concentrations at which

only an isotropic solution is present in the absence of silica (Figure 5.9) [82]. Ordered SBA-15 materials are the result of the restructuring of this precursor mesophase formed at a low temperature; if the precursor mesophase is not allowed to form and the synthesis temperature is immediately raised, the solid that forms will be disordered, and possess both a broad pore-size distribution and hystereses indicative of restrictions at the mouths of pores. SBA-15 materials formed at the lowest temperatures are expected to fairly represent the properties of the precursor mesophase. The wall thicknesses of the materials formed at temperatures not higher than 60°C resulted in the smallest distance between hydrated micelles in water. This is strongly suggestive of a mechanism by which silica precursors impregnate the intermicellar space, in which case the observed ultramicroporosity would be templated by the protruding PEO chains. If silica walls should reproduce the topology of the hydration shells of the PEO chains in water, no microporous bridges should be expected between adjacent micelles at low temperatures.

When the precursor mesophase formed at 40°C is heated to temperatures higher than 80°C, its fine structure is not preserved; on the contrary, the size of the structural mesopores increases, the thickness of the walls decreases, the ultramicroporosity disappears, and a pore-bridging secondary porosity appears. The temperature at which these phenomena begin to take place is very close to the cloud point of the surfactant, which indicating a lower solvation of PEO chains. Interestingly, silica-embedded micelles behave similar to micelles in water, in that the disappearance of ultramicroporosity parallels the disappearance of PEO fingers. PEO chains become a less efficient template for silica, and this effect corresponds to a weaker interaction between PEO and silica. The reduced strength of the PEO-silica interaction at higher temperatures is evidenced by the increased ease with which surfactant can be extracted of surfactant; however, the weak interaction between PEO and silica destabilizes the corona of the PEO-templated ultramicroporous silica that surrounds the micelles of the precursor mesophase. A phase separation of PEO and silica takes place at the nanometer scale,

bringing about an increase in the size of the structural mesopores and a densification of the silica walls. It is interesting to note that the cell parameter of the hexagonal structure remains virtually constant upon hydrothermal treatment, just as the evolution of the precursor mesophase with increasing temperature took place via the redistribution of organic volume inside a close micrometer. The process likely takes place in a haphazard way, with the opening of local gaps in the walls at the origin of the secondary porosity, acting as a bridge between structural mesopores.

The opening of bridges between the structural mesopores of SBA-15 synthesized at temperatures greater than 80°C—and thus in the system's non-ionic surfactant-silica-water—seems to parallel the connections between micelles at the cloud point in the system's non-ionic surfactant-silica-water. Although the driving force is undoubtedly the same, the weaker interaction between the micelle and its solvent, as well as the differences between the two systems, provide information on the role of the inorganics in the formation of composite mesophases. The increase in mesopore size with temperature does not have a clear-cut equivalent in the water-surfactant system. The partial dehydration of the PEO chains could be expected to bring about a decrease in area/volume ratio among the micelles and an increase in the aggregation number of ionic surfactants.

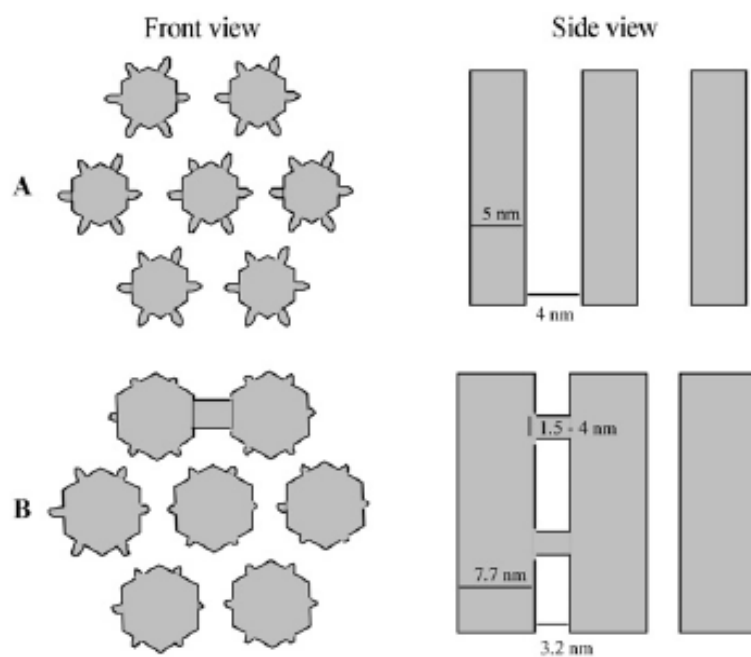


Figure 5.10 Schematic representation of SBA-15 synthesized (a) between 40 and 60°C, showing micropores and no connection between mesopores, (b) around 100°C, showing micropores and connection between mesopores [78].

5.1.2 Synthesis of SBA-15 at low acid concentrations

Structural and textural control is especially important in the design of functional porous solids—especially for applications that involve selectively tuned adsorption and diffusion—and in host-guest interactions within elaborately nanostructured materials. However, synthetically, most of these large-pore mesoporous silicas were prepared at high acid catalyst concentrations (i.e., around 1.5–2 M in water), under which the mesophase formation occurs through a kinetically controlled competitive assembly of organic and inorganic species into nanostructured domains. The fast kinetics of hydrolysis and the condensation of silica at high acid concentrations results in a rapid hybrid mesophase assembly, somehow limiting the possibilities *vis-à-vis* the true and detailed design of textural and structural properties. Co-condensation reaction kinetics are especially difficult to control in this respect. In addition, under high acid concentrations, only a narrower range of SiO₂/triblock copolymer ratio is acceptable for synthesis, otherwise, a marked decrease in ordering occurs. To overcome problems linked to quick condensation and a too-rapid mesophase assembly, we have developed an alternative synthetic strategy that is based on a combined decrease in acid catalyst concentration, to facilitate the modulation of the structural parameters of mesostructured products [83]. In this way, the formation of the mesophase can be governed more thermodynamically as the acid concentration decreases, preventing a sudden inter-micellar condensation of silica. Herein, in diluted acidic conditions, we have successfully discovered the simple principle of balancing kinetic and thermodynamic effects in materials-synthesis processes. In this respect, SBA-15 possesses some special features, all of which will be discussed here.

Using the low acid concentration method, the thermodynamic and kinetic effects are both occurred simultaneously, during silica species polymerization [84]. Under these conditions, the phase behavior of the triblock copolymer in the presence of silica

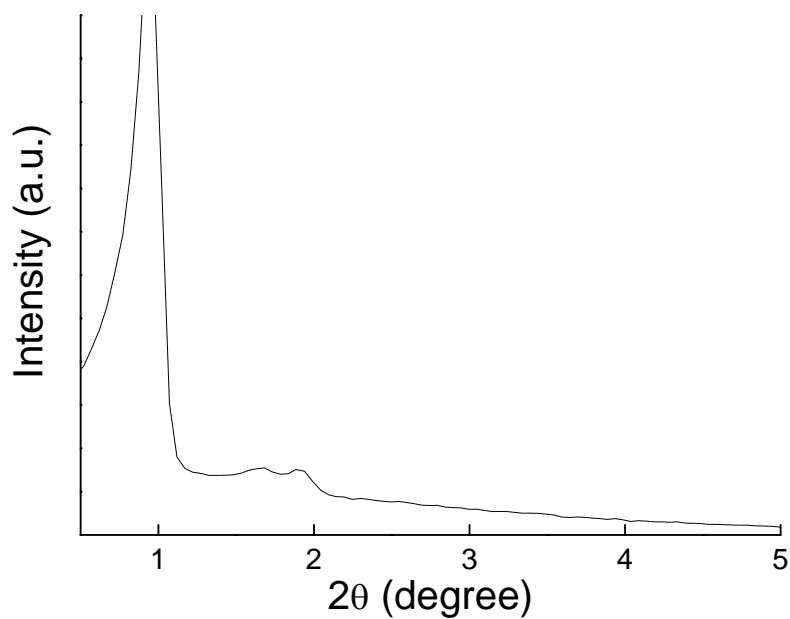


Figure 5.11 XRD patterns for mesostructured silica, synthesized under 0.001 M acid concentration.

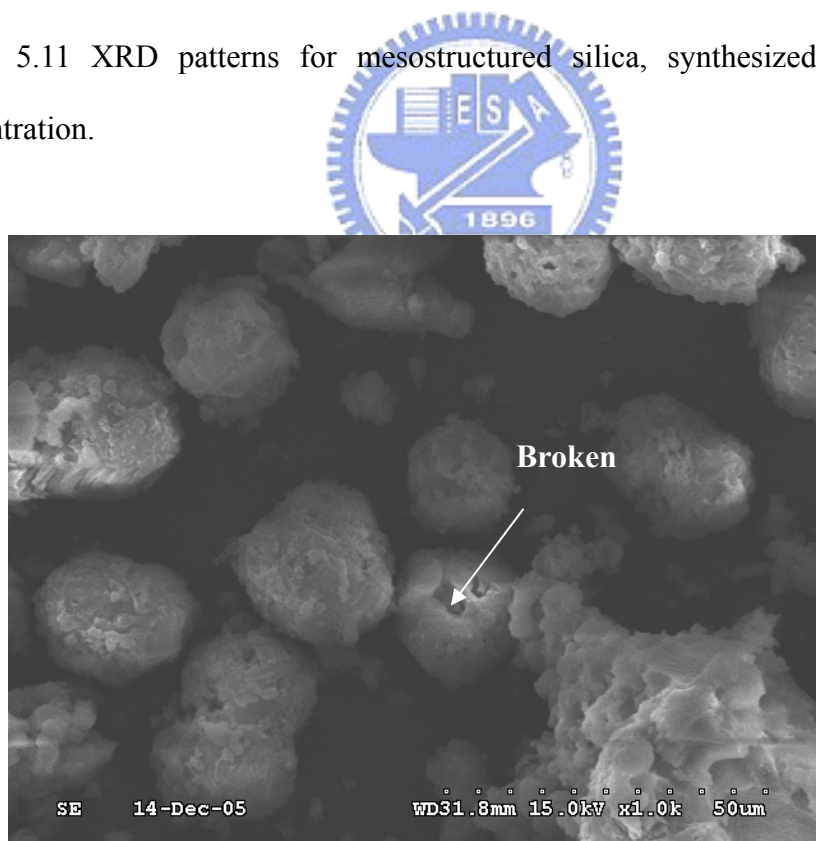


Figure 5.12 SEM image of mesostructured SBA-15, synthesized under 0.001 M acid concentration.

species can be enriched in water, since the slower silica condensation kinetics are slower. The powder XRD pattern of mesoporous silica synthesized under a 0.001 M acid concentration is depicted in Figure 5.11, illustrating the major role of acid concentration on the structure of the mesophase. The figure shows the three peaks, which can be indexed according to a hexagonal array of mesopores, that are indicative of the diffraction planes (100), (110), and (200). The unit cell size, calculated from the (100) reflection of the $p6mm$ phase, was measured to be 9.6 nm for a SBA-15 material synthesized under lower acid conditions—a value smaller than that of SBA-15 procured through high-acid synthesis. Because the condensation rate was faster than the hydrolysis rate of the silica precursor, the silica chains were branched randomly and the linear silicate formed tightly under mildly acidic conditions [85, 86]. The noises of the XRD peaks became higher as the acidic concentrations decreased. This finding is reasonable, because the presence of OH^- causes hydrolysis in preformed SBA-15 samples. SBA-15 is synthesized under strongly acidic conditions by the $\text{S}^0(\text{H}^+)\text{X}^+\text{T}^+$ route, and its frameworks are electrically neutral: $(\text{S}^0\text{H}^+\text{X}^-\text{T}^0)$ [87], where S^0 is a non-ionic surfactant, T^+ is a protonated silanol group, and X^- is the counteranion. These mesoporous silica samples—such as MCM-41—are synthesized under mild conditions, via the S^+T^- route; however, they have negatively charged frameworks. Both products exhibited an enlargement and broadening of the (100) reflections, along with poorly resolved higher-angle peaks, while the acidic concentration decreased. Figure 5.12 shows an SEM image of SBA-15 synthesized under 0.001 M HCl conditions. It was found that the SBA-15 particles were spheroidal. Glassy material is generally present when acidity is very low, and it acts like a cement between particles. The results can be rationalized if a synthesis mechanism is considered, which takes into account the polycondensation rate of the silica species [88] and the dynamic of the micelles [89]. The increased in the condensation rate with acidity affected the nucleation and formation rate of the particles. Under mildly acidic conditions, the reactions possessed a rapid depletion reaction in the solution and the nucleation was active for only a short time. Under

strongly acidic conditions, however, the interactions between silica and surfactant were weak, owing to the greater hydration of the acid through the formation of hydrogen bonds. The formation of the mesoporous silica was derived into two steps. During the first step, the surfactant micelles more or less controlled the polycondensation of the acidity, in turn raising, the discreteness of the particles. In the second step, the weakened and less-organized material from the first step were embedded. We assume the period of time needed to build a given length of silica wall around the micelle in mild acidic conditions. Nevertheless, the ratio of the lifetime of the micelle to the growth time of the wall becomes much higher than unity, under strongly acidic conditions. In such cases, three paths can be considered. (1) In strongly acidic conditions, the lifetime is too short compared to the time needed to construct the silica wall, and sharp, fiber-like sharp materials are presented. (2) In medium acidic conditions, there is a shortening of the micelle lifetime and an increase in the structural disorder, and numerous sharp, rod-like materials are presented. (3) In mildly acidic conditions, the lifetime of the micelles is very long, compared to the time needed for the formation of the solid, and spheroidal and polyhedral particles are presented. Nitrogen adsorption isotherms for SBA-15 samples are shown in Figure 5.13. The two step desorption isotherm appeared under mildly acidic conditions (i.e., 0.001 M). The nitrogen adsorption-desorption isotherm possesses some special features, namely, “plugged mesopores.” The formation mechanism is discussed below.

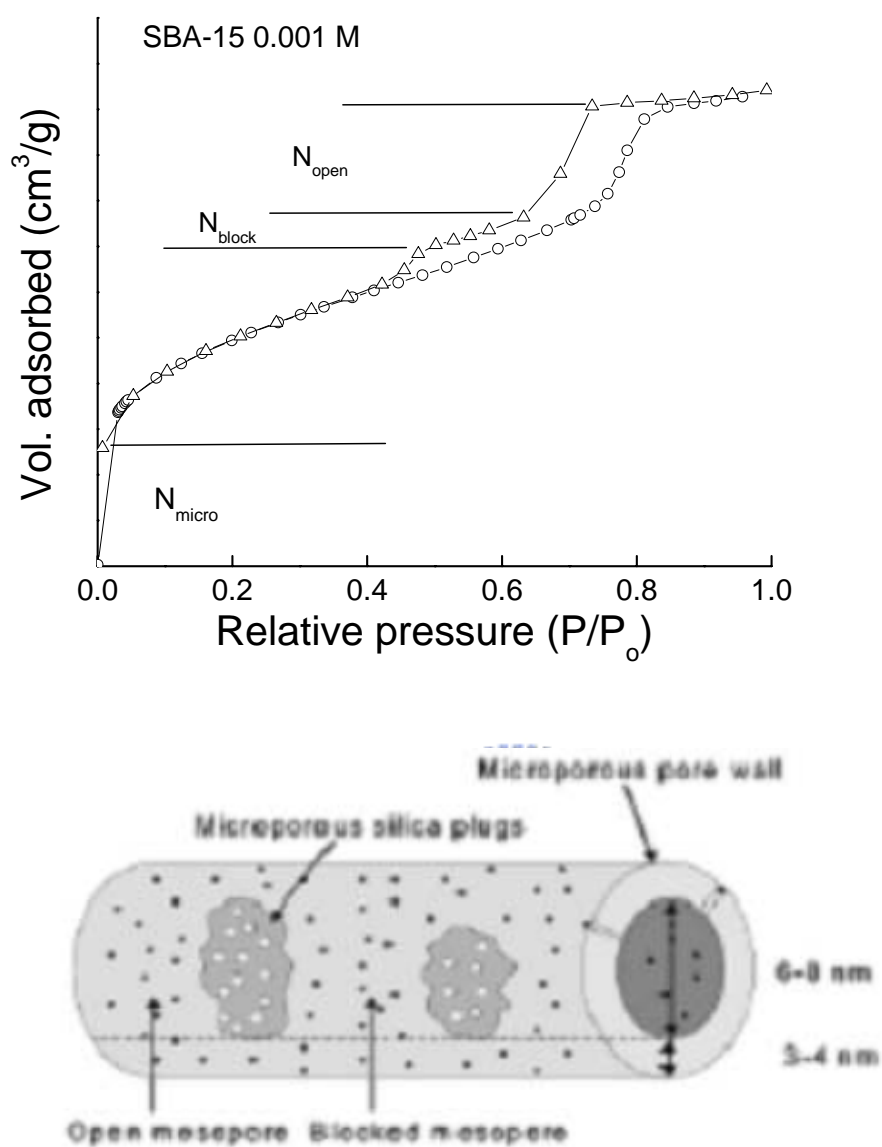


Figure 5.13 Nitrogen adsorption-desorption isotherms of “plugged” mesopores, comprising both open and blocked mesopores, intrawall micropores, and microporous silica nanocapsules [90].

5.1.3 Two-step desorption isotherm of SBA-15

In general, gas adsorption is especially suitable for the characterization of internal porosity and pore size distribution. In the case of hysteretic adsorption, the following features are evident: (1) on the adsorption branch, as the relative pressure increases, the isotherms exhibit a sharp step indicating capillary condensation; (2) on the desorption branch, as the relative pressure decreases, the desorption step is located at a relative pressure that is much lower than that which capillary condensation requires. The adsorption branch corresponds to the theoretical isotherm of the metastable states, which is terminated by spontaneous condensation near the vapor-like spinodal. The desorption step corresponds to spontaneous evaporation from necks/windows, or at a pressure limited by the equilibrium transition pressure and the liquid-like spinodal pressure. In other words, desorption from large cavities is determined by the size of the windows that connect the cavity with the bulk fluid. If the size of the window is smaller than a certain critical size (~ 4 nm for nitrogen at 77K) or the equilibrium evaporation pressure from the pore window is lower than a certain critical relative pressure, the confined fluid attains its limit of stability. At this point, spontaneous desorption occurs via cavitation. Lately, a new type of templated porous material combining microstructures, mesoporosity, and a tunable amount of both open and plugged mesopores has been developed by van der Voort et al. [90]; it possesses a step-like hysteresis in a nitrogen adsorption-desorption isotherm (Figure 5.13). It has been said that a two-step desorption branch indicates the pore-blocking effects. They also report on the development of a plugged hexagonal silica template containing both open and encapsulated mesopores. The two-step desorption isotherm results from the fact that encapsulated mesopores empty at lower pressures than open pores of similar pore size. This can be explained by the fact that several EO chains are withdrawn from the micelle. A decrease in acidity is likely to reduce the hydrophilicity of the PO segments; consequently, the curvature of the copolymer aggregates may decrease, allowing the hydrophobic core that determines the framework pore size to

increase.

5.2 Mesostructured cobalt oxide materials

Ordered mesoporous materials were first discovered in the early 1900s by Mobil scientists [91, 92]. The simple soft templating method by using organic surfactants that form micelles in aqueous solutions allows for a wide range of mesoporous materials to be synthesized. Over the past 14 years, many reports have been published on new phases of mesoporous materials. Mesoporous metal oxides are of wide interest for catalytic applications, since they can be regarded as self-supported catalysts with large specific surface areas and sharp selective properties. Cobalt oxide nanostructures employing SBA-15 as a hard template have been created, and the influence of the framework connectivity of the parent silica, the loading of the cobalt source, and the gas-sensing performance is studied in detail.

The specimen of $\text{Co}(\text{NO}_3)_3 \cdot 9\text{H}_2\text{O}$ -loaded SBA-15 specimen had a pink color, which is characteristic of Co^{2+} cations. Generally, by using the hard template replication method for mesostructured materials, a precursor of cobalt nitrate is impregnated in silica templates through calcination. To understand the decomposition of the cobalt nitrate inside the silica template, thermal decomposition analyses were performed. Figure 5.14 shows a decomposition plot of the cobalt-silica composites; this figure shows that four inflection points were obtained. These points indicate a loss of excess water, which was released at a temperature of 80°C. Further, evidence of the release of two pairs of water molecules that corresponded to the cobalt nitrate was detected at temperatures of 120°C and 180°C. Finally, the nitrate decomposition was completed and cobalt oxide was formed at a temperature of 210°C. The formation temperature for the cobalt oxide was relatively low, with cobalt oxide appearing at 250°C.

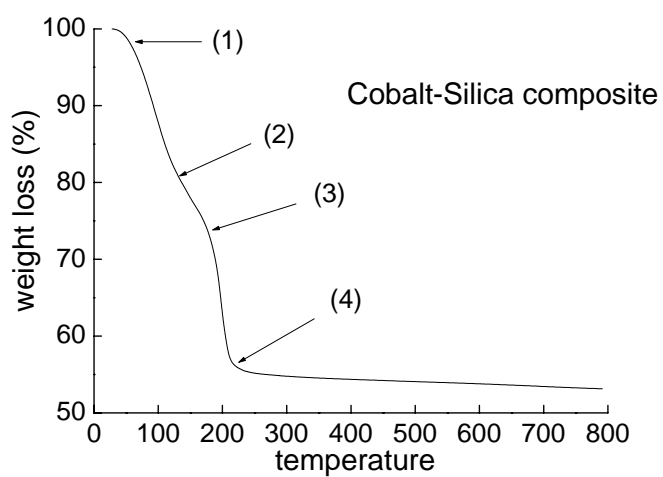
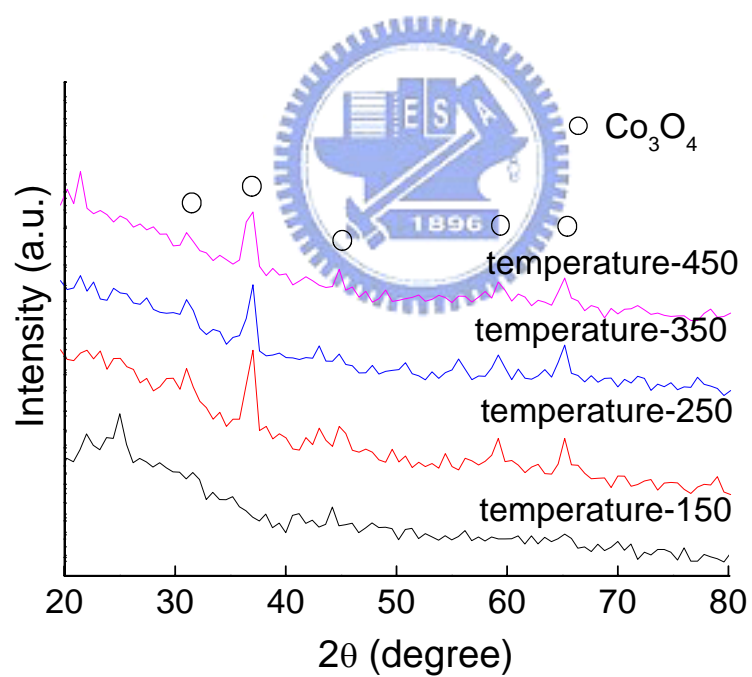


Figure 5.14 Thermal decompositions plot of the cobalt-silica composite.



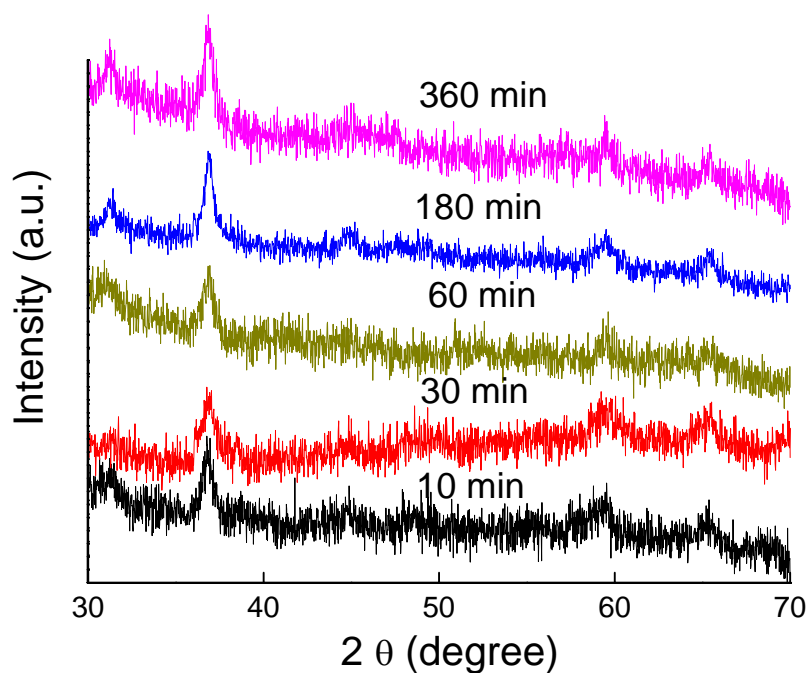


Figure 5.15 (a) XRD patterns of samples with cobalt oxide in SBA-15, at different aging temperatures, and (b) XRD patterns of cobalt oxide heated at 250°C for various lengths of time.

The XRD patterns of cobalt oxide in SBA-15 at different aging temperature were shown in Figure 5.15. Some unknown phase appeared at the temperature of 150°C, whereas the cobalt oxide crystalline phases were obtained at temperatures above 250°C. The peaks are located at 31.3°, 36.8°, 44.8°, 59.4°, and 65.2°. The XRD patterns can be indexed using a face-centered cubic unit cell of the cobalt oxide space group $Fd3m$ (JCPDS 742120). No impurity phases were detected. To investigate the formation conditions of mesostructured cobalt oxide materials, the XRD patterns of mesostructured cobalt oxide materials were heated at temperatures of 250°C for different periods of time. After the 10-min thermal treatment, the XRD showed that only phase cobalt oxide could be detected. The cobalt oxide has a preferred orientation of (311) phase, which is consistent with commercial cobalt oxide materials [93]. The peak of cobalt oxide orientation becomes sharp, which is indicative of an

increase in crystallinity among the cobalt oxide materials. Using the Scherrer equation, the average crystal size of the mesostructured cobalt oxide was calculated to be 15 nm. Furthermore, the oriented peak of the mesostructured cobalt oxide shifted to the low XRD angle, indicating that the grain size grew after the mesostructured cobalt oxide was heated at 250°C for various lengths of time.. Consequently, a combination of thermal and XRD results indicate that the crystallization of $\text{Co}(\text{NO}_3)_2 \cdot 2\text{H}_2\text{O}$ occurs first by the loss of four water molecules per $\text{Co}(\text{NO}_3)_2 \cdot 6\text{H}_2\text{O}$, followed by a phase transition to $\text{CoNO}_3(\text{OH}) \cdot \text{H}_2\text{O}$ by losing one NO_3^- anion; additionally, all water molecules were lost. The 2^+ oxidation state of Co remained unchanged except in the final stage where it was partially oxidized into 3^+ .

A comparison was made of the decomposition of cobalt nitrate hexahydrate, with and without the presence of the mesoporous silica template. Figure 5.16 shows the formation of mesostructured cobalt oxide materials. It was found that the non-templated specimen at 150°C formed the tetrahydrate state, $\text{Co}(\text{NO}_3)_2 \cdot 4\text{H}_2\text{O}$, and cobalt hydroxide nitrate monohydrate. By increasing the temperature to 250°C, cobalt nitrate started to break down into cobalt oxide. In that figure, some peaks of cobalt oxide could be obtained.

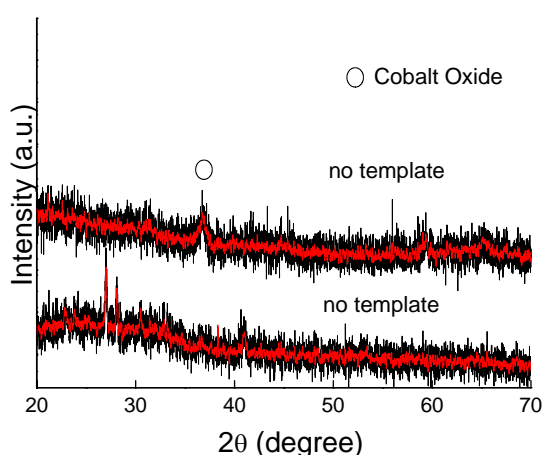
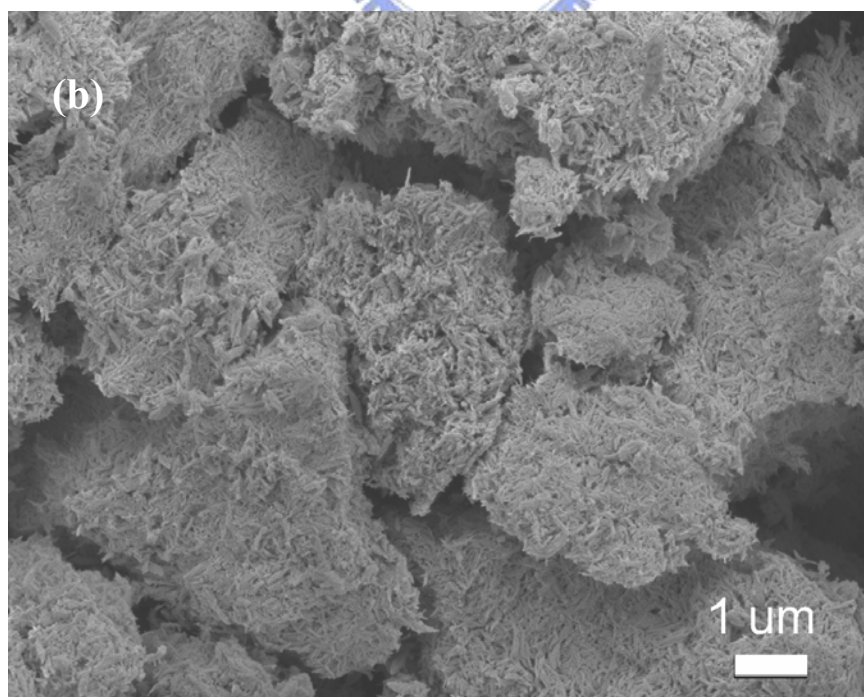
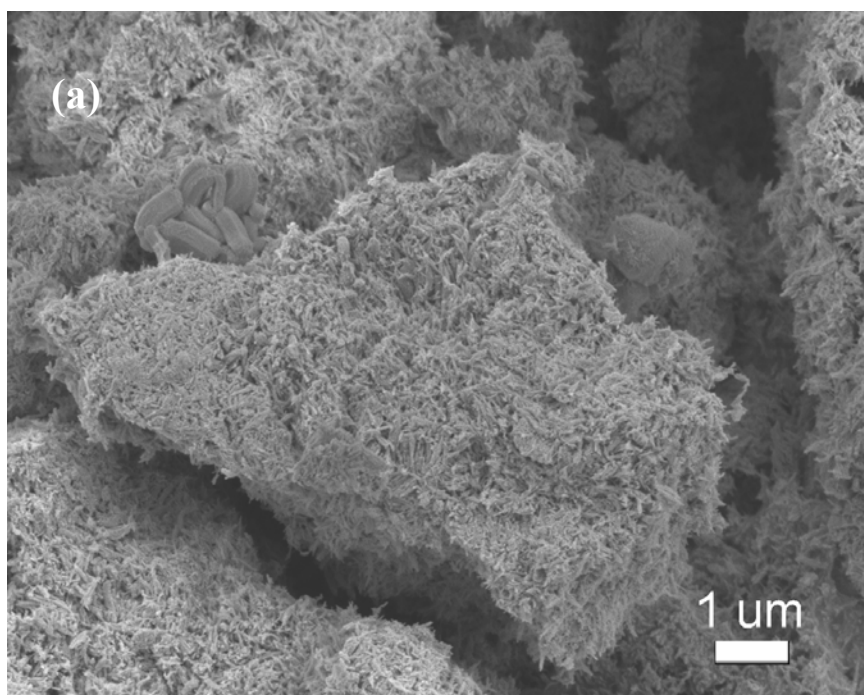
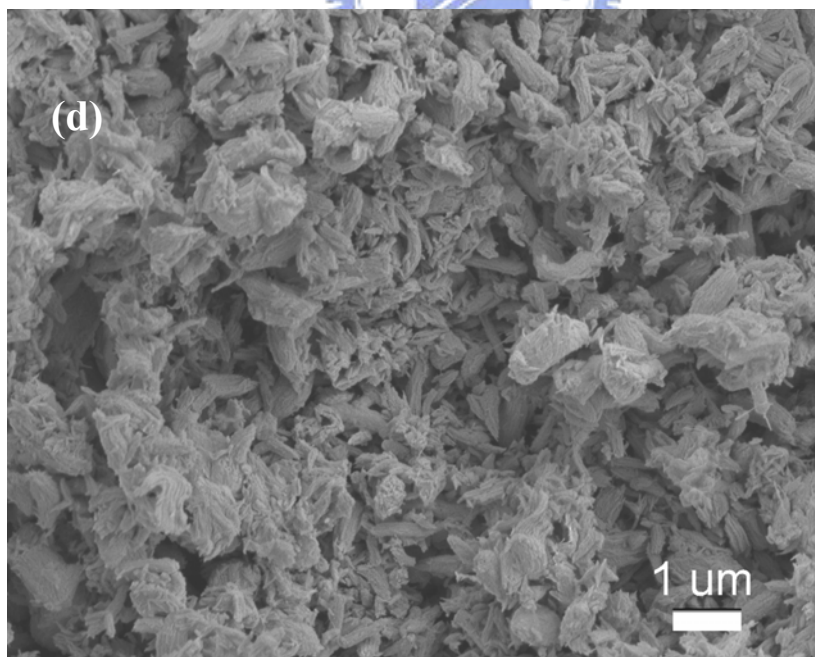
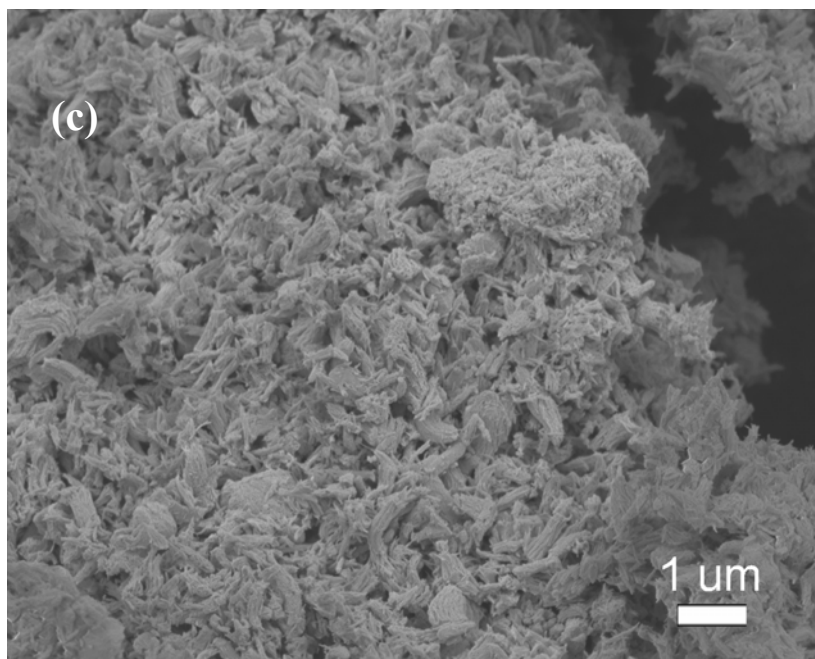
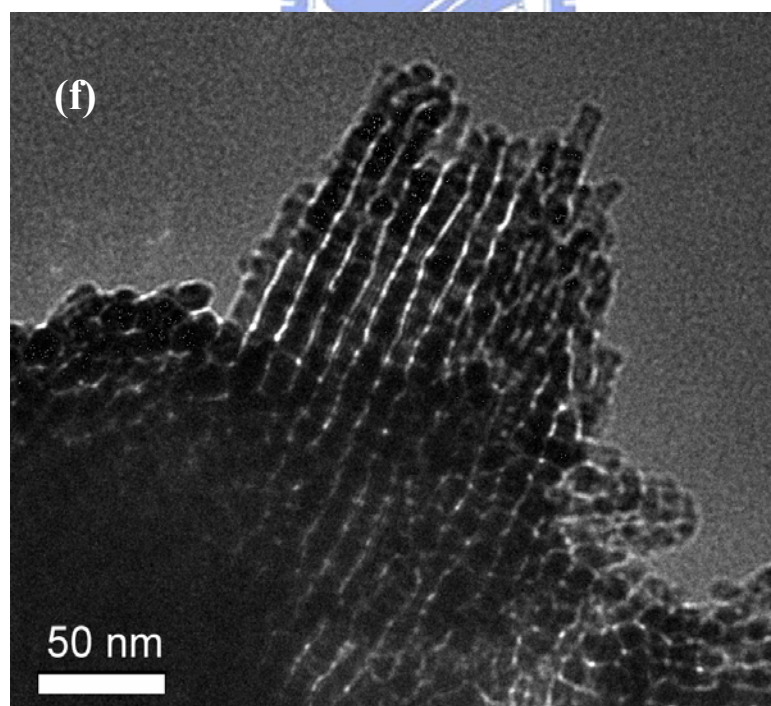
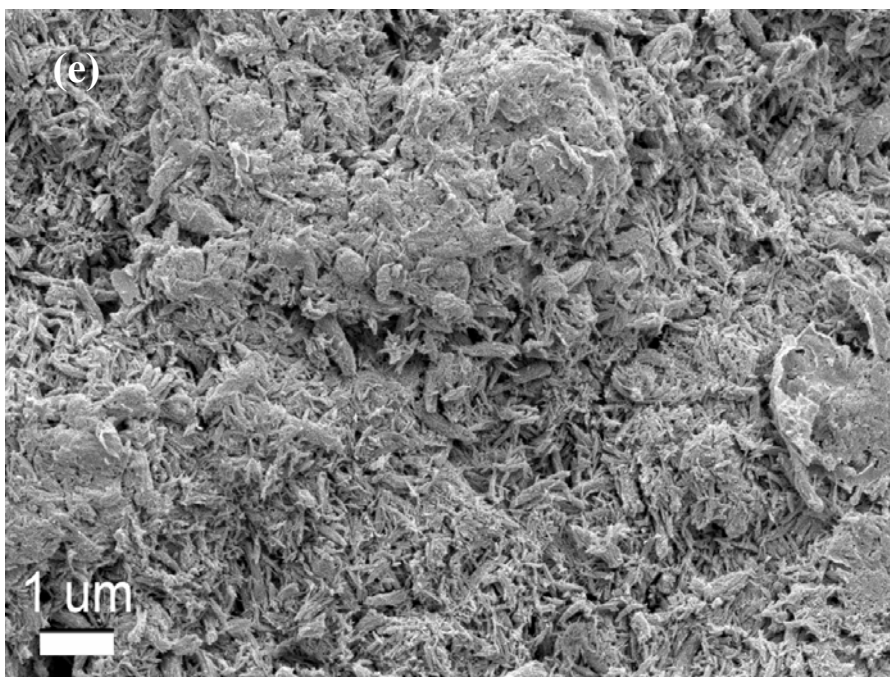


Figure 5.16 XRD patterns of the specimens after decomposing $\text{Co}(\text{NO}_3)_2 \cdot 6\text{H}_2\text{O}$, without the presence of silica template.

It should be noted that the formation of $\text{CoNO}_3(\text{OH}) \cdot \text{H}_2\text{O}$ is not commonly observed; the formation of $\text{CoNO}_3(\text{OH}) \cdot \text{H}_2\text{O}$ only occurs on the outer crust of the decomposing nitrate; even so it is extremely low in yield, as it is only a partial decomposing step, as reported by Petrov et al. [94]. That study indicates that crystal characterization of cobalt oxide cannot be observed successfully, because the yield is too low; an increase in surface area of the cobalt nitrate, via the mesopores, allows for a higher yield. That higher yield, in turn, contributes to the appearance of strong XRD peaks from not only $\text{CoNO}_3(\text{OH}) \cdot \text{H}_2\text{O}$, but also from $\text{Co}(\text{NO}_3)_2 \cdot 2\text{H}_2\text{O}$. Detailed investigations of the microstructures of the mesostructured cobalt oxide materials were performed using SEM and TEM. Figures 5.17 (a) –(e) show SEM micrographs of the mesostructured cobalt oxide materials, heated at 250°C for 10 min, 30 min, 60 min, 180 min, and 360 min, respectively. It was found that, after heating at 250°C for only 10 min (see Figure 5.17(a)), mesostructured cobalt oxide materials started to grow; after being heated for 30 min, mesostructured cobalt oxide materials were split into small pieces. The mesostructured cobalt oxide materials were split continuously and reconstructed after being heated for 60 min. Moreover, the mesostructured cobalt oxide materials aggregated and formed into filiform clusters after the specimens were heated for more than 180 min. After removing the silica template, the mesostructured cobalt oxide featured a group of straight nanostructures, and their particle size was about 150 nm (see Figure 5.17(f)). On the other hand, Figure 5.17(f) indicates that the original mesopore system in SBA-15 had been replicated. The image-contrast patterns on the (100) projection of the SBA-15-related unit cell show nanochannels along the view directions, implying that only one of the channels of the SBA-15 had been replicated. The high-resolution TEM (HR-TEM) images (Figure 5.17(g)) reveal fringe images and clearly indicate the single-crystalline nature. The lattice-measured lattice spacing is 2.01 Å, corresponding to the interlayer spacing of the (400) plane of cobalt oxide. All the diffraction spots in the SAED pattern can be indexed with the spinodal cubic cobalt oxide phase.







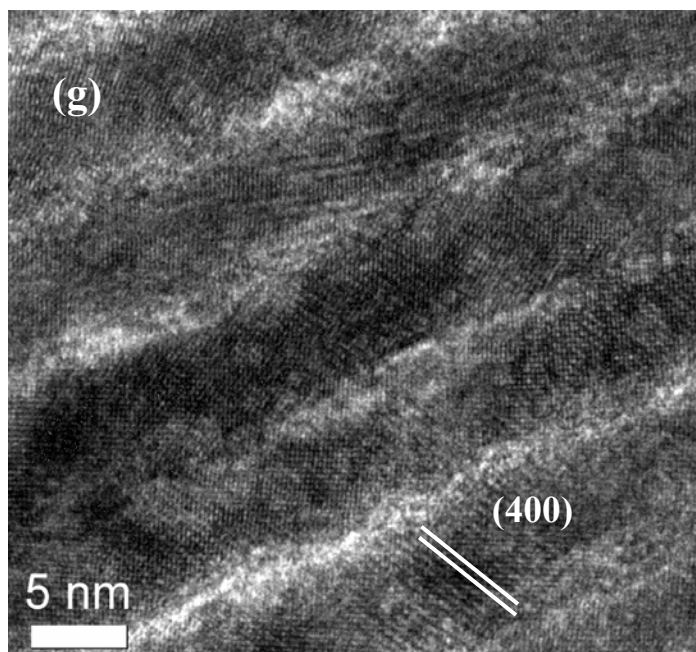


Figure 5.17 SEM images of mesostructured Co_3O_4 materials heated at 250°C for various lengths of time: (a) 10 min, (b) 30 min, (c) 60 min, (d) 180 min, and (e) 360 min. Typical bright-field TEM image of the mesostructured Co_3O_4 materials in (f); inset is the corresponding selected areas electron diffraction. (g) shows a corresponding HRTEM image of (f).

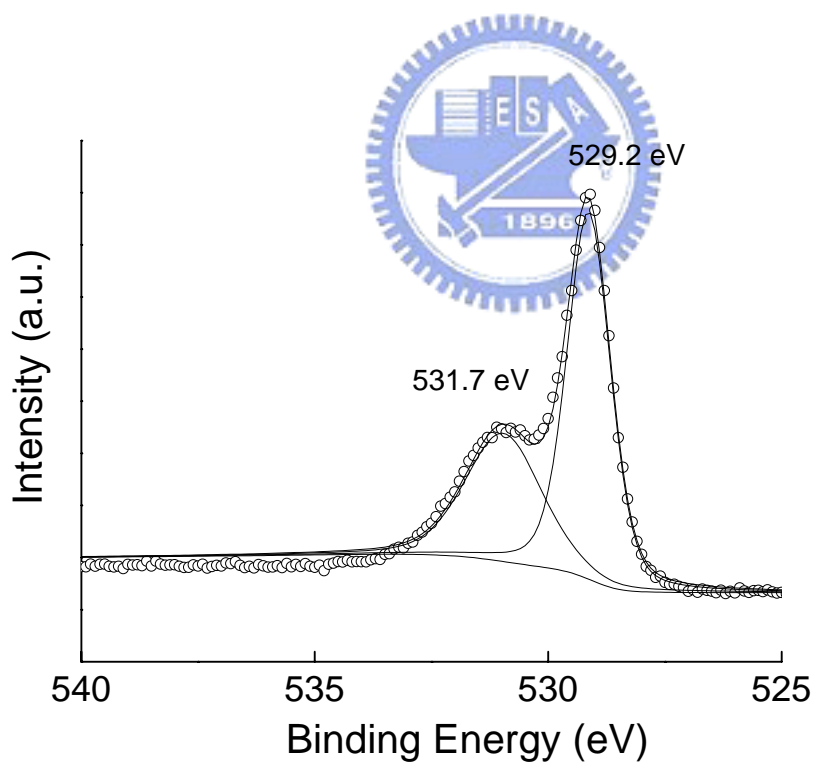
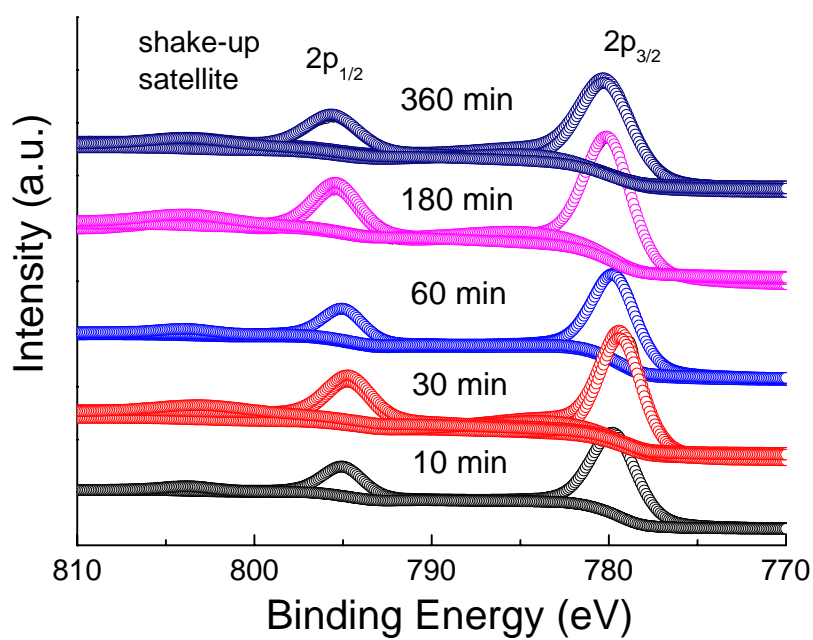


Figure 5.18 XPS measurement for (a) Co_{2p} and (b) O_{1s} core levels for mesostructured cobalt oxide materials.

To further elucidate the surface chemical composition of the mesostructured cobalt oxide materials, XPS measurements were carried out. Figure 5.18(a) shows the Co_{2p} spectra of mesostructured cobalt oxide materials. The Co_{2p} spectra consist of two main $2p_{1/2}$ and $2p_{3/2}$ at 796.3 eV and 781.3 eV, respectively, separated by about 15 eV; this was expected, following a review of the literature [96]. Furthermore, two satellites located approximately 6 eV above the primary binding energy peaks were detected. Figure 5.18(b) shows the O_{1s} XPS spectra peak with a binding energy of approximately 529.2 eV, which corresponds to an oxygen species in the spinodal cobalt oxide phase [97]. The peak observed close to 532 eV in the O_{1s} spectra indicates the presence of a-OH (hydroxyl) species adsorbed on the surface, due to the *ex situ* experimental conditions. The Co_{2p} XPS spectra show two major peaks with binding energy at 796.3 eV and 781.3 eV, corresponding to the $\text{Co}2p_{1/2}$ and $\text{Co}2p_{3/2}$ spin-orbit peaks, respectively, of the cobalt oxide phase [98, 99]. The lack of prominent shake-up satellite peaks in Co_{2p} spectra further suggests the presence of what is mainly a cobalt oxide phase [100]. Thus, from the binding energy measurements for the O_{1s} and Co_{2p} core levels and the spectral sharpness of the XPS spectra, it is clear that the formed nanostructures comprise cobalt oxide. It is interesting that the Co_{2p} spectra of mesostructured cobalt oxide materials shifted to a high binding energy when cobalt oxide was heated at 250°C for various lengths of time. The peaks shifted to high binding energy, revealing that the crystallite of the mesostructured cobalt oxide materials would be strong. The result is consistent with XRD results. To analyze the textural properties of the mesostructured cobalt oxide, nitrogen adsorption-desorption isotherms are shown in Figure 5.19. The nitrogen adsorption-desorption isotherms demonstrate that the mesostructured cobalt oxide materials show a typical type-IV isotherm with an H1 hysteresis loop. It is evident that this type of hysteresis is similar to that of well-ordered mesoporous carbon [101]. There is a sharp capillary condensation with relative pressures of 0.5 to 0.95, indicating that the degree of ordering was similar to that witnessed in the TEM observation. Moreover, the specific surface areas, total pore volume,

and pore size of the mesostructured cobalt oxide materials were $145.1 \text{ m}^2 \text{ g}^{-1}$, $0.30 \text{ cm}^3 \text{ g}^{-1}$, and 5.5 nm , respectively. The pore size of the mesostructured cobalt oxide was consistent with those in TEM observations.

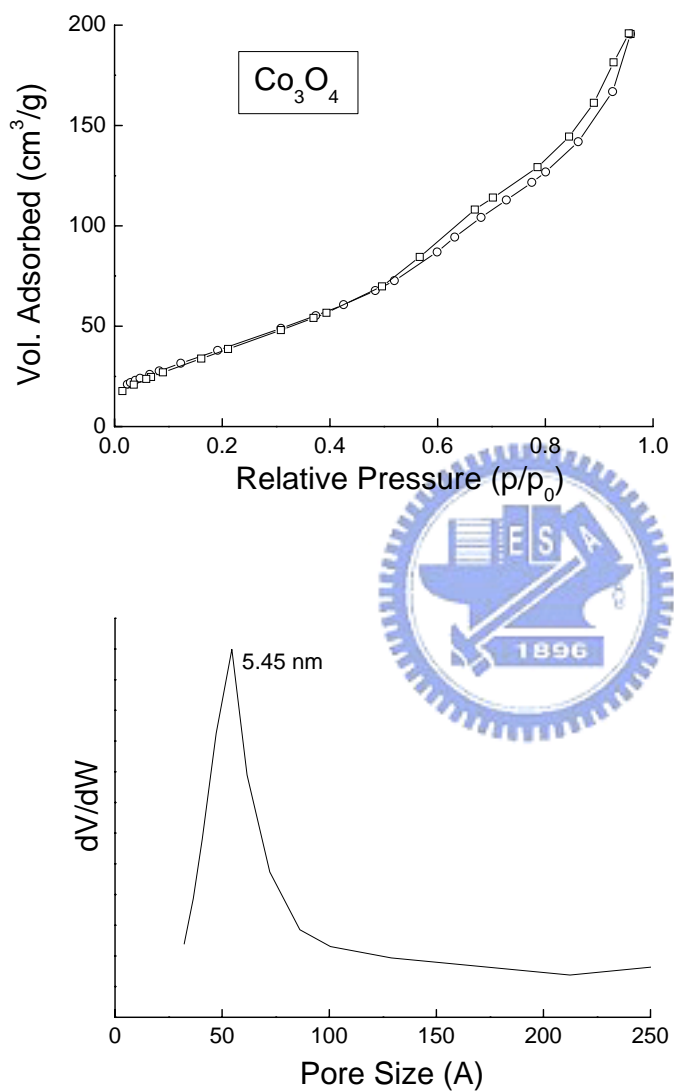


Figure 5.19 (a) Nitrogen adsorption-desorption isotherms measured at 77 K and (b) corresponding pore-size distributions of the mesostructured cobalt oxide materials.

Because capillary force is the driving force behind the insertion of guest species into the voids of a support during grinding, it is possible to obtain composites with one or more monolayers coated on the surface of the host. Moreover, a complete filling of the voids could also be achieved. When the nitrate precursor was physically mixed with the SBA-15 template containing an open structure, the nitrate could almost completely fill the pores. In all cases, pores approximately 10 nm in diameter, in the cobalt oxide materials, can be observed. It was also found that aggregate bundles and an unapparent pore system of mesostructured cobalt oxide materials were obtained in the high-loading specimen. The specimens forming the arrays were separated by a constant repeat distance, corresponding to the wall thickness of the SBA-15 templates. However, in Figure 5.20(a), the uniform pore size does not seem to be present. According to the TEM observation, the loading of the precursor strongly influences interconnectivity of mesostructured cobalt oxide materials. The structure can be tuned from randomly orientated to highly ordered, and fully interconnected networks can possess the same symmetry as the silica template.

Figure 5.21 reveals the XRD diffraction patterns of mesostructured cobalt oxide materials prepared with the templates prepared from different temperatures. As shown in Fig. 5.21, the mesostructured cobalt oxide replica samples remain the (100) reflections at crystallization temperature of 100°C. The replication for cobalt oxide was almost the same as those for the SBA-15 template, suggesting that cobalt oxide replicated the mesostructure of SBA-15. At lower crystallization temperature, the reflection of SBA-15 totally disappeared. The loss of reflections in the low-angle region should not be attributed to the dilution of the guest species but to the complete filling of pores, which decreases the contrast between the walls and the pores. At high crystallization temperature, the reflection was preserved, though their intensity was reduced due to the dilution of the amorphous gel. In fact, the mesostructure of SBA-15 is well retained during synthesizing, because the reflection of SBA-15 in the pattern almost completely recover after the $\text{Co}(\text{NO}_3)_2/\text{SBA-15}$ composites are washed with

water and dried. Thus, the complete filling of the mesopores in SBA-15 with the guest species can be used to screen the reflection of ordered mesoporous materials, as was found in several other cases such as bromoform-loaded B-MCM-41 and rare earth oxide loaded MCM-41 [103].

In general, the pore diameters of templates have been tuned by changing the temperature of hydrothermal treatment after the synthesis of the mesoporous silica. The TEM images of mesostructured cobalt oxide materials prepared from SBA-15 of different pore diameters are shown in Figure 5.21. As can be seen, it is possible to cast the mesopore structure from different SBA-15 silicas, resulting in cobalt oxide materials of different diameters. Moreover, Preparing using cobalt oxide allows to image differences in network interconnectivity. Nevertheless, cobalt oxide preparation from low crystallization temperature of 40°C does not contain ordered domains, whereas the sample preparation from high crystallization temperature of 100°C predominantly features well-ordered 2D hexagonally ordered domains with cobalt oxide arrays of reaching several nanometers in length.

The crystallization temperature of 60°C represents an intermediate situation. Arrays of mesostructured cobalt oxide materials may arise from the bridge between the mesopores in SBA-15, as demonstrated in the cases of mesoporous carbon, noble metals, and other metal oxide nanowires [104]. According to the TEM images, the diameter of the mesostructured cobalt oxide materials was close to the mesopore diameter is 7.0 nm for all samples. Nitrogen adsorption-desorption isotherms supports the results from TEM, because only for sample at higher crystallization temperature was a pronounced hysteresis observed, characteristic of the mesoporus ordered domains (Fig. 5.22). The pore size of 5.4 nm for the mesostructured cobalt oxide arrays at crystallization temperature of 100°C, as N₂ adsorption-desorption isotherm showed, was larger than the thickness of the silica walls of the sample at crystallization temperature of 40°C, 2.3 nm. These data proved the distinct volume shrinkage of the cobalt species during calcinations, as the density of cobalt oxide (6.07 g·cm⁻³) is much higher than

that of $\text{Co}(\text{NO}_3)_2 \cdot 6\text{H}_2\text{O}$ ($1.88 \text{ g}\cdot\text{cm}^{-3}$). The surface area and pore volume of the mesostructured cobalt oxide at 100°C were $175.4 \text{ m}^2\cdot\text{g}^{-1}$ and $0.37 \text{ cm}^3\cdot\text{g}^{-1}$, $150.3 \text{ m}^2\cdot\text{g}^{-1}$ and $0.30 \text{ cm}^3\cdot\text{g}^{-1}$ at 60°C , and $122.3 \text{ m}^2\cdot\text{g}^{-1}$ and $0.22 \text{ cm}^3\cdot\text{g}^{-1}$ at 40°C , respectively.

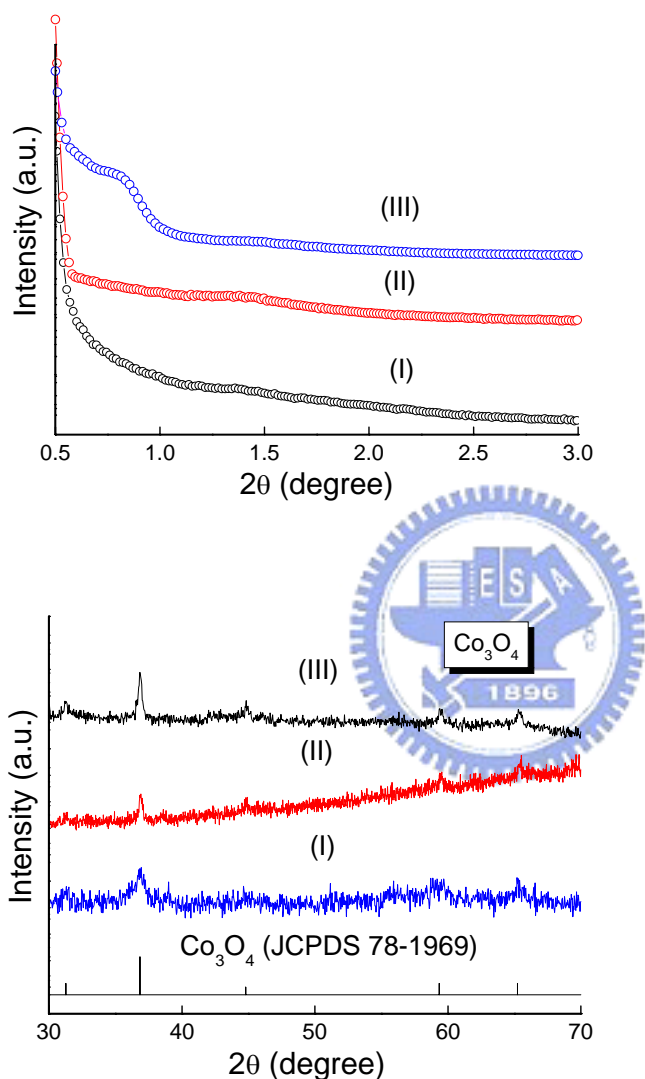
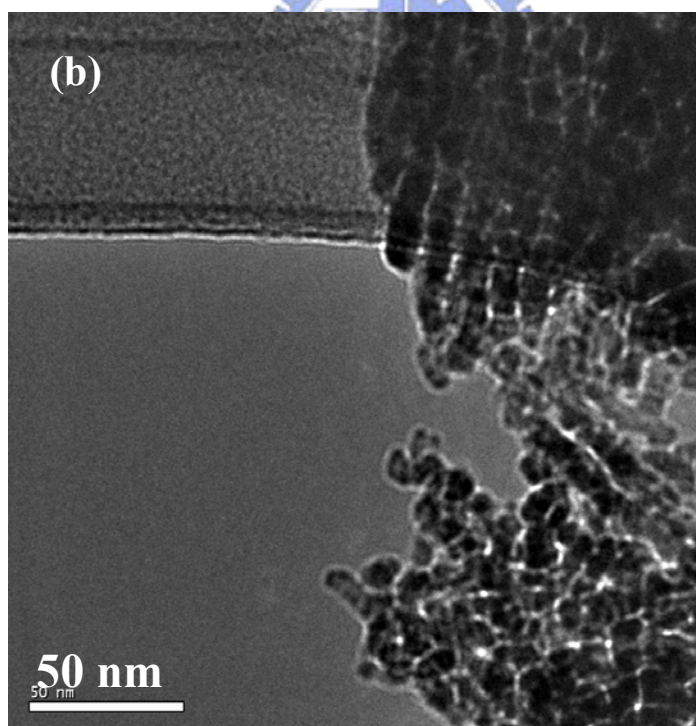
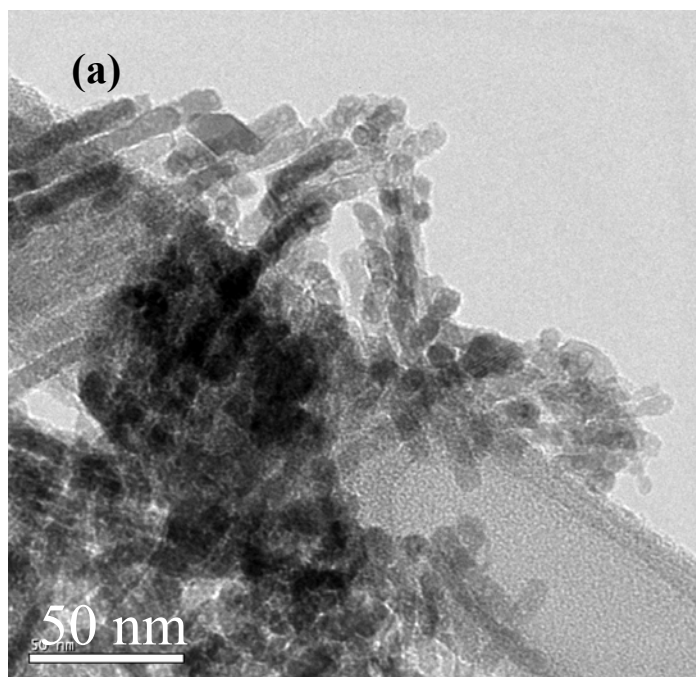


Figure 5.20 XRD patterns at the (a) low-angle and (b) wide-angle regions of the mesostructured cobalt oxide materials, with templates prepared at different temperatures: (I) 40°C , (II) 60°C , and (III) 100°C .



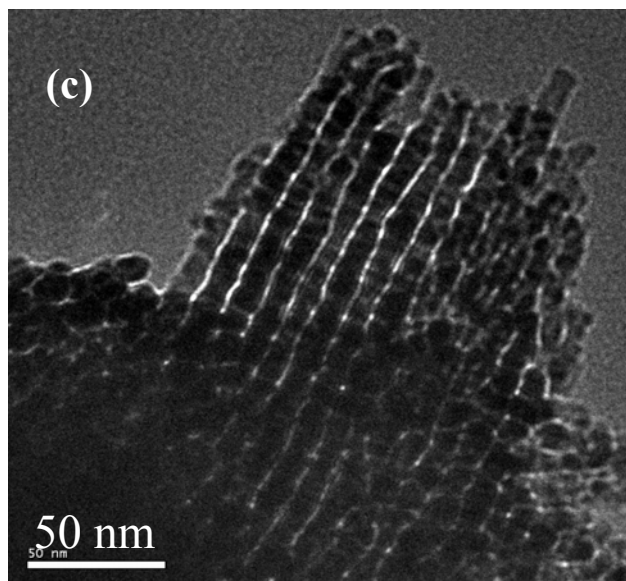


Figure 5.21 Effect of size variation in 2D hexagonal parent silica on the preparation cobalt oxide. TEM images of preparation cobalt oxide at different crystallization temperatures: (a) 40°C, (b) 60°C, and (c) 100°C.

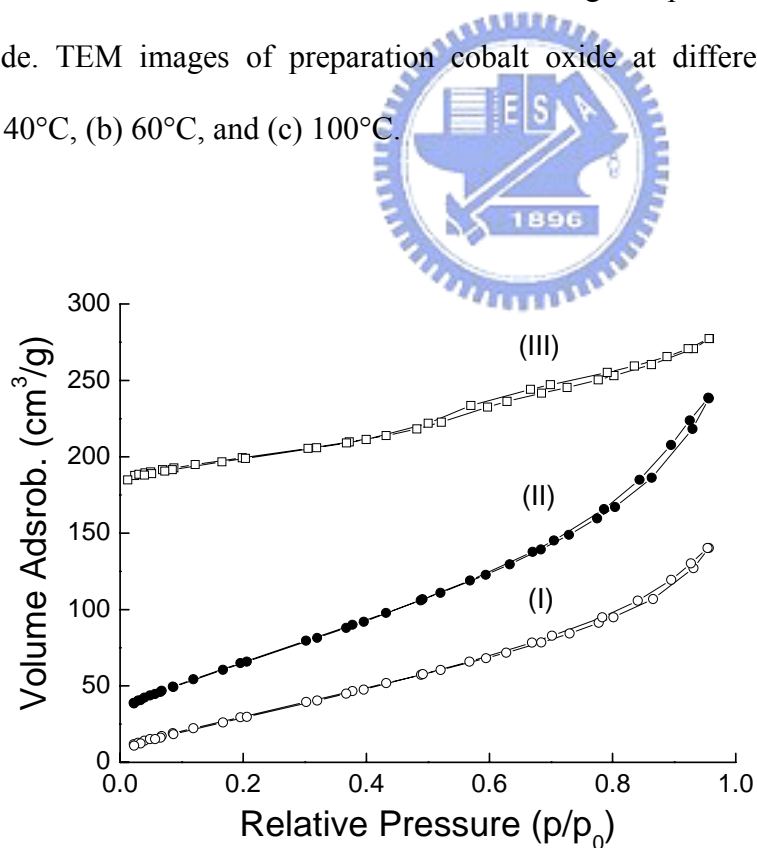


Figure 5.22 Nitrogen adsorption-desorption isotherms of cobalt oxide prepared from SBA-15 templates with different crystallization temperatures: (I) 40°C, (II) 60°C, and (III) 100°C.

Accordingly, the mesoscale order of the cobalt oxide replica prepared at higher crystallization temperature is improved. Hence, a highly condensed silica framework is in favor of the mesoscale order of the cobalt oxide replica. Therefore, to archive a better mesoscale order of the final oxides the tailoring of the host-guest interactions is paramount; in order to hinder the formation of highly dispersed species. For preparing of mesostructured cobalt oxide materials, the cobalt precursor may strongly interact with the silica walls to form highly surface species and may also form a monolayer on the internal surface of SBA-15 during the calcinations, which leads to the imperfect replication of the SBA-15 mesostructure after the removal of the hard template. Therefore, the host-guest interaction should be weakened in the synthesizing process of cobalt oxide in order to perfectly replicate the pore structure. The schematic diagram in Figure 5.23 explains two situations in the solid-state procedure: the first situation deals with the self-supported mesostructure of the samples which replicates the structure of the SBA-15 support well owing to a rather weak silica-precursor interaction, and the second situation is that a surfaces instead of the bridge between the pores, so that separated materials are obtained.

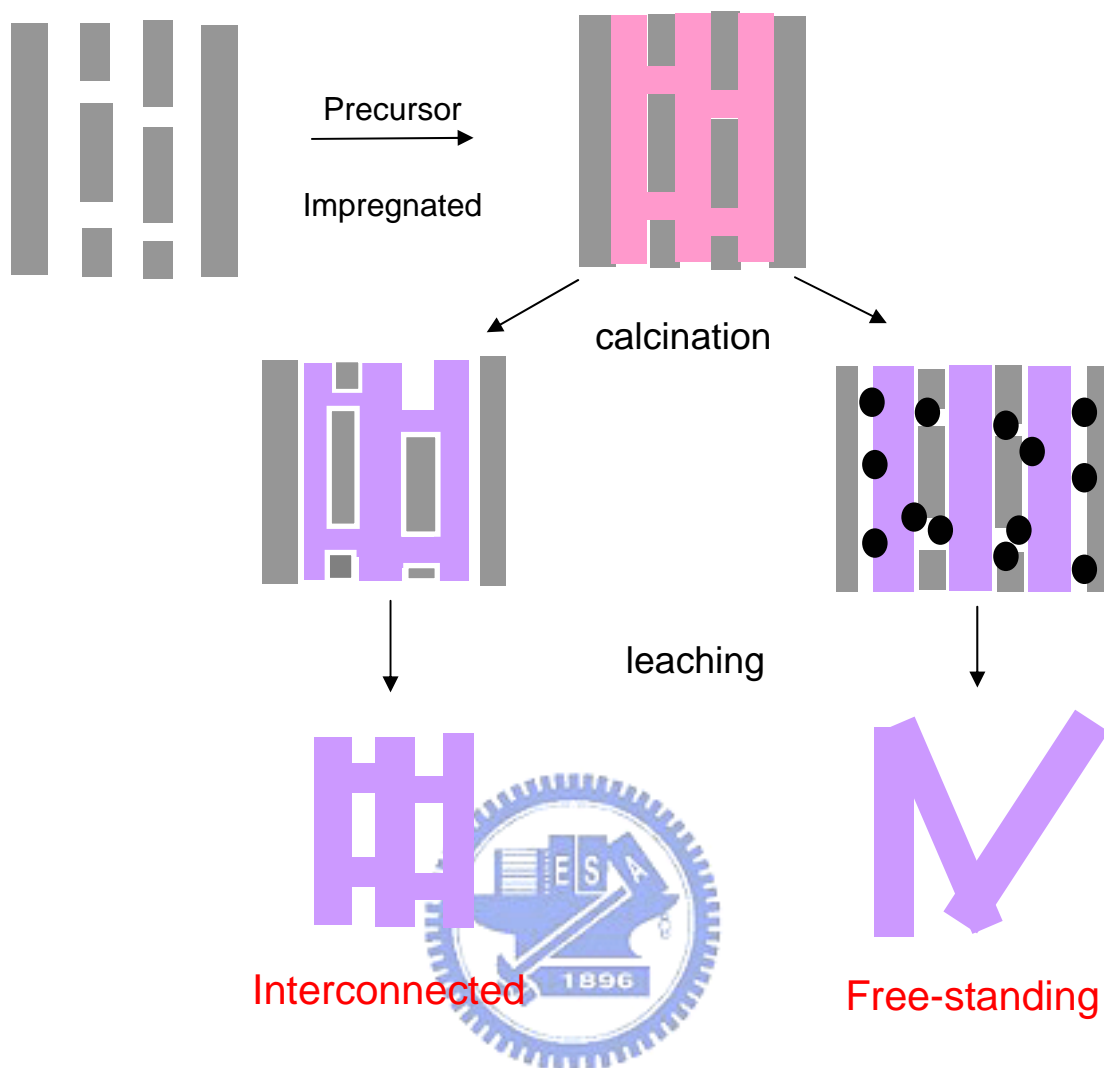


Figure 5.23 Schematic diagram for preparing metal oxide arrays.

Different voltage levels (1.0–10.0 V) were applied and measurements were taken to determine the mesostructured cobalt oxide sensor performance. As shown in Figure 5.24, a larger voltage input prompted a higher response compared to that of a lower voltage input; additionally, a long recovery time was obtained with the high-voltage condition. It is remarkable that the applied voltage controls the sensor responses; indeed, it appears that the gas-sensing response was improved by increasing the applied voltage. However, the high applied voltage result in a long recovery time, because of the increase in transfer carriers from

cobalt oxide to the electrodes. This can be explained by changes in the Ohmic junction formation between the cobalt oxide and electrodes. There exists a potential barrier for electron transfers, between the cobalt oxide and the metal. The band-bending or built-in potential of the electrode and cobalt oxide connection is given by:

$$V = \Phi_m - \Phi_s - V_a \quad (1)$$

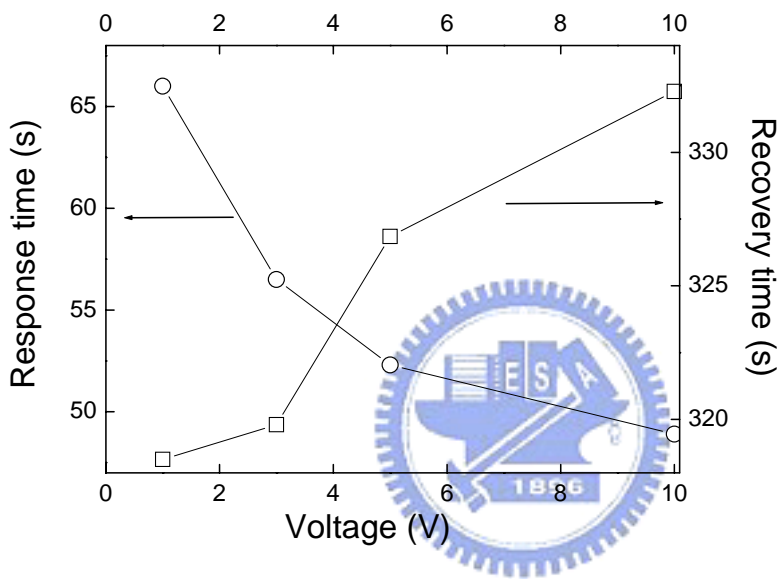


Figure 5.24 Sensor response and recovery times of mesostructured materials with applied voltages, modulated from 1 V to 10 V.

The ease of electron-transfer, facilitated by the lowering of the forward bias-induced barrier, lowering may enhance the gas-reacting response; this also explains the long recovery time inherent in the higher applied voltage case. By increasing the number of electrons transferred from cobalt oxide to the electrode by virtue of increasing the input voltage, more electrons might be captured by CO molecules, resulting in the need for a longer recovery time. The optimal output voltage of the mesostructured sensor was 3 V.

The operating temperature is the critical parameter for the sensors. Figure 5.25 shows the effect of working temperature on the saturation sensitivity of mesostructured cobalt oxide materials towards CO gas. It was observed that the working temperature plays a vital role in determining the sensitivity of the films. For a particular concentration of CO, the sensitivity first increased from 7% to 11.5% as the temperature is increased from 150°C to 200°C, and then decreased to 9.6% when the temperature was further raised to 250°C. In general, there exists an optimal working temperature for a sensor, where there is maximum sensitivity to the gas of interest. At a low temperature, the CO molecules do not have enough energy to adsorb onto the carbon surface; on the other hand, a reduction of sensitivity at high temperatures should be attributed to the difficulties related to exothermic CO gas adsorption.

Therefore, the optimal working temperature of mesostructured cobalt oxide sensing materials is 200°C. SEM images of the mesostructured cobalt oxide sensing material on the alumina substrate were taken and are featured in Figure 5.26. It was found that the mesostructured cobalt oxide sensing material showed a rod-like morphology; however, it was prone to forming aggregates, because the isopropyl alcohol (IPA) was used as the solvent for printing. This aggregate morphology in the mesostructured cobalt oxide materials might influence the sensor's response. Since 200°C was found to be a suitable temperature for CO detection, further studies were performed at this temperature. The sensor-resistance results to different concentrations of CO gas are shown in Figure 5.27. First, the sensor's response was evaluated in the 10–70 ppm range; under this condition, the response to a lower concentration was still high. The sensor-response results *vis-à-vis* different concentrations of CO in synthetic air are shown in Figure 5.28; as seen there, the sensor was able to respond quickly at low CO concentrations. The average response and recovery times were 6 min and 42 min, respectively [105].

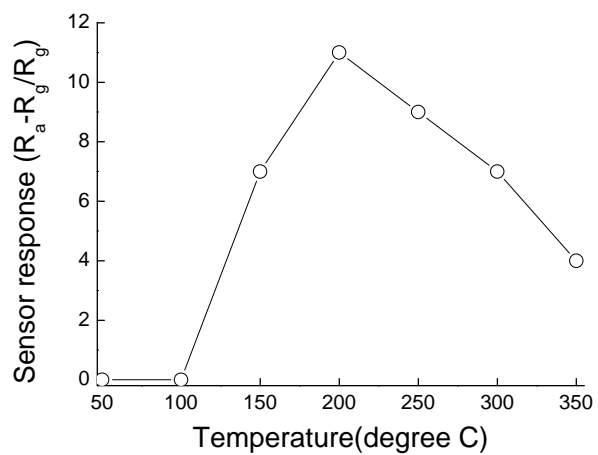


Figure 5.25 Sensor response of mesostructured cobalt oxide materials to 20 ppm CO at different working temperatures.

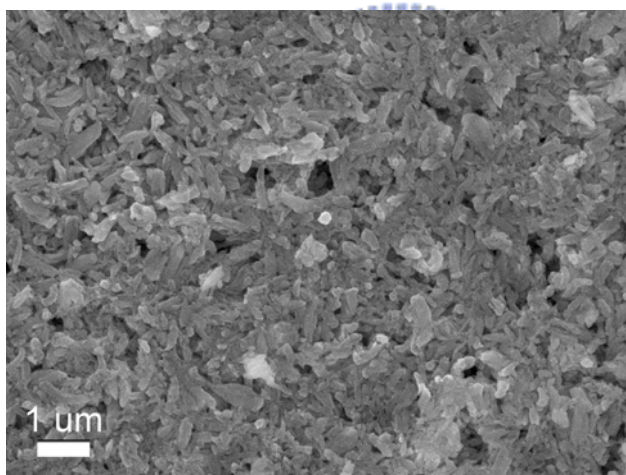


Figure 5.26 SEM images of mesostructured cobalt oxide sensing materials printed on the alumina substrate.

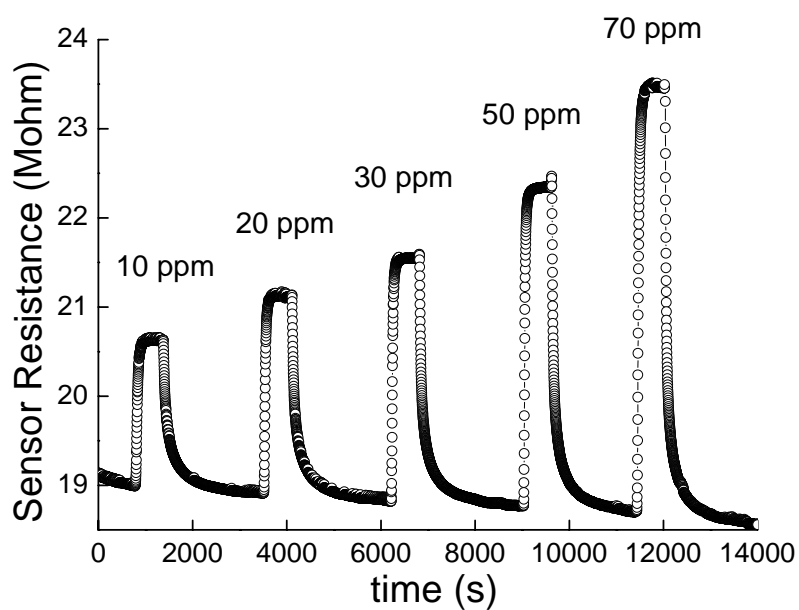


Figure 5.27 Resistance variations of mesostructured cobalt oxide materials to different concentrations of CO in synthetic air at 200°C.

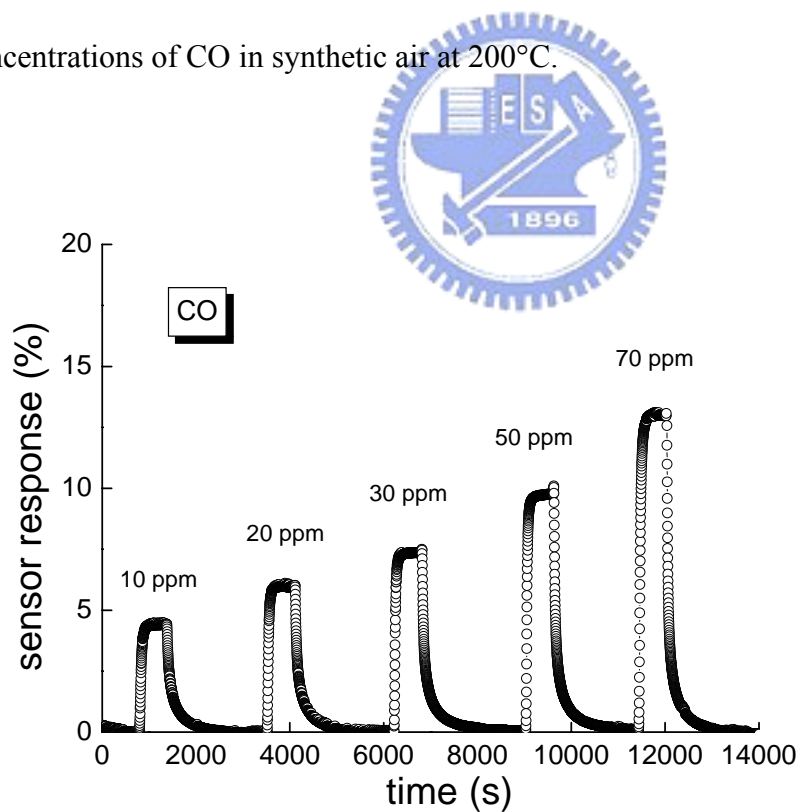
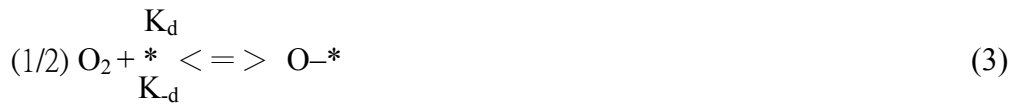
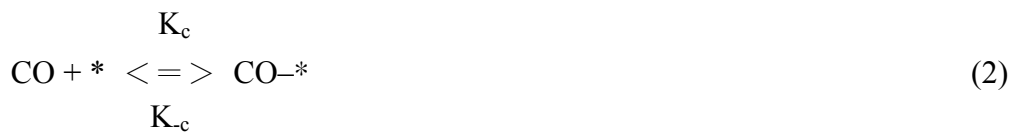


Figure 5.28 Sensor responses of mesostructured cobalt oxide materials to different concentrations of CO in synthetic air.

Figure 5.27 also shows that with the increasing resistance of mesostructured cobalt oxide material, the mesostructured cobalt oxide sensor behaved like a p-type semiconductor; this was because CO gas was injected, on account of it being an electron-donating gas. The response behavior of this sensor was similar to that of the carbon nanotube sensors [106]. Additionally, it is interesting to note that the sensor response of mesostructured cobalt oxide material seemed not to be affected by the aggregated morphology. The optimal responses were 4.3%, 6.0%, 7.4%, 9.7%, and 13% at concentrations of 10 ppm, 20 ppm, 30 ppm, 50 ppm, and 70 ppm, respectively. It is worth mentioning that the mesostructured cobalt oxide sensor showed a better sensor response than those with non-mesoporous materials [107]. It has been proposed that the oxidation of CO on cobalt oxide take the form of a redox reaction, where gas-phase CO is adsorbed on cobalt sites; and the adsorbed CO would then react with lattice oxygen atoms to form CO₂ [108, 109]. The probable mechanism of the cobalt oxide catalysis for CO oxidation can be inferred from the linear relationship between log *S* versus log [CO]. Equation (2) represents the adsorption and desorption of CO, and equation (3) represents the adsorption and desorption of O₂; equation (4) represents the surface reaction of CO and O₂.



where *, CO-*, and O-* represent vacant, CO-occupied, and O-occupied sites on the surface, respectively. *K_c* and *k_d* are the rate constants of the adsorption of CO and O₂, while *k_{-c}* and *k_{-d}* are the rate constants of the desorption of CO and O₂, respectively. *k_e* is the rate constant

of the surface reaction between adsorbed CO and O. Based on a steady-state approximation, θ_{CO} can be expressed as:

$$\theta_{CO} = K_C P_{CO} / (1 + K_d P_{O_2} + K_C P_{CO}) \quad (5)$$

where P_{CO} and P_{O_2} are the partial pressure of CO and O₂, respectively, and $K_C = k_c/k_{-c}$ and $K_d = k_d/k_{-d}$. Since it is assumed that the total number of adsorbed oxygen atoms is constant at a fixed temperature, the resistance of air is constant ($R_{air} = \text{constant}$).

5.3 Mesostructured carbon materials

Recently, Ryoo et al. developed an ordered mesoporous carbon (CMK-3) from mesoporous silica templates such as MCM-48, SBA-15, and SBA-1, using sucrose as the carbon source. These novel mesoporous carbon materials are characterized by large specific surface areas, large specific pore volumes, and electrical conductivity. Therefore, both the simultaneous control of structural and textural properties of well-ordered mesoporous carbon and their applications for gas-sensing are studied.

The SBA-15 materials were used as a template, to synthesize mesostructured carbon via the template replication method. First, we ascertained the effect of carbonization temperature on the structural ordering of the resulting carbons. Figure 5.29 shows the low-angle XRD patterns for mesostructured carbon at different carbonization temperatures. The XRD patterns at 600°C show no visible low-angle reflection; when the carbonization temperature exceeds 700°C, however, the XRD patterns show well-resolved reflections, thus indicating the enhanced structural ordering. The patterns therein are consistent with the 2D hexagonal symmetry derived from the SBA-15 structural order. The cell parameter of the mesostructured carbon was tuned from 8.56 nm to 8.19 nm, along with increases in the carbonization temperatures. It was noted that the cell parameter of the porous carbon was reduced by 9%, as compared to the silica template; structural shrinkage occurring in the porous silica template has been reported previously by various authors [110, 111]. When the silica template's spatial

dimensions were unconfirmed, the reaction would accelerate shrinkage of the pores. In addition, the intensity of the XRD peaks decreased for carbons prepared at higher carbonization temperatures.

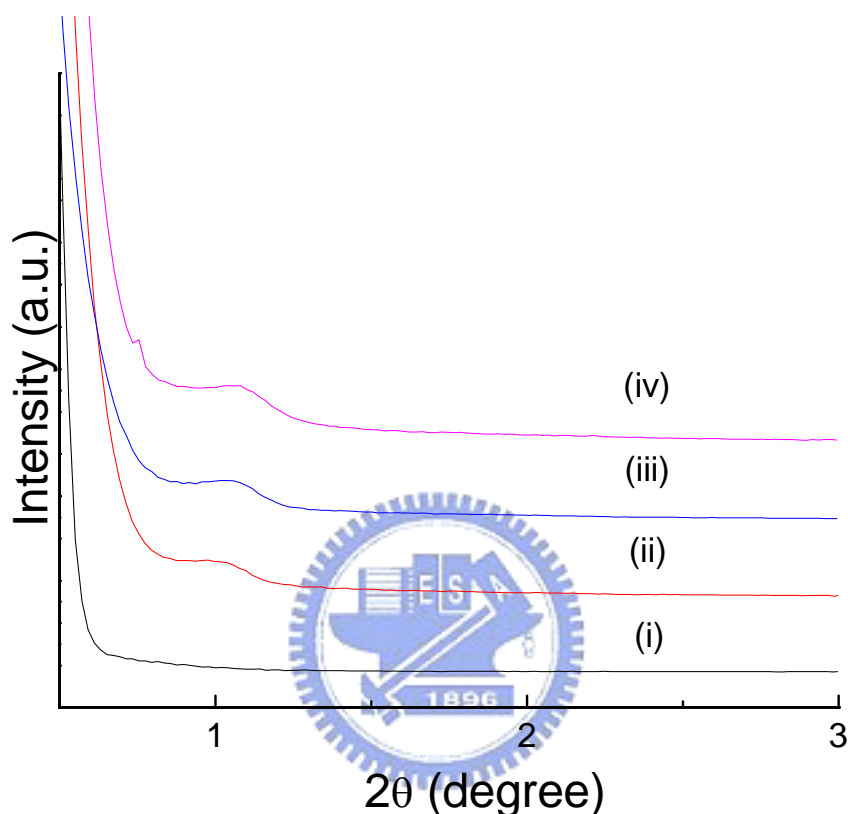
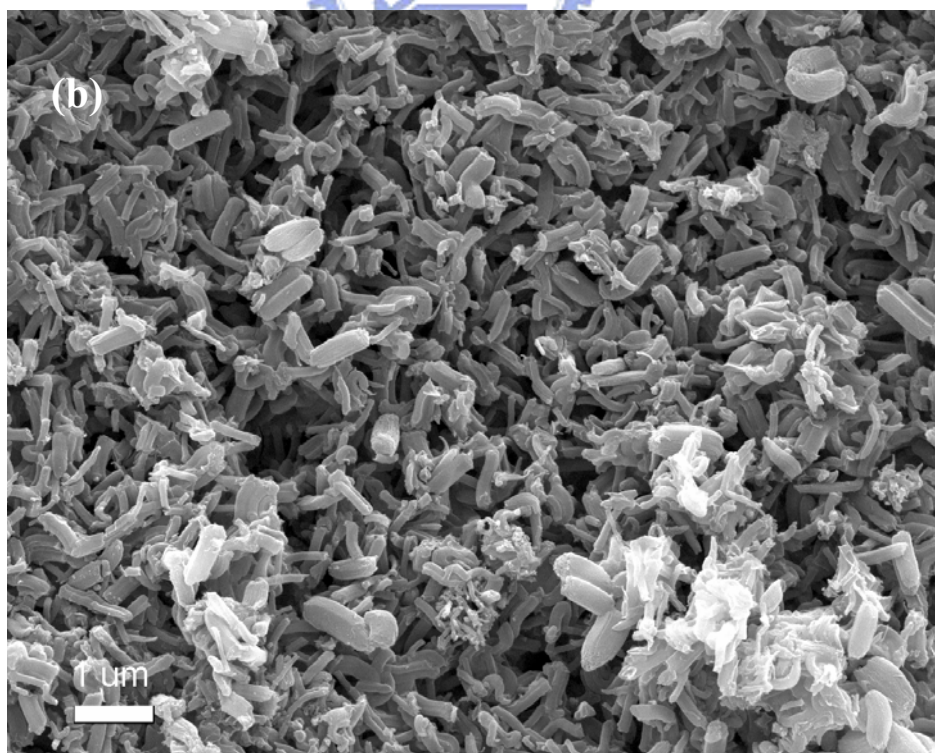
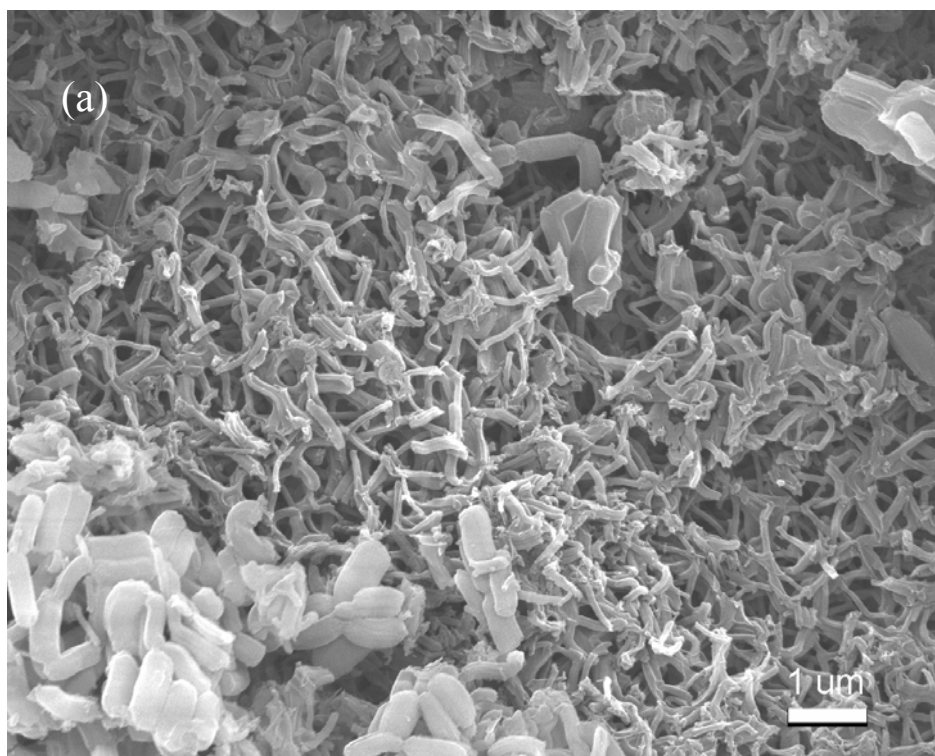


Figure 5.29 Low-angle XRD patterns of mesostructured carbon synthesized from SBA-15 silicas at different carbonization temperatures: (I) 600°C, (II) 700°C, (III) 900°C, and (IV) 1,000°C.

It is noteworthy that the XRD patterns of the mesostructured carbon were in low-angle peaks, implying the presence of some mesostructural ordering. Both the SEM images of the mesostructured carbon during the carbonization treatment showed a rod-like morphology (Figure 5.30), and both the length and diameter thereof were a little shorter and thicker at higher carbonization temperatures. The length of the mesostructured carbon varied from 1.5

μm to $1.0\ \mu\text{m}$; the diameter also varied, from $80\ \text{nm}$ to $200\ \text{nm}$. These variances were assumed to be caused by the reconstruction of mesostructured carbon. The TEM image illustrates that the well-ordered pore channels; these state is consistent with the corresponding XRD pattern (Figure 5.31).

These carbons were further investigated using nitrogen sorptions, as shown in Fig. 5.32. These carbons exhibit nitrogen sorption isotherms typical of well-ordered mesostructured carbon [112]. These results demonstrate that the mesostructured carbon belongs to type IV, according to the International Union of Pure and Applied Chemistry (IUPAC) classification. The sorption isotherms showed a large increase in the relative pressure (p/p_0) range of $0.4\text{--}0.6$ for mesostructured carbon. The sharpness of the inflection step reflected the uniform pore-size distribution, and the p/p_0 position corresponded to pore diameters in the mesopore range. The average specific surface area of mesoporous carbon was $1200\ \text{m}^2\ \text{g}^{-1}$, and the total pore volume was $1.2\ \text{cm}^3\ \text{g}^{-1}$, while the pore-size distribution of mesoporous carbon, as calculated by the Barrett-Joiner-Halenda (BJH) method, yielded an average pore size of $3\ \text{nm}$. It is noteworthy that variations in the carbonization temperatures had little effect on the pore diameter of the mesostructured carbons. Given the variation in d-spacing of the mesostructured carbons discussed above, the unchanging pore size suggests that the pore-wall thickness varies according to the carbonization temperature. A rough estimate indicates pore-wall thicknesses of approximately 8.1 , 7.3 , 6.9 , and $5\ \text{nm}$ for carbons prepared at 600 , 700 , 900 , and 1000°C , respectively; wall thickness tends to decrease at higher carbonization temperatures.



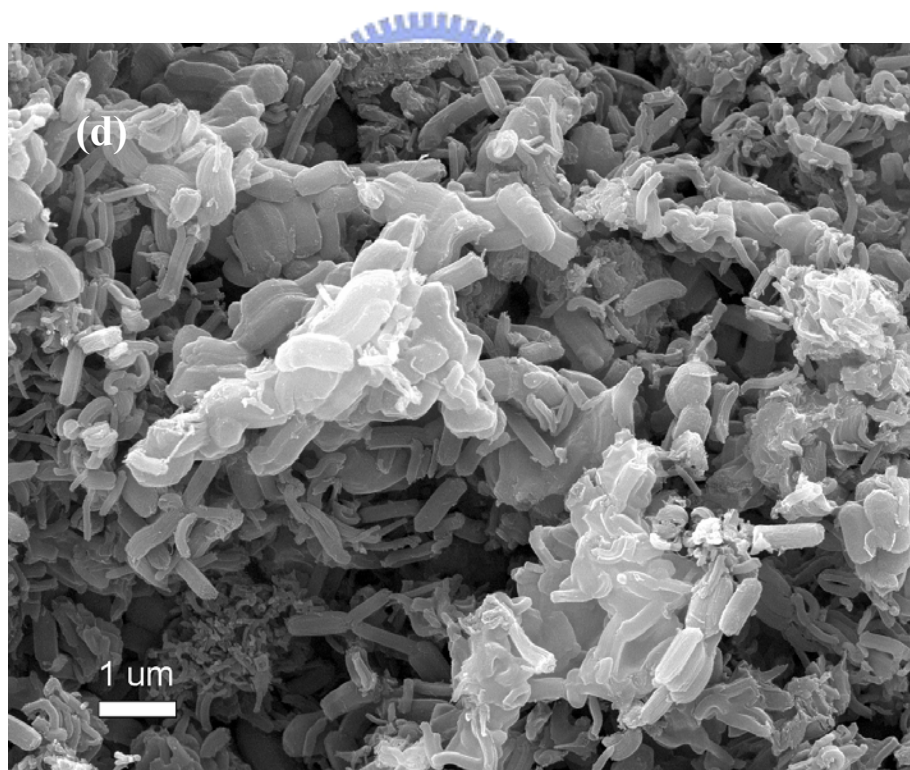
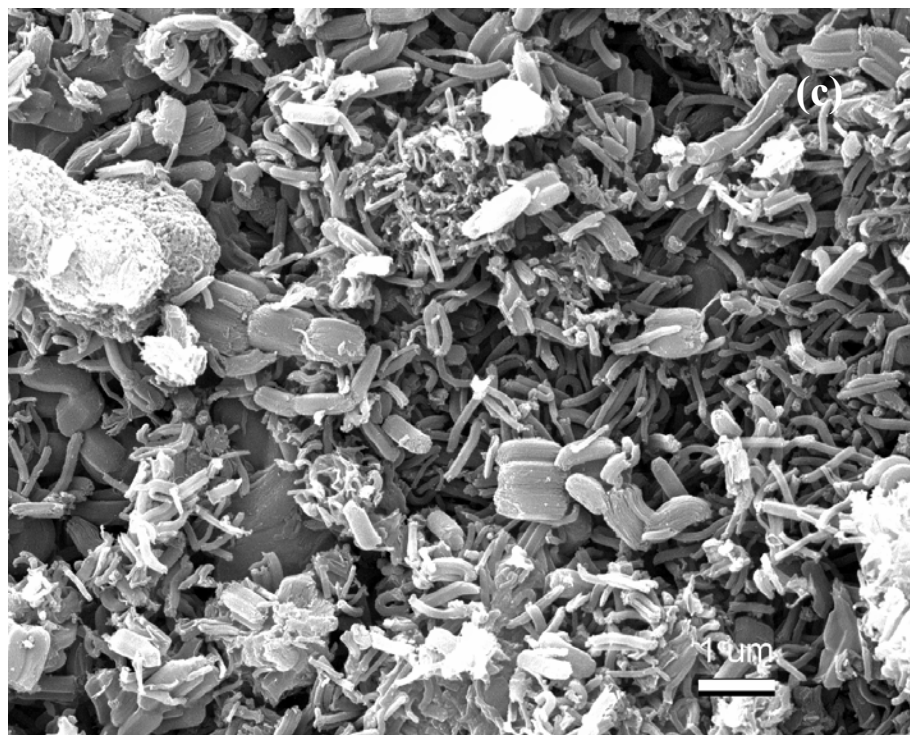


Figure 5.30 Representative SEM image for mesostructured carbon at different carbonization temperatures: (a) 600°C, (b) 700°C, (c) 900°C, and (d) 1,000°C.

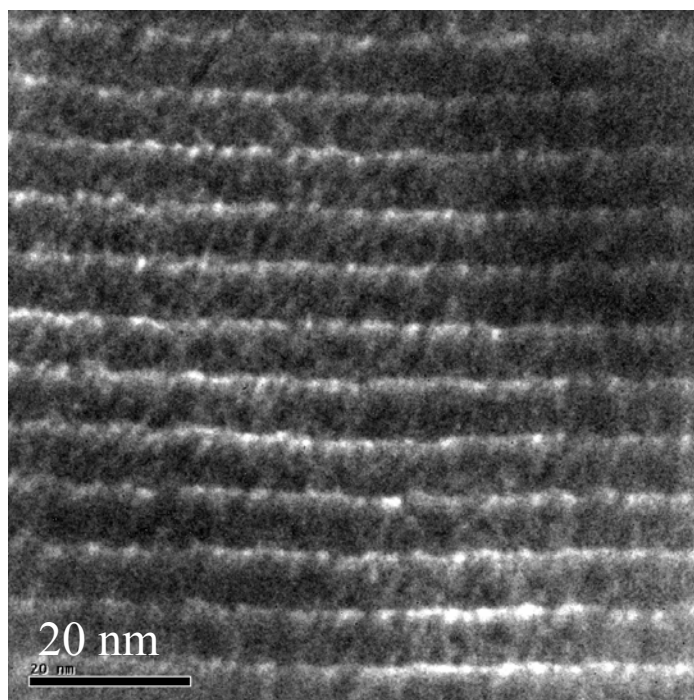


Figure 5.31 TEM images of the mesostructured carbon after carbonization treatment at 900°C.

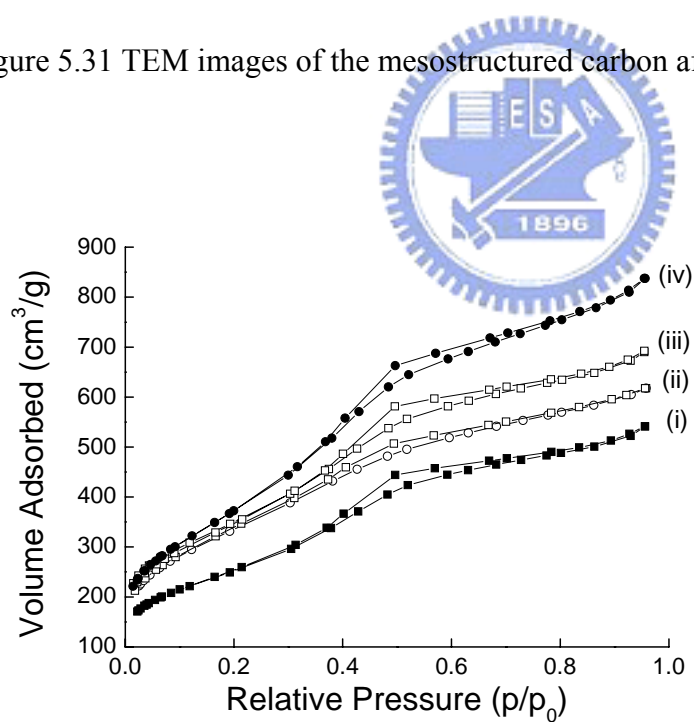
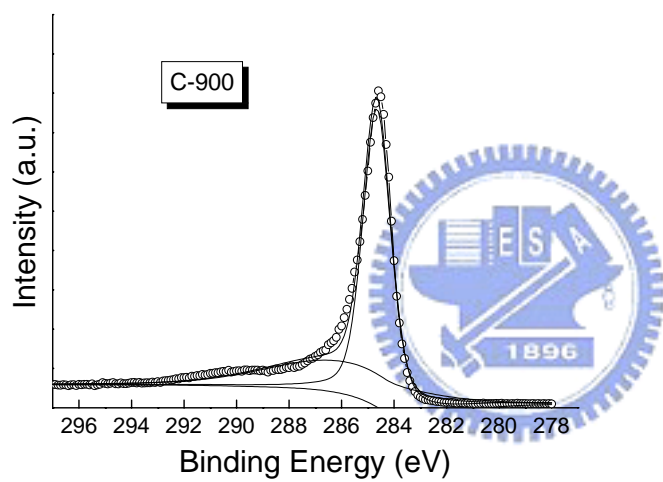
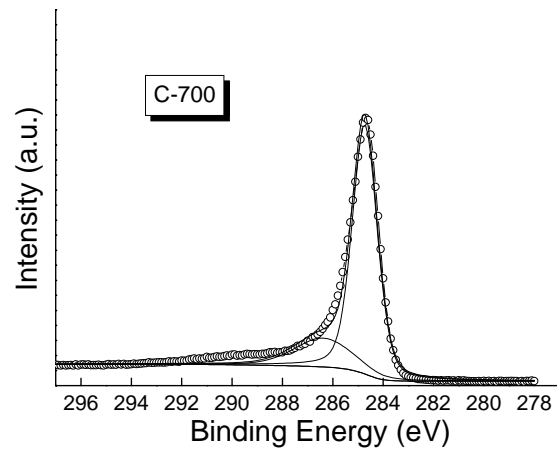
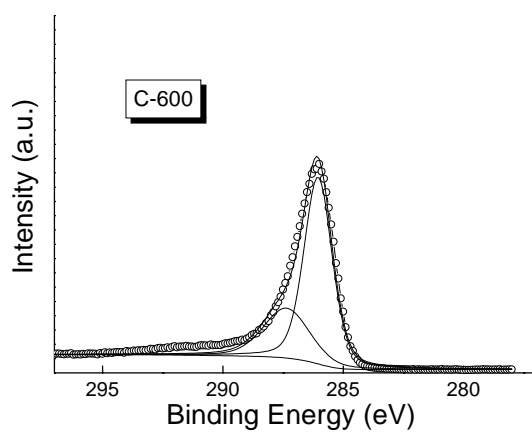


Figure 5.32 Nitrogen adsorption-desorption isotherms of mesostructured carbon at different carbonization temperatures: (I) 600°C, (II) 700°C, (III) 900°C, and (IV) 1,000°C.



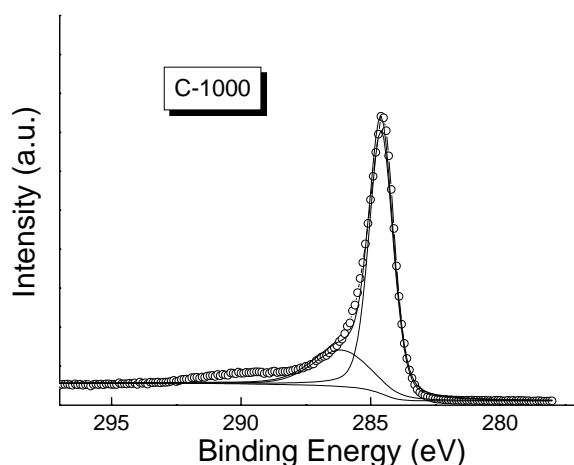


Figure 5.33 XPS spectra of mesostructured carbon carbonized at different temperatures: (a) 600°C, (b) 700°C, (c) 900°C, and (d) 1,000°C.

Figure 5.33 shows the XPS spectra of the mesostructured carbon. The carbon spectra were fitted to two peaks: a peak for carbon atoms with bonds to carbon and/or hydrogen atoms (284.6 eV), and another peak that bonds to oxygen atoms (C-OH, BE = 286.2 eV). However, at the carbonization temperature of 600°C, abnormal peaks at 287.0 eV and 288.4 eV were observed (C = O and COOH). These peaks also contain a contribution from carbon atoms, with one bond to fluorine. Moreover, the peaks of C-OH decreased as the carbonization temperatures increased, indicating that residual water had been removed.

Judging from the effect of the carbonization temperature on the structural ordering of mesostructured carbons synthesized from SBA-15 template, a temperature of 900°C was chosen to synthesize carbons from other SBA-15 silica templates (prepared at 40°C, 60°C, and 100°C), in an attempt to vary the pore size and morphology of the carbons. The remainder of this paper is therefore concerned with variations in porosity and morphology that result from the use of different SBA-15

silica templates. A carbonization of 900°C was used to synthesize mesostructured carbons from various SBA-15 templates. The resulting mesostructured carbons exhibit type-IV nitrogen sorption isotherms (Fig. 5.34(a)) with a well-developed capillary condensation step into mesopores in the partial pressure range of 0.35–0.70, indicating good mesostructural ordering. On the other hand, the carbons prepared from 40 and 60°C silica templates display an isotherm that suggests the presence of micropores and small pores. Fig. 5.34(b) shows that the mesostructured carbons have relatively narrow pore size distributions. It is interesting to note that the maximum pore-diameter of the mesostructured carbons largely depends on the silica template. The pore diameter is larger for mesostructured carbons prepared at higher crystallization temperatures. The pore size of the mesostructured carbons was tunable, to between 3.2 and 4.0 nm, depending on the nature of the SBA-15 template. Moreover, the overall porosity of the mesostructured carbons was also influenced by the nature of the SBA-15 templates. In general, mesostructured carbons have highly textural properties at high silica temperatures, which are also likely to have high surface areas and pore volumes. The mesostructured carbon prepared from SBA-15 at 100°C, exhibits the highest surface area and pore volume, at 1194.2 m² g⁻¹ and 1.05 cm³ g⁻¹, respectively. The low-angle XRD patterns of the mesostructured carbon synthesized from various SBA-15 templates are shown in Fig. 5.35.

The structural ordering of the mesostructured carbons was influenced by the nature of the SBA-15 templates. The patterns at higher silica temperatures exhibit a low level of structural ordering, compared to those of other mesostructured carbons. This observation is consistent with the isotherm and pore-size distribution curves in Figure 5.34; however, the overall result emerges that a high level of ordering is observed in the mesostructured carbon synthesized at higher crystallization temperatures. Figure 5.36 shows SEM images of the mesostructured carbons prepared

from various SBA-15 templates.

It is interesting to note that samples synthesized at lower crystallization temperatures (e.g., 40 and 60°C), exhibit a rhombus morphology, whereas samples at higher crystallization temperatures (100°C) bear a rod morphology. This is an interesting observation, and it suggests that the pore size of the silica templates directs the morphology of the mesostructured carbons toward the formation of rhombus-shaped particles. We believe that the formation of rhombus morphologies is related to the smaller pore size of the SBA-15 templates. The role that the pore size of the silica template plays in the formation of rhombus morphology can be explained as follows: During the carbonization process, the carbon precursor is initially in contact with the surface of the SBA-15 template, before diffusion into the interior of the silica. A high carbonization temperature accelerates the carbonization of the sucrose in contact with the SBA-15 templates. If the pore diameter of the SBA-15 template is small, the carbonization process could quickly block the pore channels and hinder diffusion of the sucrose into the core of the silica templates. Thus, narrow pore channels are more susceptible to pore-blocking than wider pores. Removal of the silica by HF etching results a rhombus carbon; on the other hand, the pore diameter of the SBA-15 is large, and the pore will diffuse deeply into the core of the silica to form uniform carbon/silica composites. Removal of the silica yields carbon rods. Mesostructured carbon synthesized at different crystallization temperatures is shown in Figure 5.37. The TEM images of mesostructured carbons synthesized from the small-pore SBA-15 templates (40°C and 60°C) clearly show a wormhole-type morphology. We note that the wormhole-type morphology is consistent with the porosity and XRD patterns of mesostructured carbons synthesized at lower crystallization temperatures.

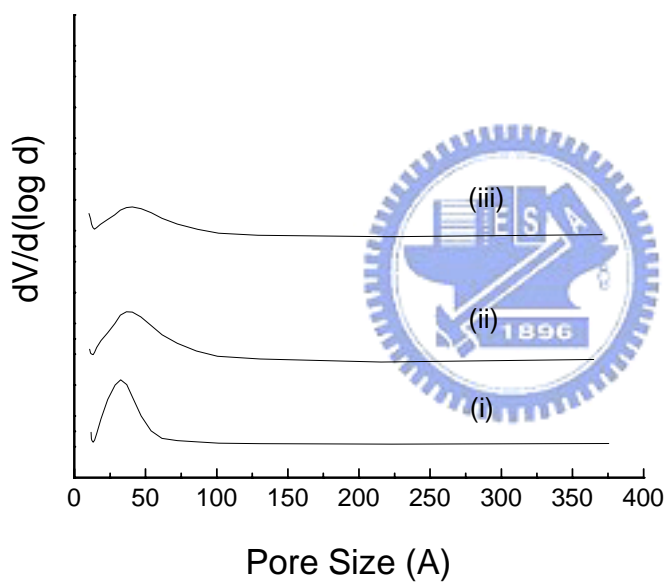
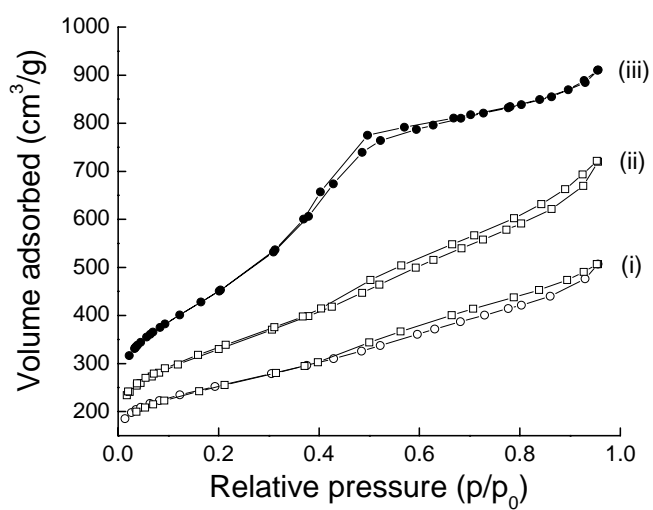


Figure 5.34 (a) Nitrogen adsorption-desorption isotherm and (b) pore-size distribution curves of mesostructured carbon from various SBA-15 templates: (I) 40°C, (II) 60°C, and (III) 100°C.

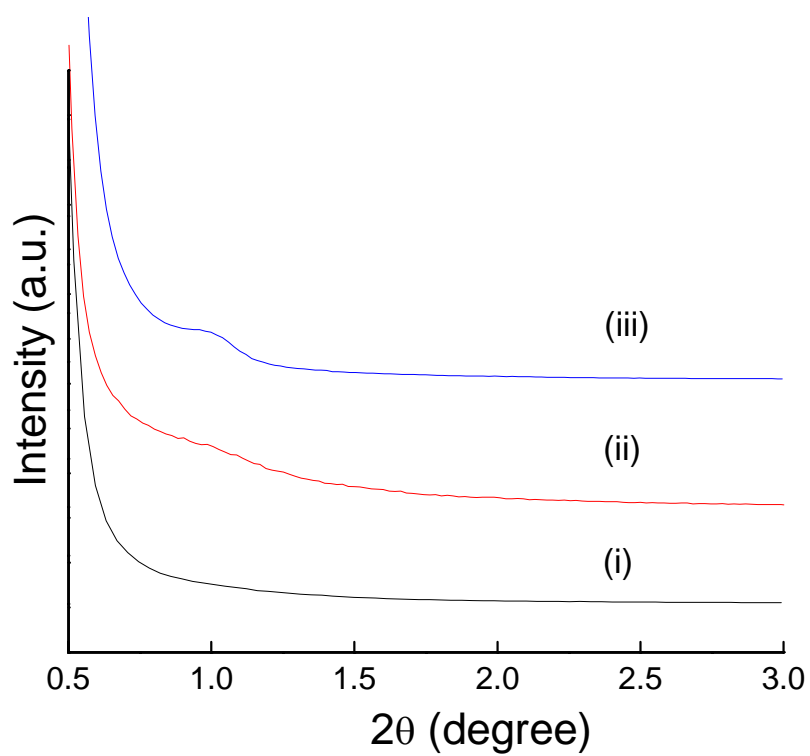
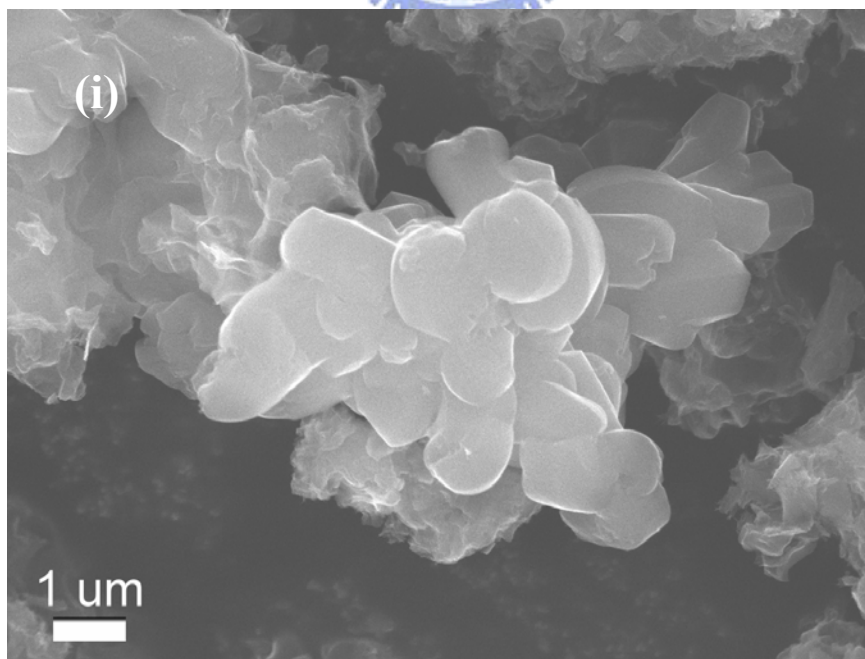


Figure 5.35 Low-angle XRD patterns of mesostructured carbon synthesized from various silica templates: (I) 40°C, (II) 60°C, and (III) 100°C.



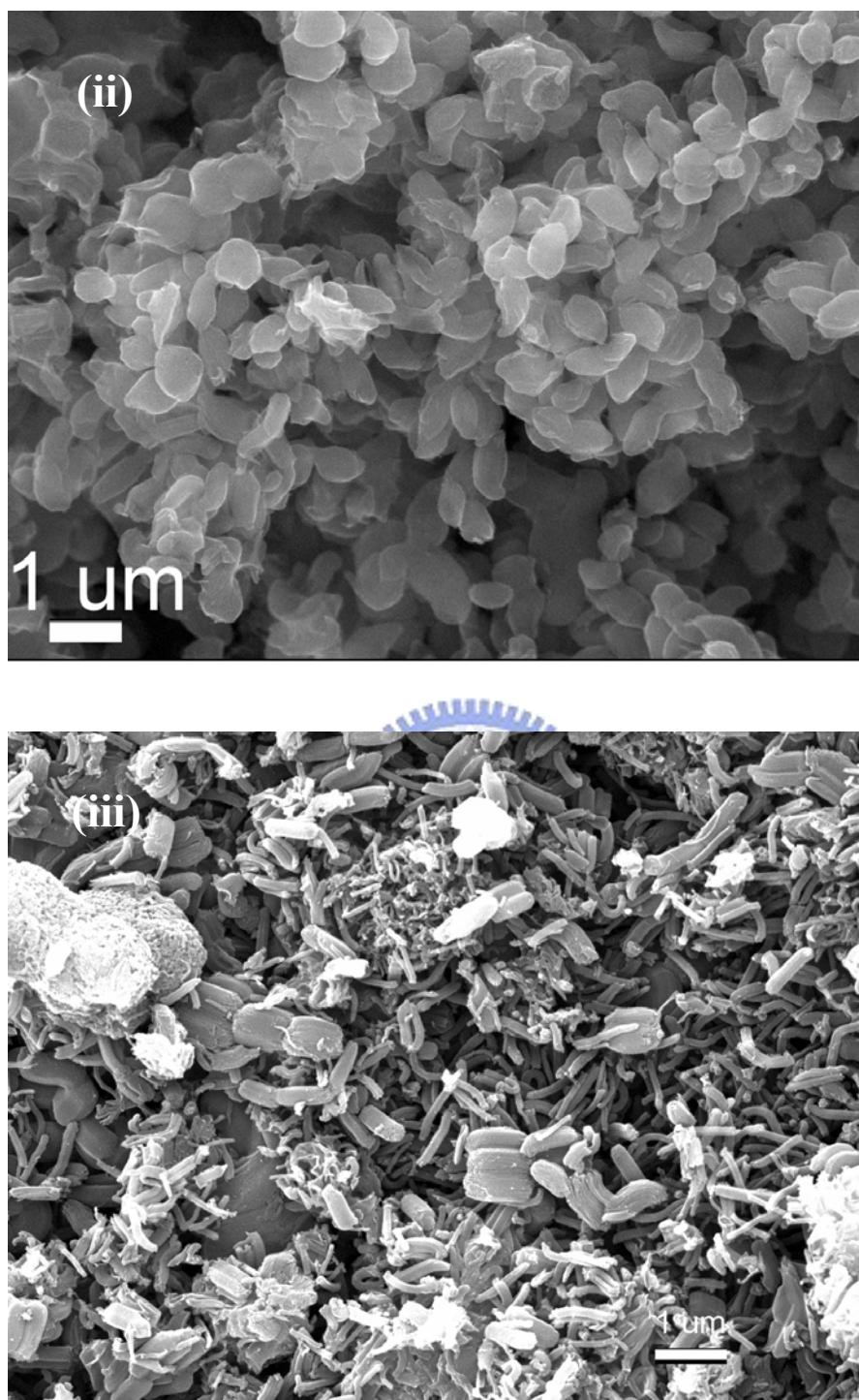
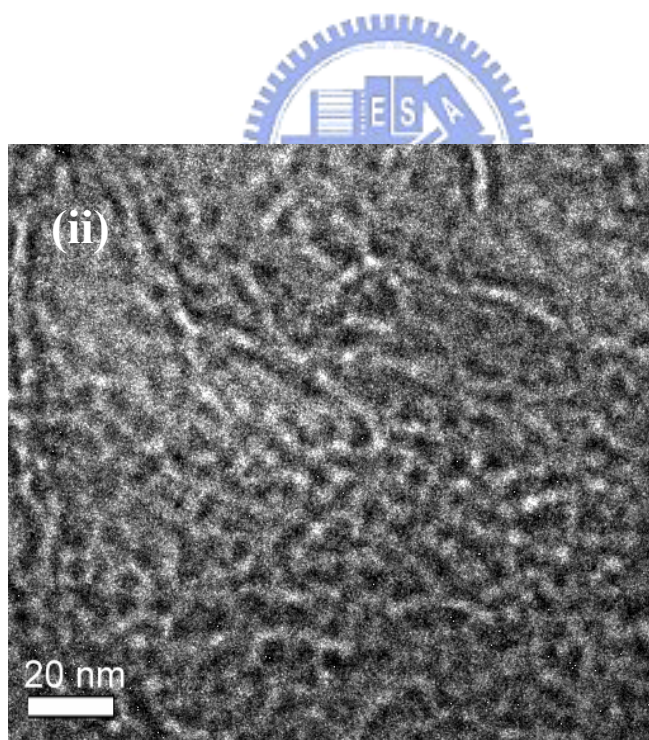
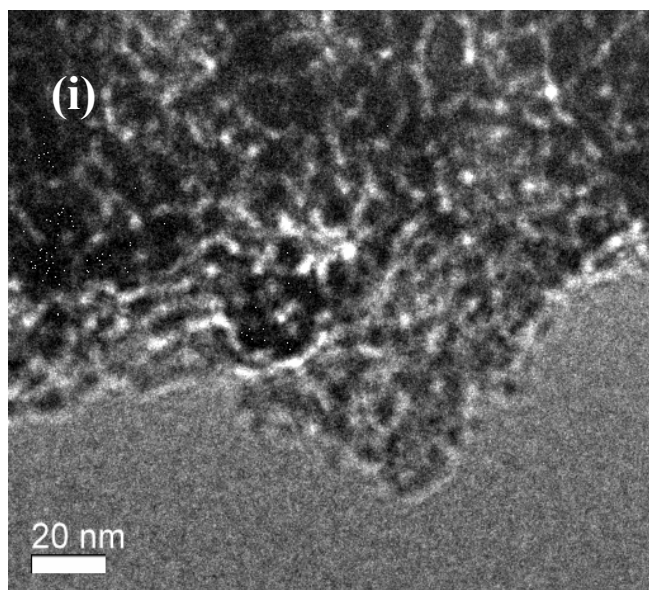


Figure 5.36 Representative SEM images of mesostructured carbon materials synthesized from various SBA-15 templates: (I) 40°C, (II) 60°C, and (III) 100°C.



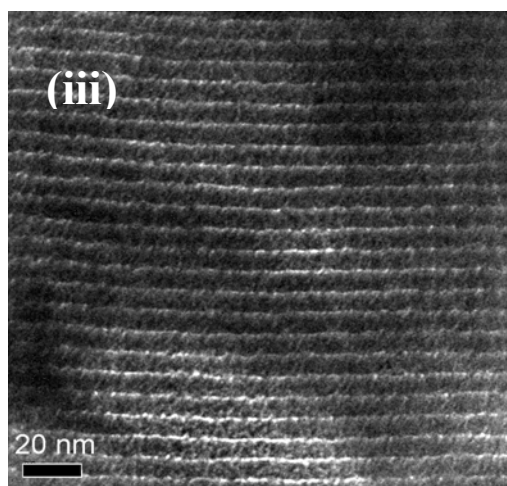


Figure 5.37 Representative TEM images of mesostructured carbon materials synthesized from various SBA-15 templates: (I) 40°C, (II) 60°C, and (III) 100°C.

Figure 5.38 shows SEM images of the mesostructured carbon material printed onto an alumina substrate. The IPA solvent affects the morphology of mesostructured carbon, causing aggregation. We suggest that the aggregate morphology might be influenced by the sensor response. In general, the working temperature plays a vital role in determining the film sensitivity; for mesostructured carbon sensing materials, the optimal temperature is 250°C. The sensor response of the mesostructured carbon to different CO concentrations is shown in Figure 5.39. It was observed that the response increased with an increase in ambient CO gas concentration. Since CO is an electron-donating gas, the mesostructured carbon sensor behaved like a p-type semiconductor, due to the increasing resistance of the mesostructured carbon. The response behavior of this sensor was similar to that of carbon nanotubes [113]. Therefore, the optimal sensitivities of this sensor were 0.1%, 0.2%, 0.3%, 0.4%, and 0.6 % for concentrations of 10 ppm, 25 ppm, 30 ppm, 50 ppm, and 70 ppm, respectively. The longer response and recovery times of the mesostructured carbon sensor were around 6 min and 60 min, respectively.

Additionally, it is interesting to note that the sensor response of mesostructured carbon material was affected by aggregate's morphology. The aggregate would block the pore channel, making it difficult for gas molecules to pass. On the other hand, according to the Knudsen diffusion, a smaller pore also resists pore accessibility [106, 107]. The gas-sensing mechanism of the mesostructured carbon sensor has been attributed to electronic interactions between mesostructured carbon and adsorbed gas molecules, which is similar to the case with carbon nanotubes (CNTs) sensors [114, 115]. For example, CO molecules decrease the positive hole carrier in p-type semiconducting carbon and increase the resistance. From the viewpoint of the energy band gap, the electronic interaction results in the carbon Fermi level shifting close closer to the valence band. As depicted in Figure 5.40, the barrier (ϕ_B) between the p-type semiconductor and the metal electrode is simply given by:

$$\phi_B = E_G + X_S - \phi_M, \quad (6)$$

where E_G and X_S are the band gap and electron affinity of the semiconductor, respectively. Equation (6) implies that the Schottky barrier, ϕ_B , is sensitive to the metal work functions, which are well-known to be sensitive to adsorbed gases. On the other hand, a striking feature emerges from Fig. 5.41, with regards to CO detection. Another mechanism occurs in the interstitial space between mesostructured carbons to form the carbon-molecule-carbon junction, leading to a hopping mechanism for the intertube charge transfer between mesostructured carbons. The intratube modulation is similar to that of the interaction between semiconductor metal oxides and donor or acceptor molecules, showing a non-linear response and a large sensitivity feature at low concentrations. In terms of CO detection, in this study, the electrical response is attributed to both the inter- and intramodulation of electronic states.

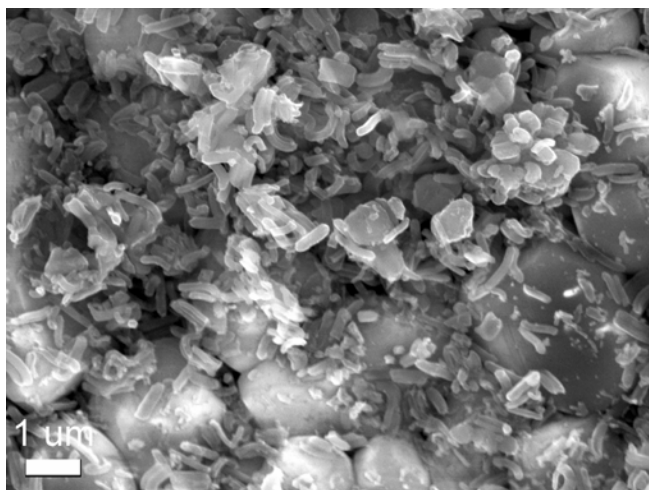


Figure 5.38 SEM images of mesostructured carbon-sensing materials printed on the alumina substrate.

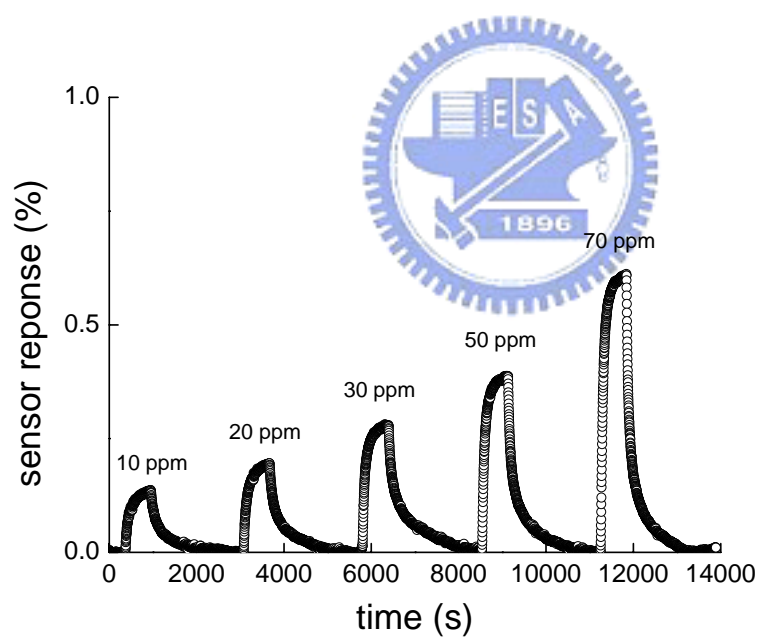


Figure 5.39 Sensor responses of mesostructured cobalt oxide materials to different concentrations of CO in synthetic air.

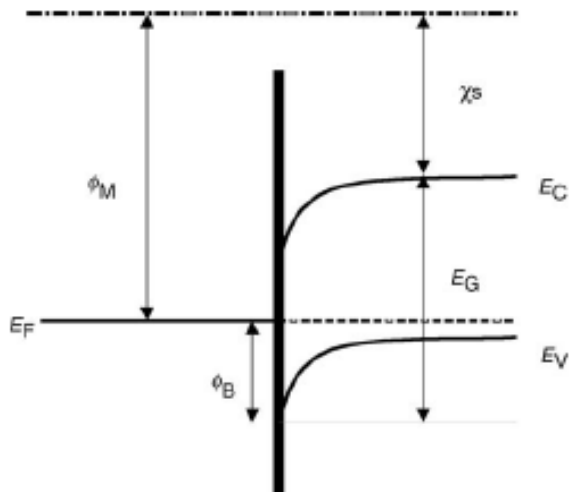


Figure 5.40 Energy-band diagram of the Schottky barrier, forming at the interface of metal and p-type mesostructured carbon. E_F : Fermi level, E_C : conduction band, E_V : valance band.

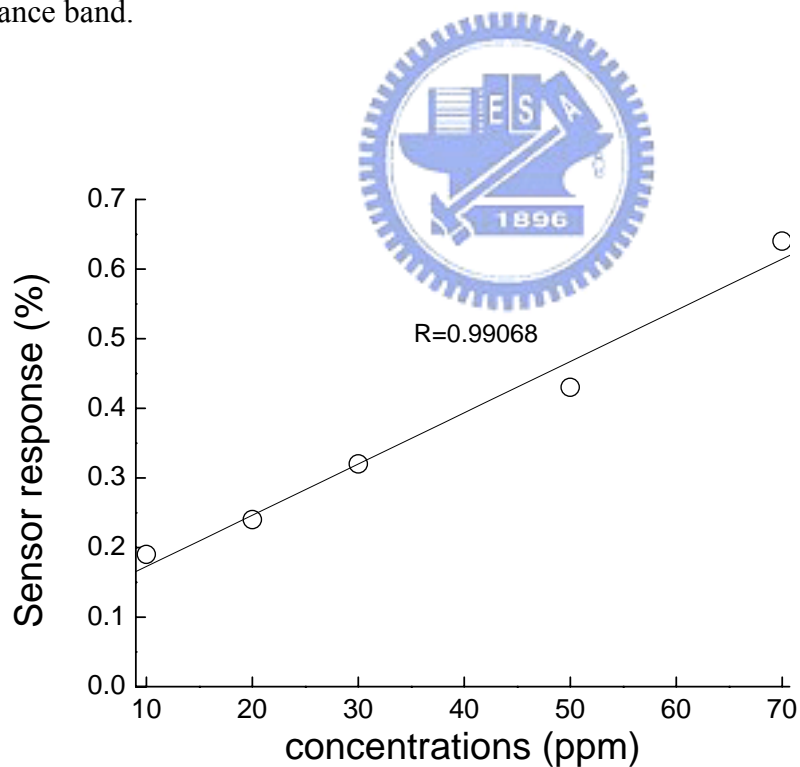


Figure 5.41 Concentration dependence of the mesostructured carbon gas sensor response.

5.4 Mesostructured ZnO materials

The low-angle XRD pattern of porous ZnO is shown in Figure 5.42(a), which also gives the structural order of the mesoporous ZnO. The figure indicates that the sample has a clearly defined diffraction peak located at approximately 1.0° , which can be attributed to the (100) reflections of the hexagonal groups. It also indicates that the sample exhibits a well-ordered structure. Moreover, the cell parameter of mesostructured ZnO is 10.35 nm. The peaks in the wide-angle region (Figure 5.44(b)) are located at 30.9° , 33.4° , 35.2° , 46° , 54.5° , 60.5° , 65.3° , and 66.4° , and correspond to a crystalline ZnO structure. These patterns also indicate the mesostructured ZnO has a [101] preferred orientation; this is consistent with conventional bulk ZnO samples.

The morphology of the mesostructured ZnO was confirmed by SEM (see Figure 5.43), indicating that the mesostructured ZnO particles seemed to be randomly oriented. The ordered structure and the crystallization of porous ZnO were determined by TEM and SAED, as shown in Figure 5.44. The TEM image shows the hexagonal linear pores along the pore axis and nanograins of about 50 nm in size; the SAED pattern, meanwhile, showed diffraction rings, implying that the mesostructured ZnO is a polycrystalline. The HR-TEM also indicated that the d-spacing of porous ZnO was 0.24 nm, which is consistent with the XRD results. The nitrogen sorption isotherm showed that the surface area and pore volume of mesostructured ZnO were $61.3 \text{ m}^2 \text{ g}^{-1}$ and $0.31 \text{ cm}^3 \text{ g}^{-1}$, respectively. The pore-diameter distribution, as determined by the BJH method, showed a pronounced peak at 5.7 nm, confirming a high degree of uniformity among the pores. To acquire more information regarding the structural properties of the mesostructured ZnO, the XPS technique was employed, to detect the composition of the mesostructured ZnO. Figure 5.45(a) shows the XPS O 1s spectra of the mesostructured ZnO. The peak at about 531.5 eV is due to oxygen in

the ZnO; the peak at about 532.8 eV is due to hydroxyl oxygen. The Zn 2p XPS peaks of the mesostructured ZnO are shown in Fig. 5.45(b). The peak is at around 1023.3 eV, corresponding to the zinc ion of ZnO. The XPS results stand as further evidence that the mesostructured ZnO was successfully synthesized.

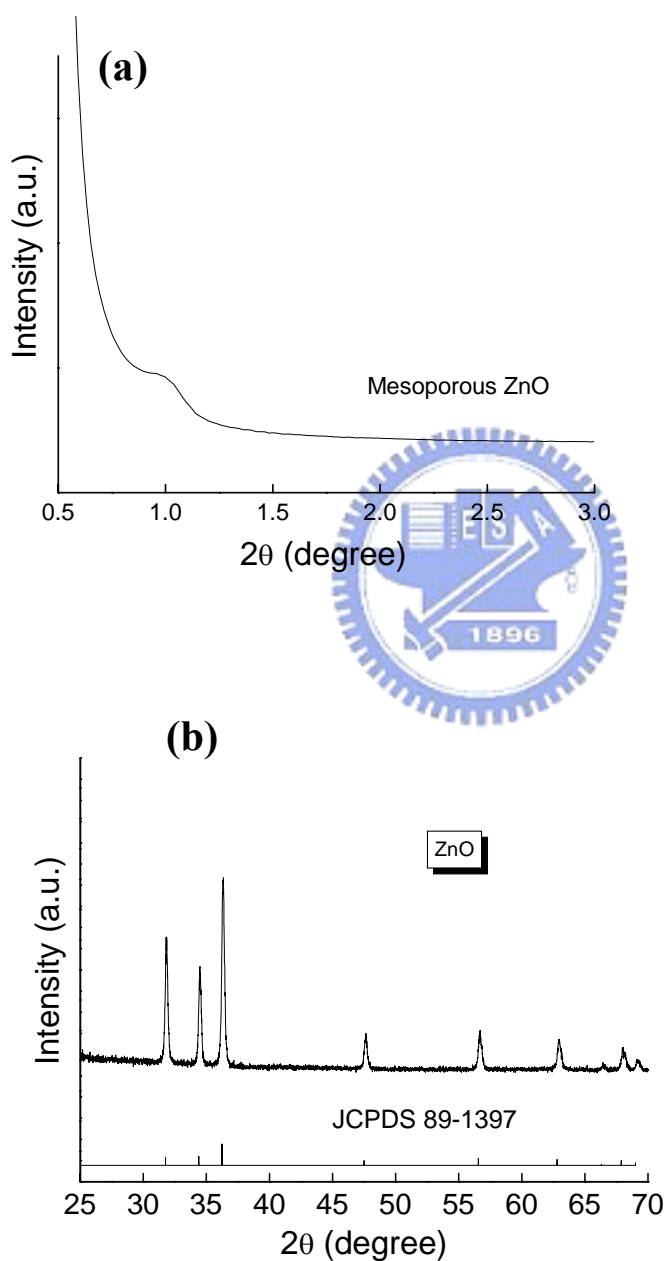


Figure 5.42 (a) Low-angle XRD patterns and (b) wide-angle XRD patterns of mesostructured ZnO.

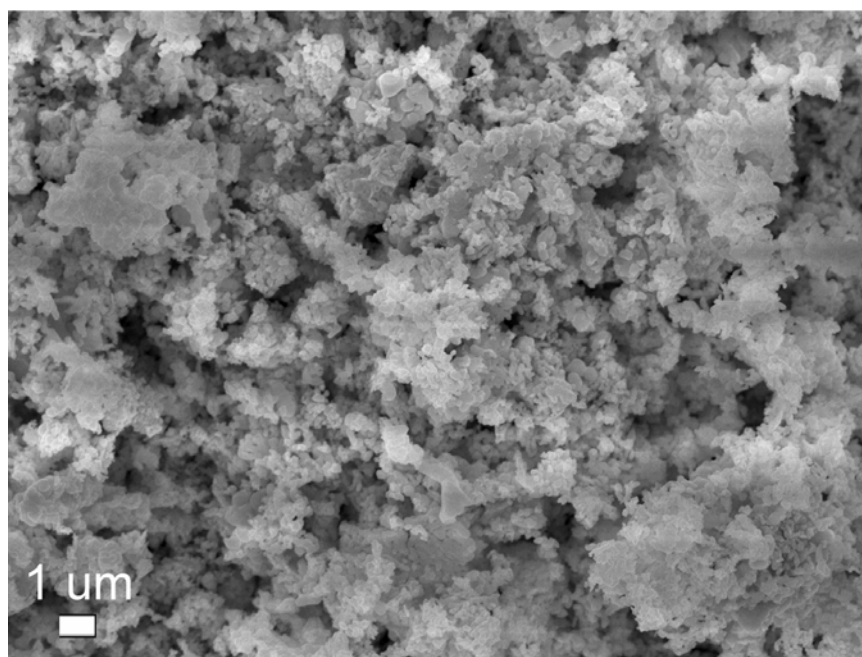
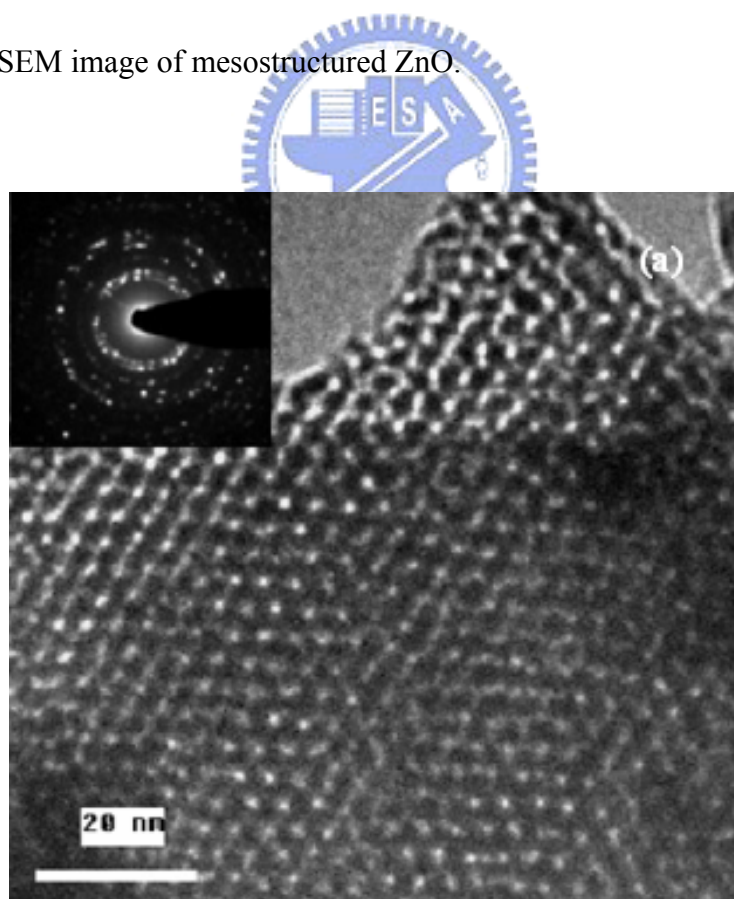


Figure 5.43 SEM image of mesostructured ZnO.



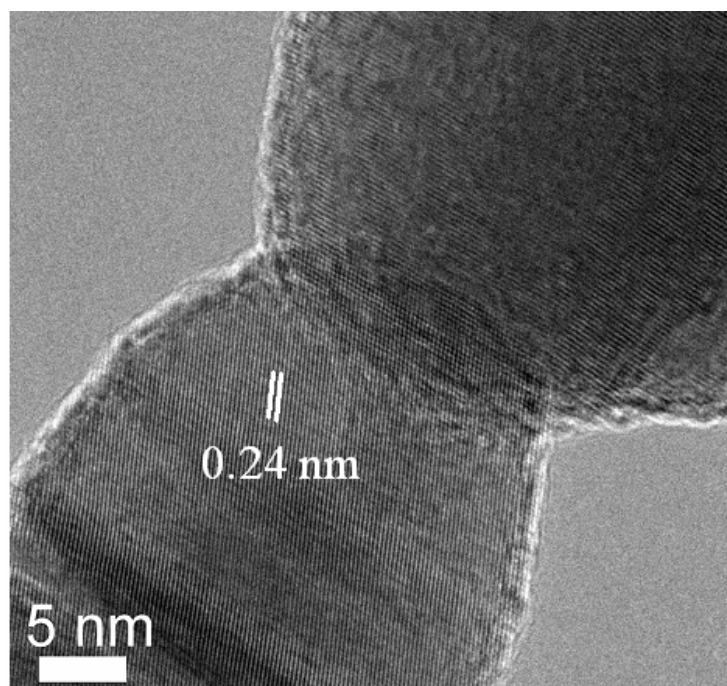
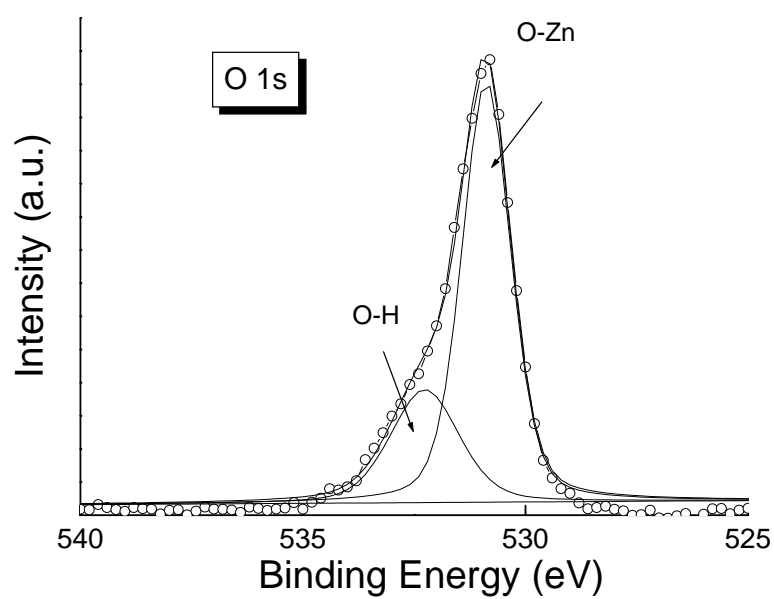


Figure 5.44 (a) TEM image of mesostructured ZnO materials, as a replica of mesostructured carbon template. (b) HRTEM micrograph of the crystalline framework of mesostructured ZnO.



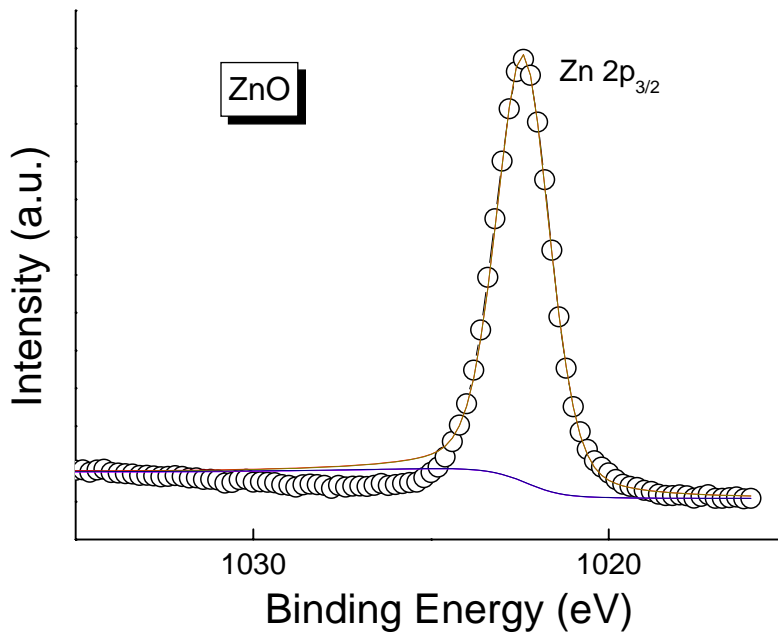
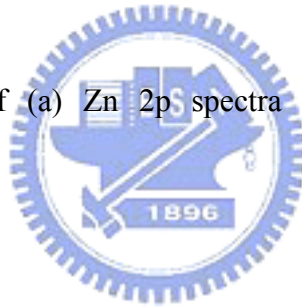


Figure 5.45 XPS spectra of (a) Zn 2p spectra and (b) O 1s spectra of the mesostructured ZnO.



The adsorption of oxygen forms ionic species such as O^{2-} , O_2^- , and O^- , which are adsorbed onto the mesostructured ZnO surface at elevated temperatures. The form of the oxygen ionic species is strongly dependent upon the temperature; in general, O_2^- is predominant at temperatures below 100°C; O^- between 100°C and 300°C; and O^{2-} , above 300°C [116]. The resistance of the mesostructured ZnO sensor decreases upon the introduction of CO gas, because of the exchange of electrons between the ionosorbed oxygen and the mesostructured ZnO sensor [117]. For semiconductor gas sensors, it is known that oxygen sorption plays an important role in electron transport.

The oxygen sorption affects the conductivity of ZnO [118]; therefore, the sensing mechanism of the nano-structured ZnO sensor for CO may be described through reaction kinematics, in the following equations [119];



On the other hand, the reaction between CO gas and the ZnO surface can be described as follows [120]:



Fig. 5.46 shows the effect of the working temperature on the sensitivity of the porous ZnO sensor with regards to CO. It shows that the working temperature plays an important role in the sensitivity of the porous ZnO sensor. The sensor response increases to the a maximum at 250°C, which is the threshold temperature for sensing CO gas. At low temperatures, the CO molecules do not have enough energy to adsorb onto the ZnO surface; on the other hand, the reduction of sensitivity at high temperatures can be attributed to the difficulties inherent in exothermic CO gas adsorption [121].

Fig. 5.47 shows the variation in the response of the ZnO sensor, in relation to its exposure to CO gas injection. It was found that the optimal sensitivity values of the ZnO sensor were 3.8%, 7.5%, 11.5%, 27.6%, and 52% at CO concentrations of 10

ppm, 20 ppm, 30 ppm, 50 ppm, and 70 ppm, respectively. This shows that the porous ZnO gas sensor has a strong response at low CO concentrations. Recently, Malagù et al. demonstrated a sensitivity enhancement that occurred when the grain size of the semiconductive oxide was below 10 nm [122]; they describe a model where the surface acceptor density decreases when the mean grain size is increased for n-type semiconductive oxides. The CO response can be enhanced through a reduction in the surface charge accumulation, which is in turn induced by through a decrease in grain size. Williams and Coles agree with this model [123]. The presence of uniform mesopores in a porous ZnO sensor can also be another important reason behind a strong response to CO gas. The pores in a ZnO sensor can enhance the detection of gas molecules passing through and create more active sites for adsorbing oxygen ions. As shown in Figure 5.49, the response and recovery times of the nano-structured ZnO sensor were found to be 100 s and 110 s, respectively. Those times—and especially the recovery time—are shorter than when other materials are used. These results indicate that the response speed and the stability of the porous ZnO sensor are both sound.

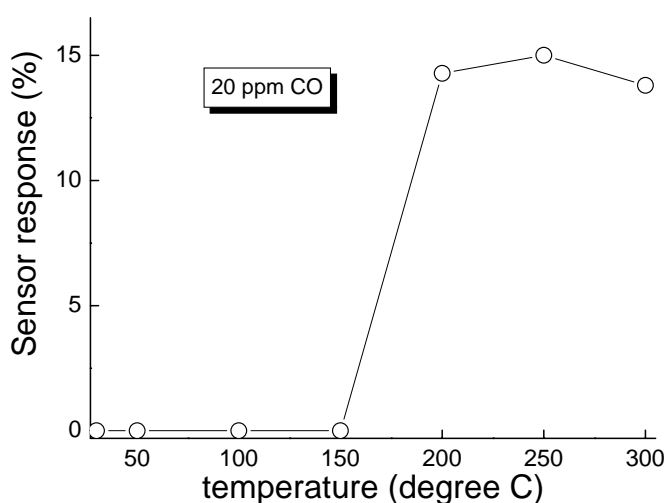


Figure 5.46 Variation of sensing response of mesostructured ZnO sensor with temperature at 20 ppm CO.

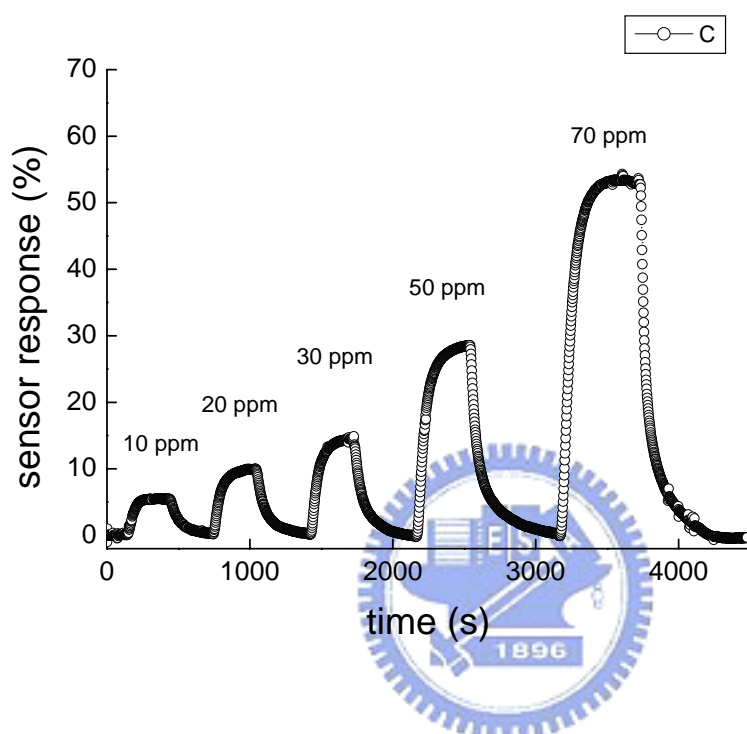


Figure 5.47 Sensing response of mesostructured ZnO sensor determined with several CO concentrations.

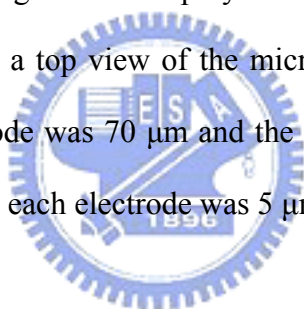
5.5 Mesostructured-based micro sensors

Finding a smart class of micro gas-sensors is a good place to start, when looking for a good gas sensor. Sensors with full complementary metal oxide semiconductor (CMOS) compatibility and microelectro-mechanical system (MEMS) manufacturability have been shown to be superior to others. Clearly, they possess several advantages over previous classes of gas sensors, such as volume production, lower cost; small device volume; low power consumption; increased sensitivity, through the use of circuit on-chips; and self-testing capabilities. Furthermore, some

researchers have been using CMOS-standard processes to create made micro-sensors abroad [124], using integrated circuits and post-processes to create smart gas sensors successfully. Because the parameters are fixed by standard processes, there are many restrictions in chip production. The current study uses MEMS process technology to manufacture the main structure of the new silicon-based structure, and its designing has been developed in accordance with an analysis of experimental data and results.

5.5.1 Overview of the micro-sensor

The basic concept of the micro-sensor is shown in Figure 5.48. The sensor features a thin membrane of a micro-hotplate structure, including films of silicon dioxide and silicon nitride, together with poly-silicon or metal micro-heaters and electrodes. Figure 5.49 shows a top view of the micro-sensor device. It can be seen that the distance of the electrode was 70 μm and the length of the electrode was 600 μm . The gap-distance between each electrode was 5 μm .



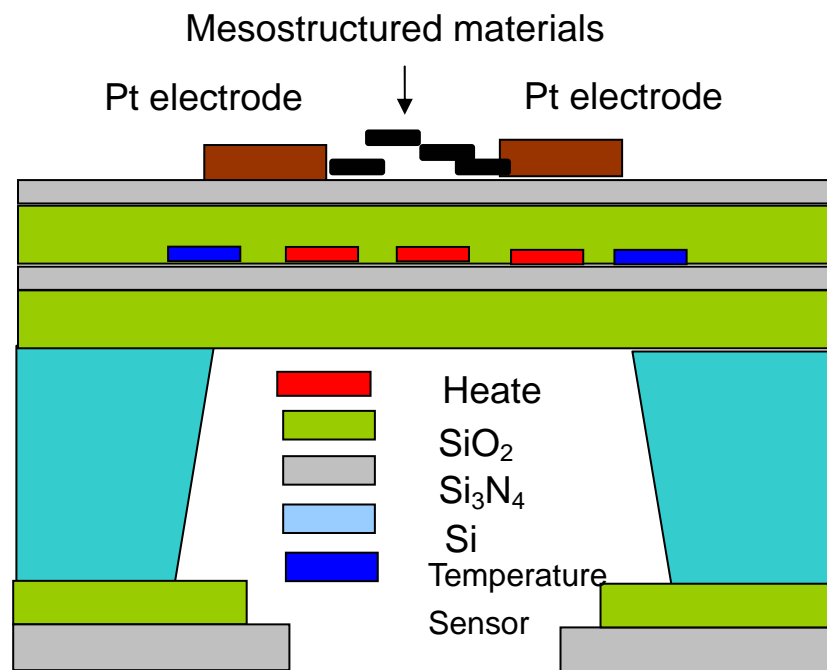


Figure 5.48 Schematic design of a micro-sensor device with the micro-hotplate membrane.

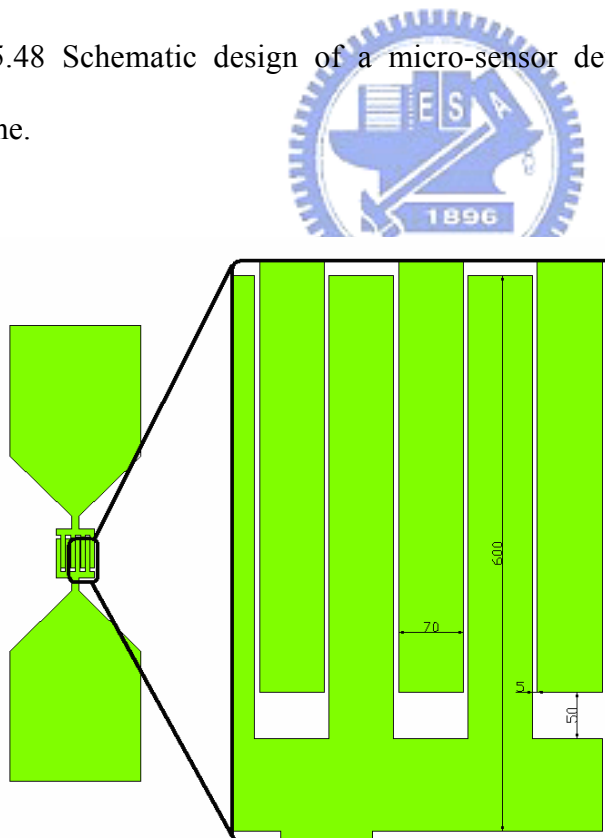


Figure 5.49 Top-view diagram of micro-sensor electrode.

DEP is an electro-kinetic phenomenon that occurs when a particle is placed in a non-uniform electric field, thus inducing the particle to form an electric dipole. Because the electric field is non-uniform, it is stronger on one side of the dipole than the other. The result is a net force on the particle, causing it to move. The DEP process provides an effective way of manipulating bio-particles, automatically and quickly enhancing the preparation of biological samples.

5.5.2 Gas-sensing for DEP-trapped mesostructured materials

SEM images of the DEP-trapped mesostructured cobalt oxide trapped on the microelectrode are shown in Figure 5.50. Since the cobalt oxides particles were longer than the electrode gap, the trapped tubes bridged the gap. The captured cobalt oxides formed a massive agglomeration. The SEM image also revealed that the DEP-trapped cobalt oxide could be firmly immobilized on the microelectrode. The highly magnified SEM (Figure 5.50(b)) image shows that the mesostructured cobalt oxide was randomly oriented, with a 530-nm length and a 110-nm diameter.

To investigate gas response, a set of gas measurements were carried out. In these experiments, the sensor's operation temperature was recorded at 200°C, which had been determined to be the optimal working temperature. Relative humidity was 50% given at an ambient temperature of 23°C. The sensors were constantly purged by synthetic air, interrupted only by trace gases that had been diluted in synthetic air. The dynamic sensor response of the mesostructured cobalt oxide gas sensor at a temperature of 200°C is shown in Figure 5.51. On the basis of the definition provided, the sensor responses were 8.9%, 11.6%, 13.2%, 16.1%, and 18.5% for concentrations of 10 ppm, 20 ppm, 30 ppm, 50 ppm, and 70 ppm, respectively. This observed temperature-dependent gas-sensing behavior accords with the reported characteristics of the thick-film material [125, 126].

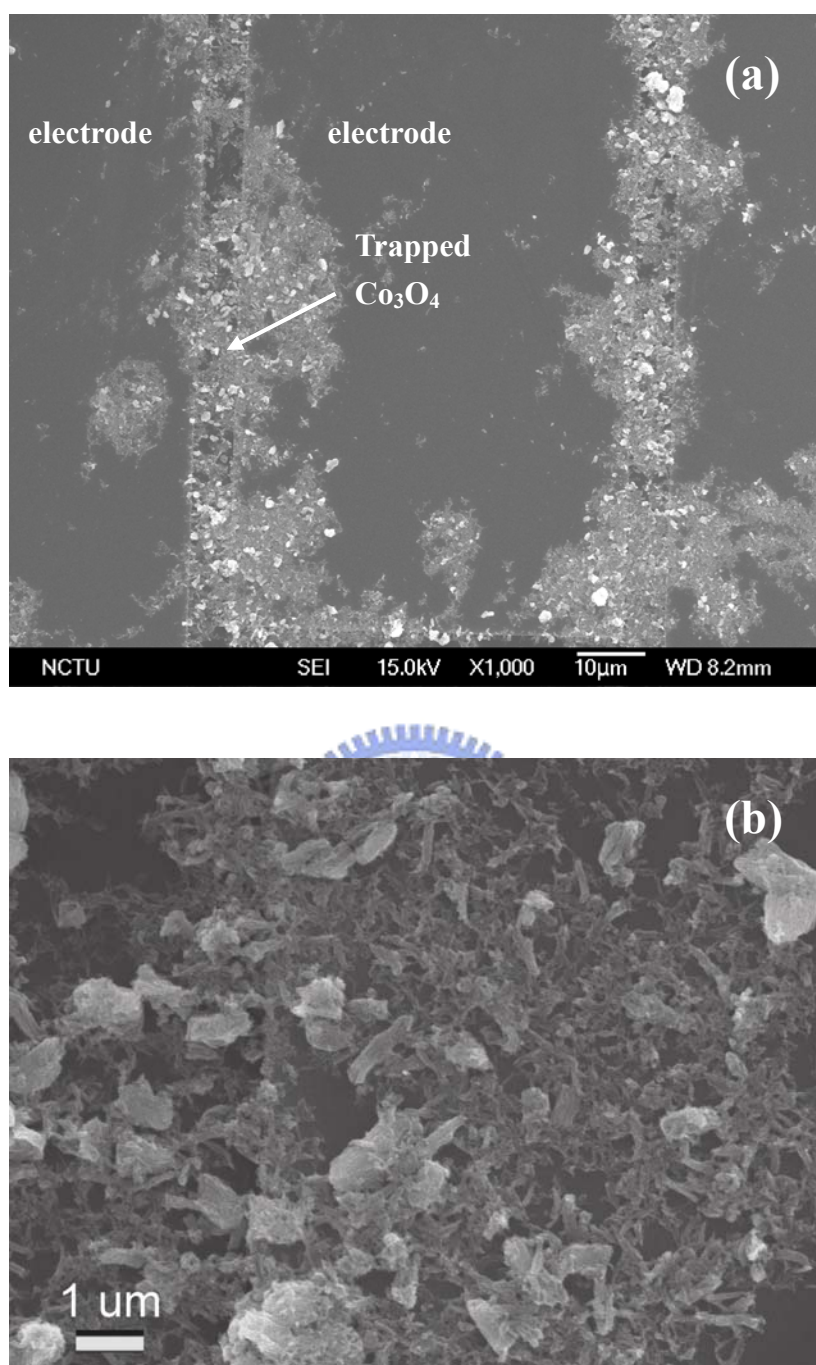


Figure 5.50 (a) Low-magnification SEM images and (b) high-magnification SEM images of DEP-trapped mesostructured cobalt oxide.

Figure 5.52 shows the repeatability test of the cobalt oxide materials at a CO concentration of 50 ppm. The tests were performed by measuring the changes in resistance at different CO concentrations (i.e., 10–70 ppm). Those changes showed that the response increased while the CO gas was being injected, but then decreased to baseline once the gas was turned off. It was also seen that these materials exhibited good repeatability during the testing. The direction of responses to CO indicated a typical p-type semiconductor behavior; moreover, the sensor response was linearly proportional to the CO concentration, at least down to 10 ppm (Figure 5.53). This indicates that the sensor could have a prompt response at low CO concentrations.

The average response and recovery times were 115 s and 211 s, respectively. J. Wöllenstein et al. reported on the non-porous cobalt oxide exposed to 50 ppm CO, where the response time was lower than 5 min and the recovery time was approximately 30 min [127]. Obviously, the mesostructured cobalt oxide exhibited much higher sensitivity and much prompter responses than the non-porous cobalt oxide thin-film sensor. Changes in sensor response were mainly caused by the adsorption and desorption of gas molecules on the surface of the sensing material. In general, for sensing materials, only a thin layer of film close to the surface can be activated during gas detection because of the dense structure of compact films. In contrast, the porous surface of cobalt oxide materials can provide more active sites, yielding more surface area that the gas molecules can activate. In this way, the gas sensitivity and response time of mesostructured cobalt oxide are remarkably enhanced.

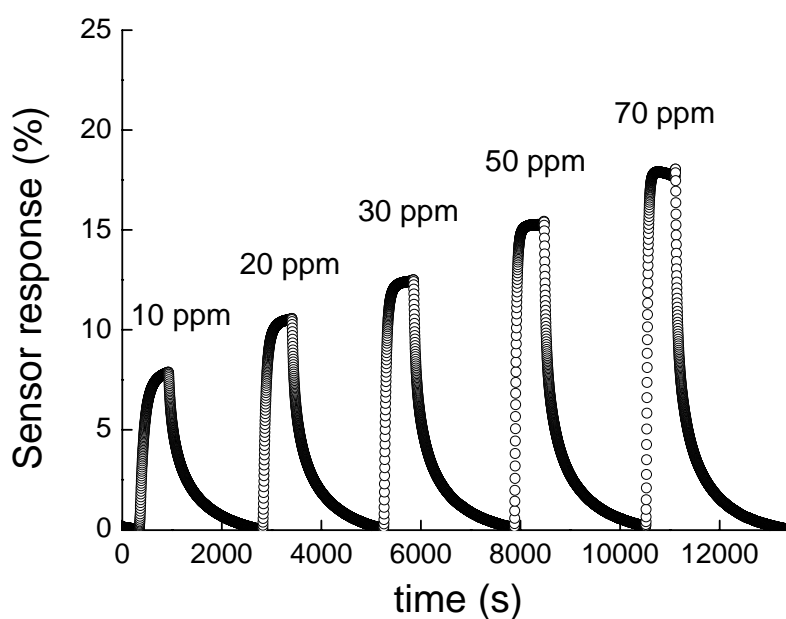


Figure 5.51 Dynamic sensor response of DEP-trapped mesostructured cobalt oxide sensor, measured with various CO concentrations.

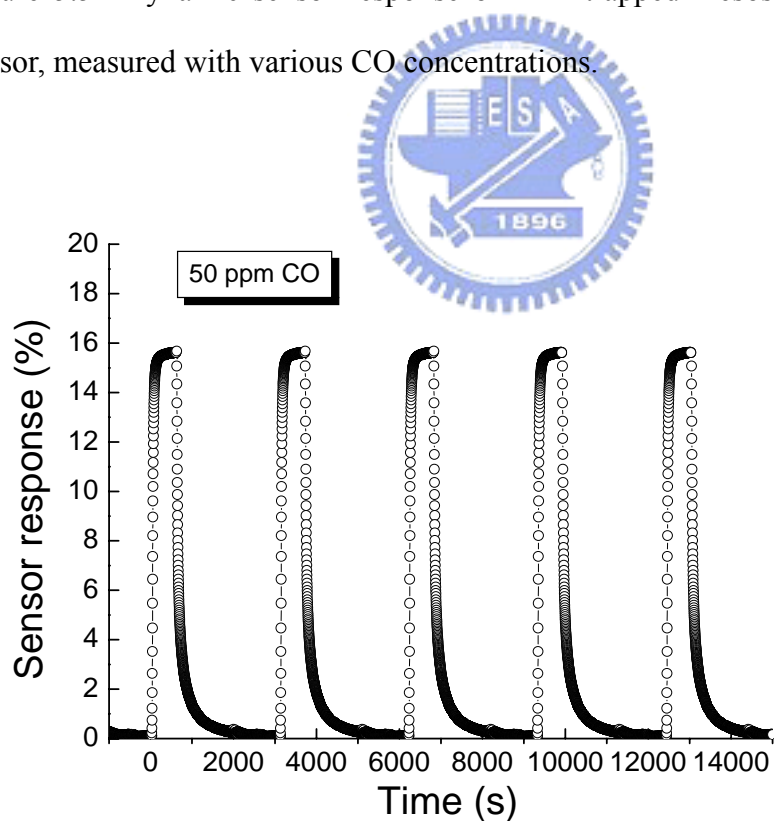


Figure 5.52 Repeatability test of the DEP-trapped mesostructured cobalt oxide exposed to 50 ppm CO.

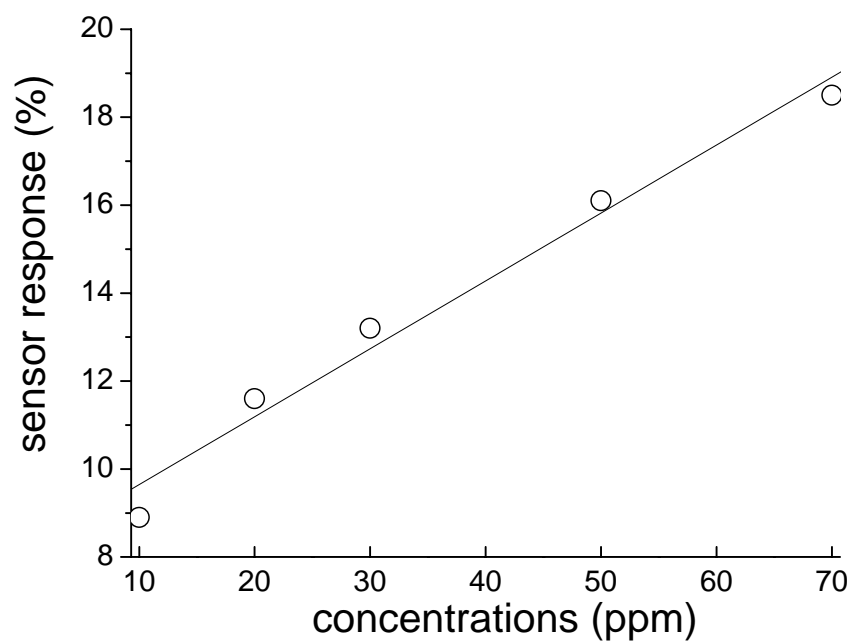


Figure 5.53 Linear sensor response of the DEP-trapped mesostructured cobalt oxide at various CO concentrations.



On the other hand, we used the aforementioned electrode to immobilize other sensing materials such as mesostructured ZnO and mesostructured cobalt oxide. Unfortunately, the electrode is not suitable for these materials, due to the device resistance of the electrode and the shape of the sensing materials. Resistance is disturbed by the surface tension, and it is difficult to control factors that contribute to sharp type; therefore, we attempted to design a new device for sending mesostructured materials. The new device for mesostructured ZnO and cobalt oxide is compiled in Table 5.1, and the morphology of the DEP-trapped mesostructured ZnO is confirmed by SEM in Figure 5.54. The image also indicates that the mesostructured ZnO particles were arranged along the electrode. The highly magnified images show that the mesostructured ZnO particles seem to be randomly oriented. This random orientation provides electrical paths among neighboring extrusions, and when these randomly oriented mesostructured ZnO particles are in spacer regions, the two electrodes are no longer electrically open.

The operating temperature of the mesostructured ZnO was fixed at 250°C. Since CO is an electron-donating gas, the mesoporous ZnO sensor behaves like an n-type semiconductor, due to the decreasing resistance of mesostructured ZnO. Figure 5.55(b) shows the variation in sensitivity of the ZnO sensor, in relation to its exposure to CO gas injection. It was found that the optimal sensitivities of the ZnO sensor were 12.1%, 14.6%, 18.4%, 26.0%, and 60% at CO concentrations of 10 ppm, 20 ppm, 30 ppm, 50 ppm, and 70 ppm, respectively. This indicates that the porous ZnO gas sensor has a strong response at low CO concentrations. Figure 5.55(b) shows the typical response changes of the mesostructured ZnO materials to a 20-ppm concentration of CO gas. The tests were performed by measuring the changes in resistance at different CO concentrations (i.e., 10–70 ppm).

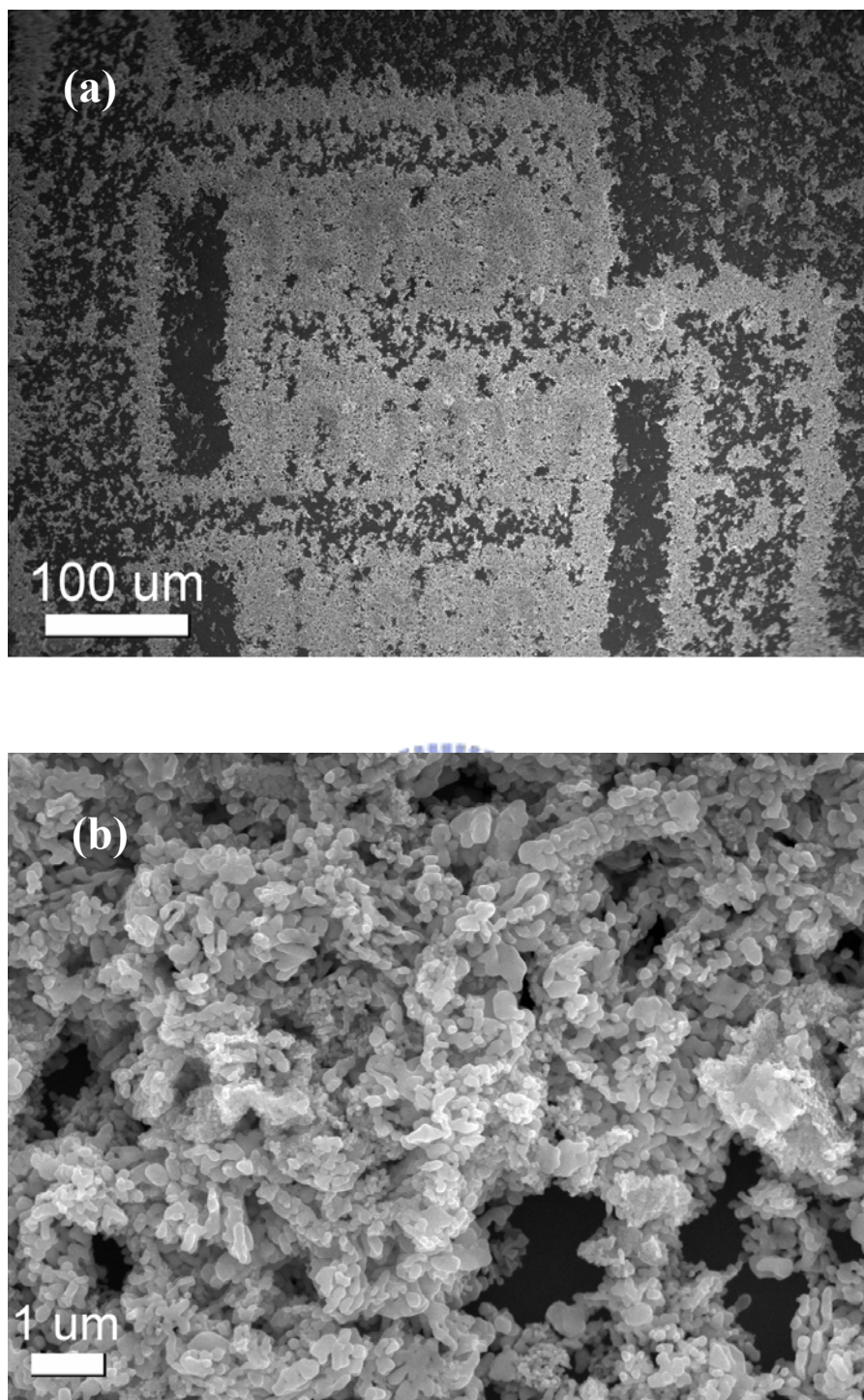


Figure 5.54 (a) Low-magnification SEM images and (b) high-magnification SEM images of DEP-trapped mesostructured ZnO.

It also showed that the resistance decreased while the CO gas was being injected, but that it increased to baseline once the gas was turned off. These materials also exhibited good repeatability during testing. As shown in Figure 5.55(a), the response and recovery times of the nano-structured ZnO sensor were found to be 80 s and 90 s, respectively, and these times—especially the latter—were shorter than when other materials were used. These results indicate that the response speed and stability of the porous ZnO sensor are both sound. Recently, Malagù et al. demonstrated a sensitivity enhancement that occurred when the grain size of the semiconductive oxide was below 10 nm [128]; they describe a model where the surface acceptor density decreases when the mean grain size is increased for n-type semiconductive oxides. The CO response can be enhanced through a reduction in the surface charge accumulation, which is in turn induced through by a decrease in grain size. Williams and Coles agree with this model [129]. The presence of uniform mesopores in a porous ZnO sensor can also be another important reason behind a strong response to CO gas. The pores in a ZnO sensor can enhance the detection of gas molecules passing through and create more active sites for adsorbing oxygen ions.

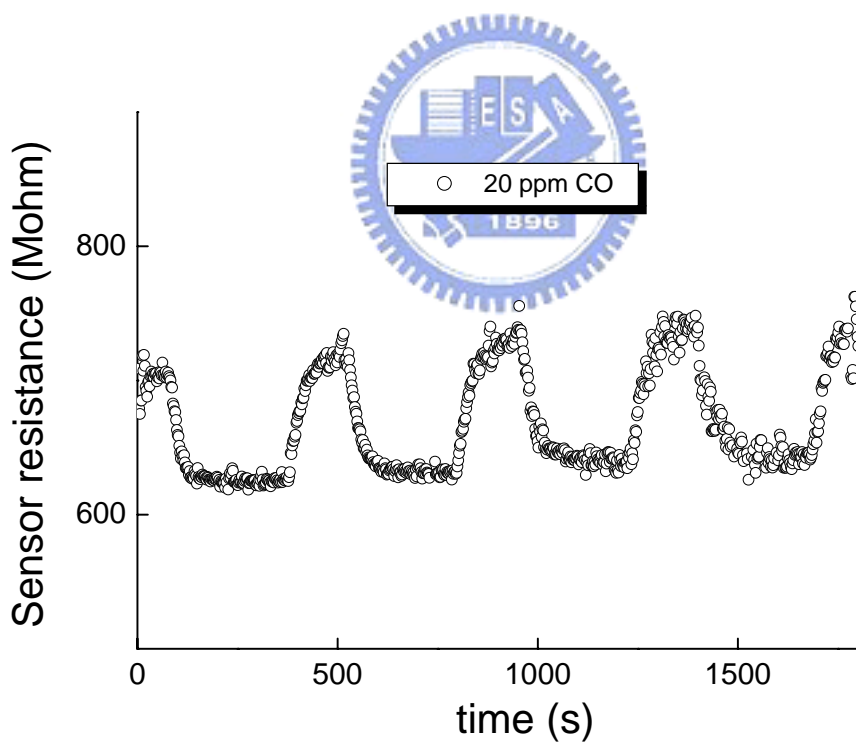
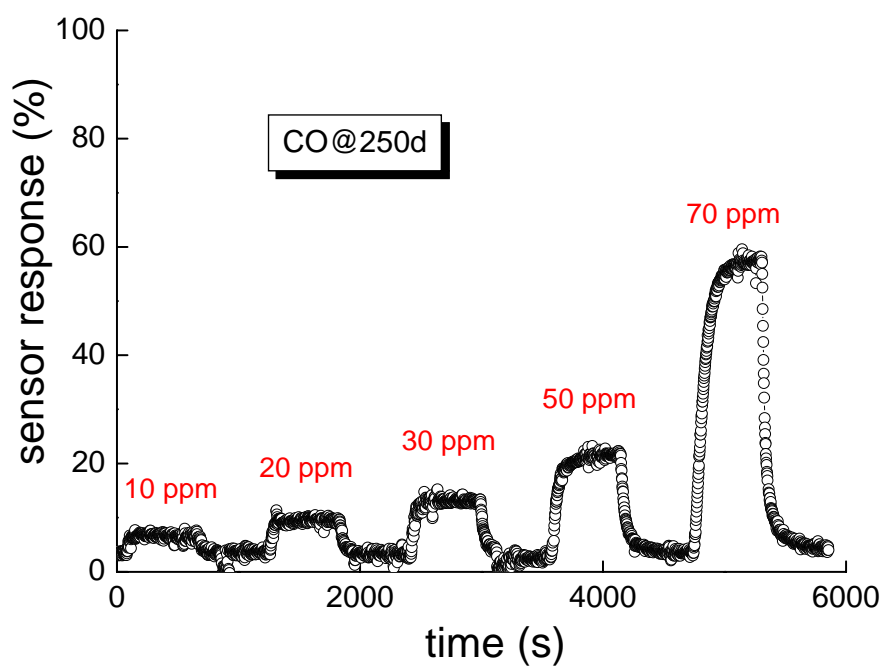


Figure 5.55 (a) Switching response of the mesostructured ZnO sensor exposed to 30-ppm CO gas and (b) sensing response of mesostructured ZnO sensor determined with several CO concentrations.

Table 5.1 The device specification for mesostructured materials.

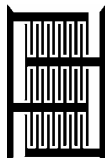
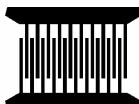

Categories of Material	Shape of Electrodes	Gap of Electrodes(μm)	Resistance ($\text{M}\Omega$)
Carbon (1000 nm)		25	80 ~136
ZnO (350nm)		20	120~200
Co ₃ O ₄ (700nm)		5	20~80

Figure 5.56 shows the DEP-trapped mesostructured carbon-sensing materials. The DEP-trapped mesostructured carbon was successfully immobilized along the electrode. The highly magnified SEM image shows that the mesostructured carbon still maintained a rod structure, with a diameter of approximately 400 nm and a length of approximately 1 μm . Figure 5.57(a) plots the switching response of the mesoporous carbon exposed to a 50-ppm CO gas injection, while Figure 5.57(b) shows a typical response curve to CO gas at 30-ppm concentrations and at optimal temperature. In the Figure 5.57(a), it is shown that resistance increased while the CO gas was being injected and then decreased to baseline once the gas was turned off. It was also seen that these materials exhibited good repeatability during the testing. The response and recovery times of the mesoporous carbon sensor were around 170 s and 250 s, respectively. As shown in Figure 5.57(b), the sensor resistance increased with an increase in ambient CO gas concentration. The optimal sensitivities of this sensor were 2.9%, 4.3%, 6.6%, 9.2%, and 36.3% for concentrations of 30 ppm, 45 ppm, 60

ppm, 75 ppm, and 90 ppm, respectively. Additionally, an abrupt condition was observed at a 90-ppm concentration of CO. To the best of the author's knowledge, only the research group of Prof. N.D. Chien has tracked these phenomena; however, they did not describe this abrupt condition [130].

It is widely accepted that the mechanism of gas diffusion through a porous material depends on the Knudsen diffusion [131]. Thus, we assume the Knudsen diffusion to be applicable to our sensors. The gas concentration inside a film decreases with an increase in diffusion depth, due to the surface reaction. The penetration depth of the gas molecules becomes small; this is a well-known non-saturated condition. In this way, the abrupt condition was found. Since CO is an electron-donating gas, the mesoporous carbon sensor behaves like a p-type semiconductor, due to the increasing resistance of mesoporous carbon. The response behavior of this sensor was similar to that of carbon nanotubes [132]. In general, an increase in the active surface area of the sensing material enhances the properties of materials used as gas sensors. The surface area of mesostructured carbon is $1200 \text{ m}^2 \text{ g}^{-1}$, which can provide a more active site for adsorbing oxygen species.

The properties of CO were determined using a CNT-based sensor at various CO concentrations. Huh et al. indicate the behavior of single-wall CNT-based gas sensor at various conditions of operation. The response of a SWNT-based sensor to a 5-ppm CO exposure is 8%, but the sensor response time approached 10 min. The recovery of the sensor, however, was quite slow and incomplete, due to the residual CO molecules that had been adsorbed on the SWNT bundles had not been entirely removed. It was also seen that these materials, when exposed to NH_3 , exposure exhibit poor repeatability during testing. On the other hand, Dutta et al. show that MWCNTs are a potential material for carbon monoxide sensing; however, this material is non-responsive to CO at 100°C . At 200°C , the sensitivity was 0.2% to 250 ppm CO,

and the required response time was 5 min. For CNT-based sensing materials, the resistance changed while the tested gas was being injected, but reverted to baseline once the gas was turned off. It was also seen that these materials exhibit good repeatability during testing [133, 134]; this is hardly acceptable in the case of CNT-based sensors.

The response and recovery times of the sensor are determined by adsorption kinetics. The bonding between the gas and sensor is very strong; a prompt response can be explained by the changes in the Schottky junction formed between mesoporous carbon and electrodes [135]. The electron transfer in the porous system, via the lowering of the forward bias-induced barrier, may enhance the gas-reaction response. The longer recovery time became longer than the response time, because of the residual gas molecules that had been adsorbed on the mesoporous carbon bundles and not entirely removed. The higher sensitivity was attributed to the small pore size and their 1D microstructure. By increasing the number of transferred electrons in porous material systems, more electrons might be captured by CO molecules, resulting in the need for a longer recovery time. These results indicate that both the response and stability of the mesoporous carbon sensor are sound.

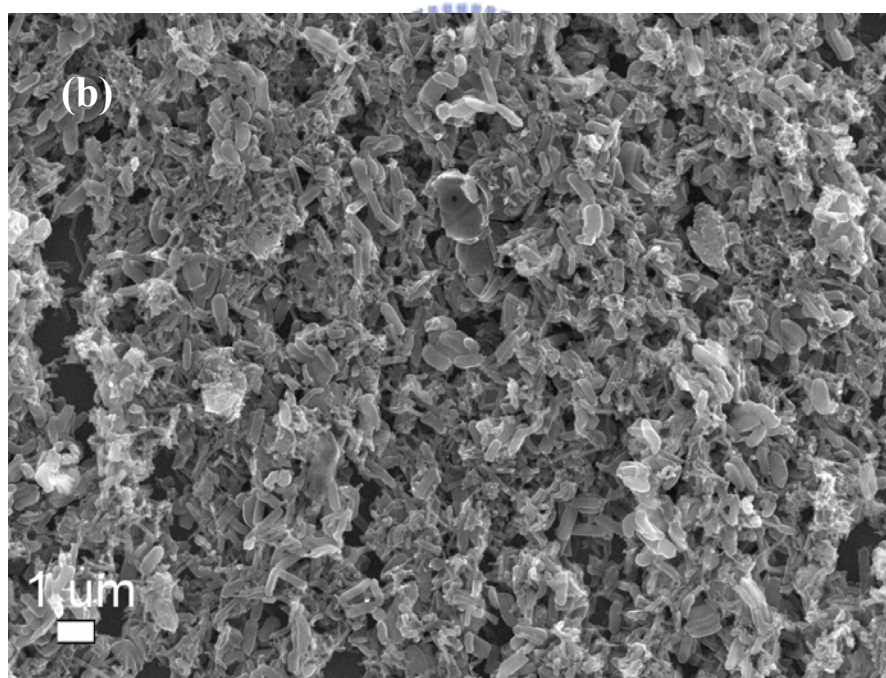
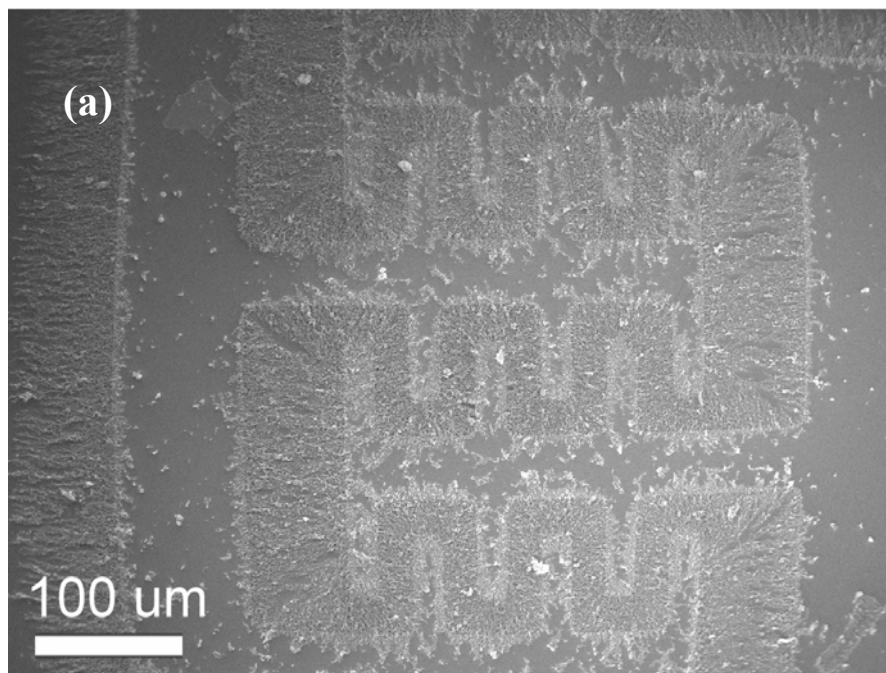


Figure 5.56 The SEM images of (a) low magnification and (b) high magnification of the DEP-trapped mesostructured carbon.

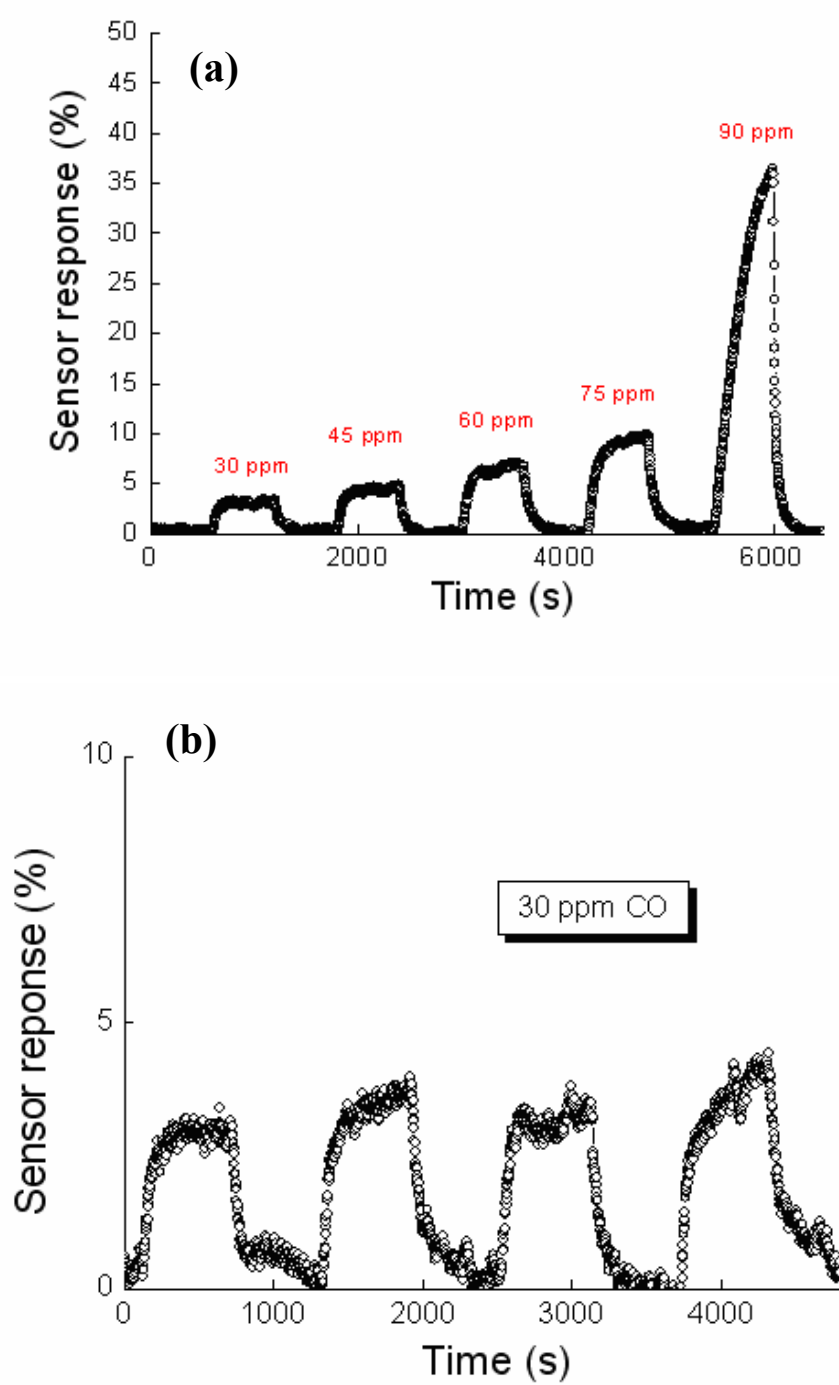


Figure 5.57 (a) Response of the mesostructured carbon sensor measured with various CO concentrations and (b) switching response of the mesostructured carbon sensor exposed to 30-ppm CO gas.

5.6 Tunable interconnectivity of mesostructured materials on sensing performance

Different crystallization temperature samples were used, to understand the influence of the interconnectivity of the mesostructured materials *vis-à-vis* sensing performance. Figure 5.58 shows the sensor response of mesostructured materials at different crystallization temperatures. It was found that sensor resistance increases with CO concentrations, regardless of crystallization temperature. The initial sensor resistance, at a crystallization temperature of 100°C, was lower than that at 40°C crystallization temperature. The sensor responses of the mesostructured materials at different crystallization temperatures are shown in Fig. 5.59. It is noticeable, that the results show systematic changes in sensor response as gas concentration decreases. More importantly, the results clearly show that mesostructured sensors at higher crystallization temperatures have a much greater sensitivity response to certain reductions in gas concentration. It is interesting to note that the surface areas of the 100°C crystallization temperature sample was higher than that of the 40°C crystallization temperature sample. Based on this condition, it was discovered that the sensitivity of the mesostructured sensor to CO could, in fact, be substantially improved. It is interesting to find that higher sensitivities were observed among sensors possessing higher interconnectivity; this phenomenon is not surprising, as it is well-known that surface oxygen anions—such as O^- or O^{2-} —that adsorbed on p-type semiconductor oxide surfaces act as surface donors, donating electrons and diminishing the surface conductivity.

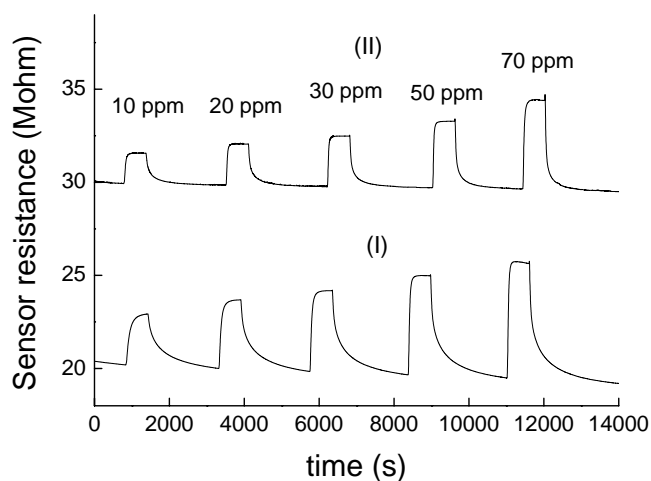


Figure 5.58 Sensor resistance of mesostructured sensors at different crystallization temperatures: (I) 40°C and (II) 100°C.

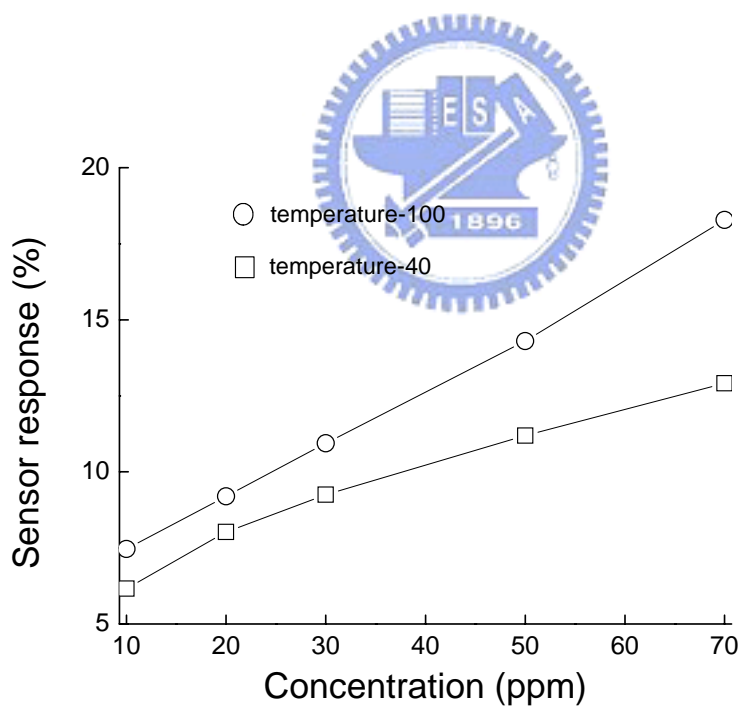


Figure 5.59 Relationship between the sensitivity of mesostructured sensors at different crystallization temperatures.

Thus, the higher interconnectivity of mesostructured sensor means a greater number of surface adsorption sites or surface oxygen anions available to react with reducing gases, thus inducing larger resistive changes in the semiconductor oxide sensor. In mesoporous materials, the mean free path of a gas molecule is determined by the pore walls rather than by adjacent molecules; a molecule, after all, is more likely to collide with the pore wall than with other gas molecules. Transport is described by the Knudsen diffusion and the diffusion coefficient D_k is proportional to the pore radius r , as shown in equation (13), where R is the universal gas constant and M is the molecular weight of the gas molecule.

$$D_k = 4r/3 (2RT/IM)^{1/2} \quad (13)$$

For larger pores, gas transport occurs mainly by molecular diffusion, whereas in smaller pores, surface diffusion becomes predominant [110, 111]. Surface diffusion will also have a more significant contribution in smaller pores. Gas diffusion is generally slower with smaller pores, as evident from equation (13) for Knudsen diffusion. Apart from the pore-size dependence of Knudsen diffusivity, the contribution of surface diffusion will become more and more significant with small mesopores, as the pore widths lie substantially below the mean free path of a gas molecule. Diffusion in loose interconnectivity will therefore be rate-determining, *vis-à-vis* overall diffusivity. This situation was observed by Korotcenkov et al., who prepared SnO₂ thin films by ionic layer deposition and obtained a crystalline size of approximately 6–7 nm; they found agglomerates with sizes similar to the films' thicknesses [133, 134].

5.7 The new mechanism of mesostructured-based sensors

The pore channels connect with each other, as shown in Figure 5.60. The gas can access the film throughout these pore-channel connections. Consequently, in terms of gas accessibility, mesostructured carbon is better than other sensing materials that lack without pore-channel connections for gas accessibility. These materials are sensitive to CO gas and exhibit excellent sensing performances, depending on the accessibility of the mesostructure to the gas. Mesoporous carbon could contribute to chemical reactions at the surface, resulting in high sensitivity at optimal operating temperatures. Porous sensors have the excellent sensitivity than non-porous sensors. The mechanisms were depicted below. In general, for the mesostructured materials, the pore channels connect with each other, as shown in Figure 5.60. The gas can access the film throughout these pore-channel connections. Consequently, in terms of gas accessibility, mesostructured materials are better than other sensing materials that lack without pore-channel connections for gas accessibility. These materials are sensitive to CO gas and exhibit excellent sensing performances, depending on the accessibility of the mesostructure to the gas. Mesoporous materials could contribute to chemical reactions at the surface, resulting in high sensitivity at optimal operating temperatures.

The properties of CO were determined using a CNT-based sensor at various CO concentrations. Huh et al. indicate the behavior of single-wall CNT-based gas sensor at various conditions of operation. The response of a SWNT-based sensor to a 5-ppm CO exposure is 8%, but the sensor response time approached 10 min. The recovery of the sensor, however, was quite slow and incomplete; due to the residual CO molecules that had been adsorbed on the SWNT bundles had not been entirely removed. It was also seen that these materials, when exposed to NH_3 , exposure exhibit poor repeatability during testing. On the other hand, Dutta et al. show that MWCNTs are a potential material for carbon monoxide sensing; however, this material is

non-responsive to CO at 100°C. At 200°C, the sensitivity was 0.2% to 250 ppm CO, and the required response time was 5 min. For CNT-based sensing materials, the resistance changed while the tested gas was being injected, but reverted to baseline once the gas was turned off. It was also seen that these materials exhibit good repeatability during testing [133, 134]; this is hardly acceptable in the case of CNT-based sensors.

The response and recovery times of the sensor are determined by adsorption kinetics. The bonding between the gas and sensor is very strong; a prompt response can be explained by the changes in the Schottky junction formed between mesoporous carbon and electrodes [137]. The electron transfer in the porous system, via the lowering of the forward bias-induced barrier, may enhance the gas-reaction response. The longer recovery time became longer than the response time, because of the residual gas molecules that had been adsorbed on the mesoporous carbon bundles and not entirely removed. The higher sensitivity was attributed to the small pore size and their 1D microstructure. By increasing the number of transferred electrons in porous material systems, more electrons might be captured by CO molecules, resulting in the need for a longer recovery time. These results indicate that both the response and stability of the mesoporous material sensors are sound.

Additionally, mesoporous materials also show fewer grain boundaries that could offer additional sensing area for gas adsorption. This topology favors fast electrical charge transduction through the material, which could explain the short response time observed. By increasing the number of transferred electrons in porous material systems, more electrons might be captured by CO molecules, thereby necessitating a longer recovery time. These results indicate that both the response and stability of the mesoporous materials sensor are good. Moreover, the presence of a nanosized mesostructured materials film can be another important reason for the CO response.

Gas sensing of semiconducting metal oxides is caused by the dependence of the barrier on the environment work function [138]. We deduced that the dependence of barrier height on environment work function increased as the surface charge density decreased. Therefore, the CO response could be enhanced with a reduction in the surface charge accumulation induced by the decrease in grain size. Williams and Coles have agreed with this model [129].

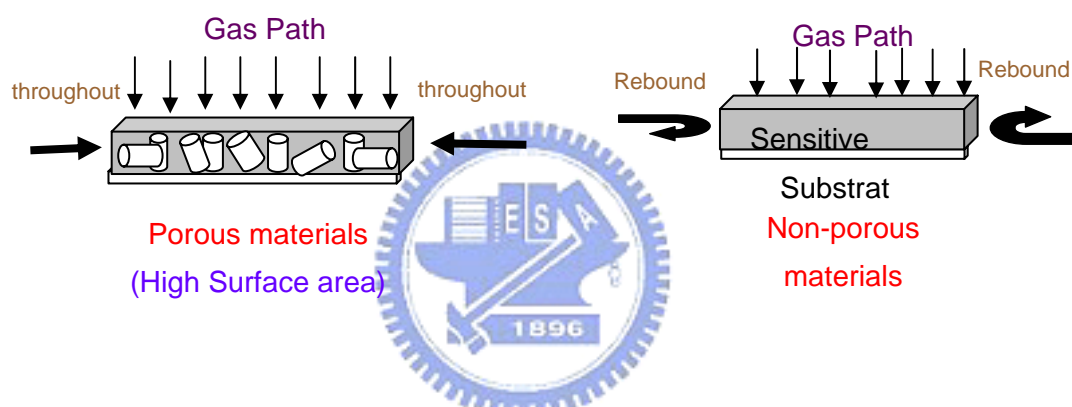


Figure 5.60 Diagram showing gas accessibility in mesostructured materials.

Chapter 6 Conclusions

The structural, textural, and gas-sensing properties of mesostructured materials are summarized as follows.

1. Mesostructured cobalt oxide materials synthesized from SBA-15 template have a specific architecture, high surface areas, and larger pore size, but also show excellent gas-sensing performance for low concentrations of CO. DTA/TGA revealed that the composites have four inflection points, indicating the release of water at different temperatures between 80°C and 210°C. The structural properties showed that cobalt oxide was a single crystalline and that its highly ordered structure remained. On the other hand, mesostructured cobalt oxide synthesized at lower crystallization templates (i.e., 40°C and 60°C), showing separated nanorods lacking a highly ordered structure. The morphologies of the mesostructured cobalt oxide seemed to be aggregated. The optimal response are 4.3%, 6.0%, 7.4%, 9.7%, and 13% for CO concentrations of 10 ppm, 20 ppm, 30 ppm, 50 ppm, and 70 ppm, respectively. Additionally, it is interesting to note that the sensor response of mesostructured cobalt oxide material was seemingly affected by an aggregated morphology.
2. For mesostructured carbon materials, the well-resolved reflections were appeared at the carbonization temperatures above 700°C, indicating an enhanced structural ordering. However, the cell parameter of the mesostructured carbon was tuned along with an increase in carbonization temperatures, due to structural shrinkage. After the carbonization process, samples synthesized at lower crystallization temperatures (i.e., 40°C and 60°C) exhibited a rhombus morphology, whereas

samples at higher crystallization temperatures (100°C) had a rod morphology. On the other hand, a highly ordered structure was not observed at the lower crystallization temperatures, due to the smaller pore size. Although the mesostructured carbon had a larger surface area ($\sim 1200 \text{ m}^2 \text{ g}^{-1}$). The sensing performances were 0.1%, 0.2%, 0.3%, 0.4%, and 0.6% for concentrations of 10 ppm, 25 ppm, 30 ppm, 50 ppm, and 70 ppm. This material also had the longer response and recovery times—about 6 min and 60 min, respectively. After being screen-printed on alumina substrate, the aggregated morphology would block the pore channel, obstructing gas molecules from passing easily. For this reason, the sensing performance of the mesostructured carbon is relatively poor.

3. The mesostructured ZnO materials synthesized from the mesostructured carbon template shows a (101) preferred orientation. The mesostructured ZnO particles seem to be randomly oriented and the highly ordered nanograins of mesostructured ZnO are about 50 nm in size; the SAED pattern also shows the diffraction rings, implying that the mesostructured ZnO is a polycrystalline. Moreover, the optimal sensitivity of the mesostructured ZnO reached 52% at CO concentrations of 70 ppm, although the surface area ($61.3 \text{ m}^2 \text{ g}^{-1}$) was smaller than those of other mesostructured materials. The mesostructured ZnO materials also had faster response and recovery times of 100 s and 110 s, respectively.
4. To summarize the aforementioned results (i.e., 1-3 above), the mesostructured ZnO exhibit an excellent sensing performance—better than other mesostructured materials, such as mesostructured carbon or mesostructured cobalt oxide. The morphology of the mesostructured ZnO was randomly orientated; however, the morphologies of the mesostructured carbon and mesostructured cobalt oxide were

aggregated, causing blockages of the pore entrances. The molecules, of course, could cross the pores more easily when they were not blocked, and so an excellent sensing performance was observed.

5. The DEP-trapped mesostructured carbon was successfully immobilized along the electrode. The highly magnified SEM image shows that the mesostructured carbon still retains the rod structure, with a diameter of approximately 400 nm and a length of approximately 1 μm . The optimal sensitivities of this sensor were 2.9%, 4.3%, 6.6%, 9.2%, and 36.3% for concentrations of 30, 45, 60, 75, and 90 ppm, respectively. This material also had faster response and recovery times, of about 170 s and 250 s.

6. For DEP-trapped mesostructured ZnO, the SEM image indicates that the mesostructured ZnO particles also arranged along the electrode. The highly magnified images showed that the mesostructured ZnO particles were apparently randomly oriented. The random orientation provides electrical paths between neighboring extrusions. It was found that the optimal sensitivities of the ZnO sensors were 12.1%, 14.6%, 18.4%, 26.0%, and 60% at the CO concentrations of 10 ppm, 20 ppm, 30 ppm, 50 ppm, and 70 ppm, respectively. This shows that the porous ZnO gas sensor had a strong response to low CO concentrations; the response and recovery times of the nano-structured ZnO sensor were found to be 85 s and 90 s, respectively.

7. For the DEP-trapped mesostructured cobalt oxide, the captured cobalt oxides formed a massive agglomeration. The SEM image also revealed that DEP-trapped cobalt oxide could be firmly immobilized on the microelectrode, with a length of

530 nm and a diameter of 110 nm. At the optimal temperature, the sensor responses were 8.9%, 11.6%, 13.2%, 16.1%, and 18.5% for concentrations of 10 ppm, 20 ppm, 30 ppm, 50 ppm, and 70 ppm, respectively. This thin-film device had faster response and recovery times, of about 115 and 211 s, respectively.

8. To summarize the aforementioned results (i.e., 5–7 above), the DEP-trapped mesostructured ZnO still exhibited excellent sensing performance—better than those of other mesostructured materials, such as mesostructured carbon or mesostructured cobalt oxide. All of the samples had uniformly arranged morphologies; however, the mesostructured ZnO had a larger pore radius than other mesostructured materials. Therefore, the gas molecules were able to diffuse into the interior of the samples more expeditiously than in other mesostructured materials.



Reference

1. S. H. Schneider, *Sci. Amer.*, 256 (1987) 78.
2. J. Watson, and D. Tanner, *Radio Electron. Eng.*, 44 (1974) 85.
3. J. Fouletier, P. Farby, and M. Kleitz, *J. Electrochem. Soc.*, 123 (1976) 204.
4. T. Oyabu, *J. Appl. Phys.*, 53 (1985) 2785.
5. S.J. Stetter, and W. Penrose, *Sensors*, 10 (2002) 189.
6. S. Hahn, Ph.D. Thesis, Universität Tübingen (2002).
7. N. Barsan, M. Schweizer-Berberich, W. Göpel, *Fresenius J. Anal. Chem.*, 365 (1999) 287.
8. I. Simon, N. Barsan, A. Tomescu, *Sens. Actuators B*, 73 (2001) 1.
9. M. Tiemann, *Chem. Eur. J.*, 13 (2007) 8376.
10. A. Gurlo, and R. Riedel, *Angew. Chem.*, 119 (2007) 3900.
11. M. E. Franke, T. J. Koplin, and U. Simon, *Small*, 2 (2006) 36.
12. G. Korotcenkov, *Sens. Actuators B*, 107 (2005) 209.
13. N. Barsan, U. Weimar, *J. Phys. Condens. Matter.*, 15 (2003) R813.
14. D. Kohl, *J. Phys. D*, 34 (2001) R125.
15. N. Yamazoe, *Sens. Actuators. B*, 108 (2005) 2.
16. C. T. Kresge, M. E. Leonowicz, W. J. Roth, J. C. Vartuli, and J. S. Beck, *Nature*, 359 (1992) 710.
17. J. J. Ying, C. P. Mehnert, and M. S. Wong, *Angew. Chem. Int. Ed.*, 38 (1999) 56.
18. J. S. Beck, J. C. Vartuli, W. J. Roth, M. E. Leonowicz, C. T. Kresge, K. D. Schmitt, C. T. W. Chu, D. H. Olsen, E. W. Sheppard, S. B. McCullen, J. B. Hihhins, and J. L. Schlenker, *J. Am. Chem. Soc.*, 114 (1992) 10834.
19. J. S. Beck, , J. C. Vartuli, G. J. Kennedy, C. T. Kresge, W. J. Rose, S. E. Schramm, *Chem. Mater.*, 6 (1994) 1816.
20. C. Y. Chen, S L. Burkett, H. X. Li, M. E. Davis, *Microporous Mater.*, 2 (1993) 27.

21. A. Steel, S. W. Carr, M. W. Anderson, J. Chem. Soc. Chem. Commun., (1994) 1571.
22. A. Monnier, F. Schüth, Q. Huo, D. Kumar, D. Margolese, R. S. Maxwell, G. D. Stucky, M. Krishnamurty, P. Petroff, A. Firouzi, M. Janicke, B. F. Chmelka, Science, 261 (1993) 1299.
23. G. D. Stucky, A. A. Monnier, F. Schüth, Q. Huo, D. Margolese, D. Kumar, M. Krishnamurty, P. Petroff, A. Firouzi, M. Janicke, B. F. Chmelka, Mol. Cryst. Liq. Cryst., 240 (1994) 187.
24. J. C. Vartuli, C. T. Kresge, M. E. Leonowicz, A. S. Chu, S. B. McCullen, I. D. Johnson, E. W. Sheppard, Chem. Mater., 6 (1994) 2070.
25. A. Firouzi, D. Kumar, L. M. Bull, T. Besier, P. Sieger, Q. Huo, S. A. Walker, J. A. Zasadzinski, C. Glinka, J. Nicol, D. Margolese, G. D. Stucky, B. F. Chmelka, Science, 267 (1995) 1138.
26. A. Firouzi, F. Atef, A. G. Oertli, G. D. Stucky, B. F. Chmelka, J. Am. Chem. Soc., 119 (1997) 3596.
27. C. A. Fyfe, G. Fu, J. Am. Chem. Soc., 117 (1995) 9709.
28. J. C. Vartuli, K. D. Schmitt, C. T. Kresge, W. J. Roth, M. E. Leonowicz, S. B. McCullen, S. D. Hellring, J. S. Beck, J. L. Schlenker, D. H. Olsen, E. W. Sheppard, Chem. Mater., 6 (1994) 1176.
29. Q. Huo, D. I. Margolese, G. D. Stucky, Chem. Mater., 8 (1996) 1147.
30. D. Y. Zhao, Z. H. Luan, and L. Kevan, Chem. Commun., (1997)
31. P. Behrens, Angew. Chem. Int. Ed. 35 (1996) 515.
32. X. S. Zhao, G. Q. Lu, G. J. Millar, Ind. Eng. Chem. Res., 35 (1996) 2075.
33. A. Sayari, Chem. Mater., 8 (1996) 1840.
34. P. Behrens, Adv. Mater., 5 (1993) 127.
35. D. Y. Zhao, and D. Goldfarb, Chemical Commun., 8 (1995) 875.

36. P. Yang, D. Zhao, B. F. Chmelka, and G. D. Stucky, *Chem. Mater.*, 10, (1998) 2033.
37. H. P. Lin, S. B. Liu, C. Y. Mou and C. Y. Tang, *Chem. Comm.*, (1999) 583
38. H. P. Lin and C. Y. Mou, *J. Cluster Sci.*, 10 (1999) 271.
39. P. Lin, Y.-R. Cheng, S. B. Liu, C.Y. Mou, *J. Mater. Chem.*, 9, (1999) 1197.
40. J. Fan, C. Yu, F. Gao, J. Lei, B. Yian L. Wang, Q. Luo, B. Tu, Zhou and D. Zhao, *Angew. Chem.*, 115, (2003) 3254.
41. D. G. Choi, and S. M. Yang, *J. Collo. Interf. Sci.*, 261 (2003) 127.
42. M. M. Braun and L. Pilon, *Thin Solid Films*, 496 (2006) 505.
43. S. Tanaka, T. Maruo, N. Nishiyama, K. Ueyama, H. W. Hillhouse, *Stud. Surf. Sci. Catal.* 165 (2007) 595.
44. S. Kim, J. Ida, V. V. GULIANTS, Y. S. Lin, *International j. environ. Technol. Manag.*, 4 (2004) 21.
45. D. T. ON, S. M. J. Zaidi, S. Kaliaguine, *Micropor. Mesopor. Mater.*, 22 (1998) 211.
46. O. Huo, D. I. Margolese, U. Ciesla, P. Feng, T. E. Gier, P. Sieger, R. Leon, P. M. Petroff, F. Schüth, G. D. Stucky, *Nature*, 368 (1994) 317.
47. O. Huo, D. I. Margolese, U. Ciesla, D. G. Demuth, P. Feng, T. E. Gier, P. Sieger, A. Firouzi, B. F. Chmelka, F. Schüth, G. D. Stucky, *Chem. Mater.*, 6 (1994) 1176.
48. J. M. Gomez-Vega, M. Iyoshi, K. Y. Kim, A. Hozumi, H. Sugimura, and O. Takai, *Thin Solid Films*, 398-399 (2001) 615.
49. D. Zhao, P. Yang, D. I. Margolese, B. F. Chmelka, and G. D. Stucky, *Chem. Commun.*, (1998) 2499.
50. J. M. Kim, S. K. Kim, and R. Ryoo, *Chem. Commun.*, (1998) 259.
51. S. Che, Y. Sakamoto, O. Terasaki, and T. Tatsumi, *Chem. Lett.*, 31 (2002) 214.
52. H. Zhou, S. Zhu, M. Hibino, I. Honma, *J. Power Sources* 122 (2003) 219.

53. S. Á lvarez, M. C. Blanco-López, A. J. Miranda-Ordieres, A. B. Fuertes, T. A. Centeno, *Carbon*, 43 (2005) 866.
54. H. Li, S. Zhu, H. Xi, R. Wang, *Micropor. Mesopor. Mater.*, 89 (2006) 196.
55. A. B. Fuertes, C. Lota, T. A. Centeno, E. Frackowiak, *Electrochim. Acta*, 50 (2005) 2799.
56. H. Zhou, S. Zhu, M. Hibino, I. Honma, M. Ichihara, *Adv. Mater.*, 15 (2003) 2107.
57. W. Göpel, and K. Schierbaum, *in Sensors, Volume 2: Chemical and Biochemical Sensors, Weinheim* (1991) 2.
58. P. Moseley, and B. Tofield, *Solid state gas sensors*, New York and London, Plenum Press (1989).
59. J. Stetter, W. Penrose, *Sensors Update*, 10 (2002) 189.
60. J. A. Cobus, PhD thesis, University of Barcelona, 2001.
61. K. D. Schierbaun, U. K. Kirner, J. F. Geiger, and W. Gopel, *Sens. Actuators B*, 4 (1991) 87.
62. D. Mutschall, PhD thesis, University of Berlin, 1997.
63. J. Marc Madou, and S. Roy Morrison, *CHEMICAL SENSING with SOLID STATE DEVICES*. ACADEMIC PRESS, INC, 1992.
64. H. Ihokura, Ph.D thesis, Kyushu University, (1983) 52.
65. H. Mitsudo, *Ceramics*, 15 (1980) 339.
66. M. Yudasaka, M. Zhang and S. Iijima, *Chem. Phys. Lett.*, 323 (2000) 549.
67. M. C. Carotta, C. Dallara, G. Martinelli, L. Passari, and A. Camanzi, *Sens. Actuators B*, 3 (1991) 101.
68. H. K. Henisch, *Rectifying Semiconductor Contacts*, (1957).
69. G. Ertl, *Reaction mechanism in catalysis by metal*, Chemistry and Physics of Solid Surface, 3, CRC Press, Boca Raton, FL, 1982.
70. D. Zhao, J. Feng, Q. Huo, N. Melosh, G. H. Fredrickson, B. F. Chmelka, and G. D.

- Stucky, Science, 279 (1998) 548.
71. D. Zhao, Q. Huo, J. Feng, B. F. Chmelka, and C. D. Stucky, J. Am. Chem. Soc. 120 (1998) 6024.
72. R. Ryoo, S. H. Joo, and S. Jun, J. Phys. Chem. B, 103 (1999) 7743.
73. J. Suehiro, G. Zhou, and M. Hara, J. Phys. D 36 (2003) L109.
74. C. D. Wagner, L. E. Davis, M. V. Zeller, J. A. Tayler, R. H. Raymond, and L. H. Gale, Surf. Interface Anal. 3 (1981) 211.
75. E. Comini, A. Cristalli, G. Faglia, and G. Sberveglieri, Sens. Actuators B, 65 (2000) 260.
76. D. Y. Zhao, J. L. Feng, Q. S. Huo, N. Melosh, G. H. Fredrickson, B. F. Chmelka, and G. D. Stucky, Science, 279 (1998) 548.
77. D. Y. Zhao, Q. S. Huo, J. L. Feng, B. F. Chmelka, and G. D. Stucky, J. Am. Chem. Soc., 120 (1998) 6024.
78. A. Galarneau, H. Cambon, F. Di Renzo, R. Ryoo, M. Choi, and F. Fajula, New J. Chem. 27 (2003) 73.
79. S. J. Gregg, and K. S. W. Sing, in *adsorption, Surface Area and Porosity*, Academic Press, London, 1982, 244.
80. C. Booth, and D. Attwood, Macromol. Rapid Commun., 21 (2000) 511.
81. J. N. Israelachvili, and H. Wennerström, J. Phys. Chem., 96 (1992) 520.
82. G. Wanka, H. Hoffmann, and W. Ulbricht, Macromolecules, 27 (1994) 414.
83. M. Choi, W. Heo, F. Kleitz, R. Ryoo, Chem. Commun., (2003) 1340.
84. M. Kruk, E. B. Celer, M. Jaroniec, Chem. Mater., 16 (2004) 698.
85. C. J. Brinker, G. Scherer., *Sol-Gel Science*, Academic Press, London, (1990).
86. M. D. Curran, A. E. Stiegman, J. Non-Cryst. Solids, 249 (1999) 62.
87. Y. Li, Z. Feng, Y. Lian, K. Sun, L. Zhang, G. Jia, Q. Yang, and C. Li, Microporous Mesoporous Mater., 84 (2005) 41.

88. R. Iler, *The Chemistry of Silica*, Wiley, New York, 1979.
89. J. Lang, C. Tondre, R. Zana, R. Bauer, H. Hofmann, and W. Ulbricht, *J. Phys. Chem.*, 79 (1975) 276.
90. P. Van Der Voort, M. Benjelloun, and E. F. Vansant, *J. Phys. Chem. B*, 106 (2002) 9027.
91. C. T. Kresge, M. E. Leonowicz, W. J. Roth, J. C. Vartuli, and J. S. Beck, *Nature*, 359 (1992) 710.
92. F. Kleitz, W. Schmidt, and F. Schüth, *Microporous Mesoporous Mater.*, 65 (2003) 1.
93. L. He, Z. Li, and Z. Zhang, *Nanotechnology*, 19 (2008) 1.
94. K. Petrov, N. Zotov, O. Garcia-Martinez, and R. J. Rojas, *J. Solid State Chem.*, 101 (1992) 145.
95. M. Imperor-Clerc, P. Davidson, and A. Davidson, *J. Am. Chem. Soc.*, 122 (2000) 898.
96. M. Burriel, G. Garcia, J. Santiso, A. Abrutis, Z. Saltyte, and A. Figueras, *Chem. Vap. Deposition*, 11 (2005) 106.
97. L. Armelao, D. Barreca, S. Gross, and E. Tondello, *Surf. Sci. Spectra* 8 (2001) 14.
98. C. V. Chenck, J. G. Dillard, and J. W. Murray, *J. Colloid Interface Sci.*, 95 (1983) 398.
99. M. Oku, and Y. Sato, *Appl. Surf. Sci.*, 55 (1992) 37.
100. T. J. Chuang, C. R. Brundle, and D. W. Rice, *Surf. Sci.*, 59 (1976) 413.
101. R. Ryoo, S. H. Joo, M. Kruk, and M. Jaroniec, *Adv. Mater.*, 13 (2001) 677.
102. C. Dickinson, W. Zhou, R. P. Hodgkins, Y. Shi, D. Zhao, and H. He, *Chem. Mater.*, 18 (2006) 3088.
103. J. Sauer, F. Marlow, and F. Schüth, *Phys. Chem. Chem. Phys.*, 3 (2001) 5579.
104. B. Tian, X. Liu, H. Yang, S. Xie, C. Yu, B. Tu, D. Zhao, *Adv. Mater.*, 15 (2003)

- 1370.
105. S. G. Wang, Q. Zhang, D. J. Yang, P. J. Sellin, G. F. Zhong, *Diamond Relat. Mater.*, 13 (2004) 1327.
106. J. Li, Y. Lu, Q. Ye, M. Cinke, J. Han, M. Meyyappan, *Nano Lett.*, 3 (2003) 929.
107. T. Wagner, J. Roggenbuck, C. D. Kohl, M. Fröba, M. Tiemann, *Stud. Surf. Sci. Catal.*, 165 (2007) 347.
108. U. S. Chou, G. Sakai, K. Shimanoe, N. Yamazoe, *Sens. Actuators B*, 98 (2004) 166.
109. G. G. Mandayo, E. Castano, F. J. Gracia, A. Cirera, A. Cornet, J. R. Morante, *Sens. Actuators B*, 95 (2003) 90.
110. G. Sakai, N. Matsunaga, K. Shimanoe, N. Yamazoe, *Sens. Actuators B*, 80 (2001) 147.
111. N. Matsunaga, G. Sakai, K. Shimanoe, N. Yamazoe, *Sens. Actuators B*, 96 (2003) 226.
112. G. Korotcenkov, *Sens. Actuators B*, 107 (2005) 209.
113. A. B. Fuertes, and D. M. Nevskaya, *Microporous Mesoporous Mater.*, 62 (2003) 177.
114. S. Jun, S. H. Joo, R. Ryoo, M. Kruk, M. Jaroniec, Z. Liu, T. Ohsuna, and O. Terasaki, *J. Am. Chem. Soc.*, 122 (2000) 10712.
115. F. Udrea, J. W. Gardner, D. Setiadi, J. A. Covington, T. Dogaru, C. C. Lu, and W. I. Milne, *Sens. Actuators B*, 78 (2001) 180.
116. M. Takata, D. Tsubone, and H. Yanagida, *J. Am. Ceram. Soc.*, 59 (1976) 4.
117. B. L. Zhu, D. W. Zeng, J. Wu, W. L. Song, and C. S. Xie, *J. Mater. Sci.*, 14 (2003) 521.
118. P. Mitra, A. P. Chatterjee, and H. S. Maiti, *Mater. Lett.*, 35 (1998) 33.

119. P. P. Sahay, J. Mater. Sci., 14 (2005) 4383.
120. S. R. Morrison, Sens. Actuators B, 84 (2002) 258.
121. J. F. Chang, H. H. Kuo, I. C. Leu, and M. H. Hon, Sens. Actuators B, 84 (2002) 258.
122. C. Malagù, V. Guidi, M. Stefancich, M. C. Carotta, and G. Martinelli, J. Appl. Phys., 91 (2002) 808.
123. G. Williams, and G. S. V. Coles, MRS Bull., 24 (1999) 25.
124. G. Korotcenkov, V. Macsanov, V. Tolstoy, V. Brinzari, J. Schwank, G. Faglia, Sens. Actuators B, 96 (2003) 602.
125. A. B. Fuertes, Microporous Mesoporous Mater., 67 (2004) 273.
126. W. Wang, K. Lee, T. Kim, I. Park and S. Yang, Smart Mater. Struct., 16 (2007) 1382.
127. H. Yamaura, K. Moriya, N. Miura, and N. Yamazoe, Sens. Actuators B, 65 (2000) 39.
128. S. D. Choi, and B. K. Min, Sens. Actuators B, 77 (2000) 330.
129. J. Wöllenstein, M. Burgmair, G. Plescher, T. Sulima, J. Hildenbrand, H. Böttner, and I. Eisele, Sens. Actuators B, 93 (2003) 442.
130. C. Malagù, V. Guidi, M. Stefancich, M. C. Carotta, and G. Martinelli, J. Appl. Phys., 91 (2002) 808.
131. G. Williams, and G. S. V. Coles, MRS Bull., 24 (1999) 25.
132. N. V. Hieu, L. T. B. Thuy, and N. D. Chien, Sens. Actuators B, 129 (2008) 888.
133. J. W. Veldsink, R. M. J. van Damme, G. F. Versteeg, and W. P. M. van Swaaij, Chem. Eng. J., 57 (1995) 115.
134. J. Li, Y. Lu, Q. Ye, M. Cinke, J. Han, and M. Meyyappan, Nano Lett., 3 (2003) 929.

135. H. Q. Nguyen, and J. S. Huh, Sens. Actuators B 117 (2006) 426.
136. J. C. Obirai, G. Hunter, and P. K. Dutta, Sens. Actuators B 134 (2008) 640.
137. J. H. Lee, J. Kim, H. W. Seo, J. W. Song, E. S. Lee, M. Won, and C. S. Han, Sens. Actuators B, 129 (2008) 628.
138. C. Malagù, V. Guidi, M. Stefancich, M. C. Carotta, G. Martinelli, J. Appl. Phys. 91 (2002) 808.

